

¹ To the Graduate Council:
² I am submitting herewith a thesis written by Jason Bane entitled “The EMC Effect
³ in A=3 Nuclei.” I have examined the final paper copy of this thesis for form and
⁴ content and recommend that it be accepted in partial fulfillment of the requirements
⁵ for the degree of Doctor of Philosophy, with a major in Nuclear Physics.

⁶
⁷

Nadia Fomin, Major Professor

⁸ We have read this thesis
⁹ and recommend its acceptance:

¹⁰ _____

¹¹ Jamie Coble

¹² _____

¹³ Kate Jones

¹⁴ _____

¹⁵ Thomas Papenbrock

¹⁶ _____

¹⁷ Soren Soreson

¹⁸

Accepted for the Council:

¹⁹
²⁰

Carolyn R. Hodges

²¹

Vice Provost and Dean of the Graduate School

²² To the Graduate Council:
²³ I am submitting herewith a thesis written by Jason Bane entitled “The EMC Effect
²⁴ in A=3 Nuclei.” I have examined the final electronic copy of this thesis for form and
²⁵ content and recommend that it be accepted in partial fulfillment of the requirements
²⁶ for the degree of Doctor of Philosophy, with a major in Nuclear Physics.

²⁷ Nadia Fomin, Major Professor

²⁸ We have read this thesis
²⁹ and recommend its acceptance:

³⁰ Jamie Coble

³¹ _____
³²

³³ Kate Jones

³⁴ _____
³⁵

³⁶ Thomas Papenbrock

³⁷ _____
³⁸

³⁹ Soren Soreson

⁴⁰ _____
⁴¹

⁴² Accepted for the Council:

⁴³
⁴⁴ Carolyn R. Hodges

⁴⁵ _____
⁴⁶

⁴⁷ Vice Provost and Dean of the Graduate School

⁴⁸ (Original signatures are on file with official student records.)

49

The EMC Effect in A=3 Nuclei

50

A Thesis Presented for

51

The Doctor of Philosophy

52

Degree

53

The University of Tennessee, Knoxville

54

Jason Bane

55

December 2018

⁵⁶

© by Jason Bane, 2018

⁵⁷

All Rights Reserved.

⁵⁸ Contents

⁵⁹ List of Tables	vi
⁶⁰ List of Figures	vii
⁶¹ 1 Introduction	1
62 1.1 Electron scattering	2
63 1.2 Deep inelastic scattering	8
64 1.2.1 Scaling	11
65 1.2.2 Quark Parton Model	11
⁶⁶ 2 EMC Effect	16
67 2.1 European Muon Collaboration	16
68 2.2 Ratios - cross-sections and Structure Functions	17
69 2.3 EMC Experiments	19
70 2.3.1 Experiments at CERN	19
71 2.3.2 Experiments at SLAC	22
72 2.3.3 HERMES at DESY	23
73 2.3.4 Experiments at Jefferson Lab	24
74 2.4 EMC Theory and Models	26
75 2.4.1 Multiquark Cluster	26
76 2.4.2 Nuclear Binding	26
77 2.4.3 Medium Modification	27

78	2.4.4 Rescaling	27
79	2.5 MARATHON	27
80	3 Experimental Setup	29
81	3.1 Thomas Jefferson Lab	29
82	3.1.1 CEBAF	29
83	3.1.2 Injector	30
84	3.1.3 Accelerator	31
85	3.2 Hall A Beam Line	33
86	3.2.1 Beam Position Monitors	33
87	3.2.2 Raster	36
88	3.2.3 Beam Energy	39
89	3.2.4 Beam Current Monitors	40
90	3.3 Target	42
91	3.4 High Resolution Spectrometers	43
92	3.4.1 Vertical Drift Chambers	45
93	3.4.2 Scintillators	50
94	3.4.3 Cherenkov	51
95	3.4.4 Calorimeter	53
96	3.5 Trigger Setup	54
97	3.6 Kinematic Settings	56
98	4 Data Analysis	59
99	4.1 Analysis Software	59
100	4.1.1 Tracking	60
101	4.2 Electron Counting	62
102	4.3 Efficiencies	62
103	4.3.1 Computer and electronic Lifetime	63
104	4.3.2 Particle Identification Efficiency	63
105	4.3.3 Trigger Efficiency	66

106	4.3.4 Tracking Efficiency	68
107	4.4 Background Subtraction	69
108	4.4.1 End Caps	70
109	4.4.2 Pair Produced Electrons	71
110	4.4.3 Beta Decay of Tritium	72
111	4.5 Luminosity	74
112	4.6 Monte Carlo Ratio Method	74
113	4.6.1 Monte Carlo Simulation	75
114	4.6.2 Monte Carlo Comparison	75
115	4.7 DIS Cross Section	75
116	4.8 Systematic Error	75
117	5 Results	76
118	5.1 EMC Ratios	76
119	5.1.1 Isoscalar Correction	76
120	5.1.2 EMC Effect	76
121	6 EMC Simulation	77
122	6.1 Investigation	77
123	6.2 Transformation	78
124	6.3 Results	80
125	7 Conclusion	83
126	Bibliography	84

¹²⁷ List of Tables

¹²⁸ 3.1	Kinematics originally planned for the MARATHON experiment in-	
¹²⁹	cluding an estimation of time required for three of the gas targets in	
¹³⁰	hours. Estimations provided by John Arrington and Zhihong Ye[46].	57
¹³¹ 3.2	Kinematic settings used during the MARATHON experiment. Kine-	
¹³²	matic 1-15 for LHRS, and kinematic 16 using RHR. The good electron	
¹³³	count is in units of thousands.	57
¹³⁴ 4.1	Livetime during the MARATHON experiment calculated using trigger	
¹³⁵ 2.	63

₁₃₆ **List of Figures**

₁₃₇ 1.1	Simple Feynman diagram of an electron scattering from a proton [31].	4
₁₃₈ 1.2	Ratio of experimentally measured cross section to the Mott cross-section verses $\tan^2\theta/2$ for a Q^2 of 2.5 GeV $^2/c^2$. [2]	6
₁₄₀ 1.3	Electron-proton scattering for incident energy of 4.9 GeV and scattering angle of 10° [16].	9
₁₄₁ 1.4	Measurements of the proton structure function $F_2(x, Q^2)$ for different x settings[29]	10
₁₄₄ 1.5	Data from SLAC plotting the ratio of the structure functions $2x \cdot F_1(x)$ and $F_2(x)$ vs. x [63, 62].	12
₁₄₆ 1.6	Structure function results measured from three lepton-nucleon scattering experiments [14].	13
₁₄₈ 1.7	Elementary particles including leptons, quarks, and bosons with mass, charge, and spin [56].	14
₁₅₀ 2.1	Graph of the ratio of A/D structure functions vs x from the EMC. [41, 10].	17
₁₅₂ 2.2	EMC effect from the BCDMS collaboration [15]. The BCDMS results show in plot 'a' a good comparison from their EMC effect for iron and the results from the EMC. In plot 'b', BCDMS collaboration compare their nitrogen EMC results to SLAC's carbon EMC results.	20
₁₅₆ 2.3	The Q^2 dependence of (F_2^n/F_2^p) for a value of x [6].	21

157	2.4 EMC ratios from SLAC. The plot shows the Q^2 average cross-section ratios with isoscalar corrections for different nuclei [35].	22
158		
159	2.5 The dependence of the atomic mass number on the EMC effect[35]. . .	23
160		
161	2.6 Ratio of nuclear to deuterium cross-section per nucleon corrected for neutron excess[7]. The JLab data in red is compared with SLAC data in Blue [35] and BCDMS data in green [15].	24
162		
163	2.7 Isoscalar EMC effect as function of nuclear density [65].	25
164		
165	3.1 Drawing of the Injector layout.	30
166		
167	3.2 Schematic Layout of CEBAF.	32
168		
169	3.3 A 3D drawing of Hall A.	33
170		
171	3.4 A schematic layout of the beam line in Hall. [5]	34
172		
173	3.5 BPM design diagram, from JLab instrumentation group. Beam direction is from left to right [71].	35
174		
175	3.6 A schematic layout of a harp fork [71]	36
176		
177	3.7 The X and Y position for a Bulls eye scan for BPM calibration. . . .	37
178		
179	3.8 The X and Y current of the raster with a carbon hole. The size of the carbon hole is fit with a radial sigmoid[38].	38
180		
181	3.9 Hall A Current Monitor components [27].	40
182		
183	3.10 BCM calibration [60].	41
184		
185	3.11 BCM frequency for BCM calibration [60].	42
186		
187	3.12 Target Images	43
188		
189	3.13 A side view of a HRS [5].	44
190		
191	3.14 A view of both the left(top) and right(bottom) detector stacks inside the left and right HRS [5].	45
192		
193	3.15 A sketch of the two VDC planes in the HRSs with a particle traveling through the detector at 45°.[30].	46
194		

183	3.16 A possible track that causes signals in wires. The drift electrons will follow the arrow path. The dot/dashed lines correspond to the projected distance used to reconstruct the path of the incident particle. The transition point from parallel to radial field lines is represented by the ellipses. [30]	47
188	3.17 The VDC efficiency for one plane of wires.	48
189	3.18 Histograms of VDC signals before(left) and after(right) calibration of t_0 [45].	49
191	3.19 Histogram of β before and after time walk correction.	50
192	3.20 Top down depiction inside the GC [13].	51
193	3.21 The raw signal captured from a single cherenkov PMT, PMT[1], with a fit to the pedestal peak and a line draw to demonstrate its ADC channel number.	52
196	3.22 Left: The sum of all ADC channels from the LHRS calorimeters. Right: The total energy deposited into the LHRS calorimeter scaled by the momentum setting. Electron cuts have been applied.	54
199	3.23 Scematic drawing of the trigger logic and timing for the MARATHON experiment [40].	55
201	3.24 A kinematic coverage plot, demonstrating the Q^2 coverage for x and Theta. Also the relationship between x and Theta. The band around the points represents the approximate spectrometer acceptance in the y axis.	58
205	4.1 The TCS for an electron scattering event as seen from above. The event happens at z_{react} distance from the Hall center. L is the distance from the Hall center to the sieve plane. D is the horizontal displacement of the spectrometer axis from the ideal position. Θ is the spectrometer's central angle [51].	61

210	4.2	Two dimensional plot of the cherenkov sum versus Total Energy de-				
211		posited, including electron sampling in teal and non-electron sampling				
212		in red.				64
213	4.3	Electrons and other back ground particles identified via cuts in the				
214		total calorimeter and the gas cherenkov shown in the individual layers				
215		of the calorimeters and the cherenkov. Sampling cuts for Electrons in				
216		teal and Non-Electrons in red.				65
217	4.4	The PID efficiency for the cherenkov and both layers of the calorime-				
218		ter,including the overall total PID efficiency for each of the gas targets				
219		at all of the kinematics.				67
220	4.5	Trigger efficiency of trigger 2 for different targets at all kinematics				
221		calculated via sampling from trigger 1.				67
222	4.6	Tracking efficiency of the VDCs for different targets at all kinematics.				68
223	4.7	Comparison of the scattering vertex along the z axis for the empty				
224		target(EM) and the gas targets at kin. 4.				71
225	4.8	The ratio of positron events to electrons for tritium [68].				72
226	4.9	The amount of Helium in the Tritium cell in reference to the total				
227		amount of material in the cell as a function of time. Included are				
228		bands of time for different sections of the Tritium run group's plan [49].				73
229	6.1	Example of the electron beam(red) with a energy of 2.5 GeV and the				
230		proton(blue) with angle of 45° in respect to the electron and with a				
231		momentum of 0.5 GeV/c.				78
232	6.2	Vector representations of the momentum for the incoming electron(red)				
233		and target proton(blue) with units of GeV for each phase of their				
234		transformations before scattering.				79
235	6.3	Vector representations of the momentum for the incoming electron(red)				
236		and target proton(blue) with units of GeV for each phase of their				
237		transformations after scattering).				81

238	6.4 Simulation results for fixed momentum protons. Three runs with	
239	unique proton momentum.	82

²⁴⁰ **Chapter 1**

²⁴¹ **Introduction**

²⁴² Understanding the world around us is the goal of every scientist, from the chemist
²⁴³ that experiments with the formation of atoms to the geologist exploring the process of
²⁴⁴ rock formations. Nuclear physicists focus on studying the fundamental constituents
²⁴⁵ of matter, the building blocks of nature. Physicist use scattering experiments at
²⁴⁶ accelerator facilities, like CERN in Switzerland, DESY in Germany, BATES in
²⁴⁷ Massachusetts, JLab in Virginia, and many others, to study the protons and neutrons
²⁴⁸ that make up a nucleus and the constituents that form the internal structure of a
²⁴⁹ nucleon. These experiments allow physicists to probe inside a nucleus to observe the
²⁵⁰ internal structure and to investigate the interactions between the quarks and gluons.
²⁵¹ Many of the experiments are design to confirm an existing results while also expanding
²⁵² on unique ideas.

²⁵³ In the last century, there have been numerous breakthroughs in the fields of nuclear
²⁵⁴ and particle physics. Rutherford discovered the proton by bombarding light nuclei
²⁵⁵ with alpha particles to produce the reaction,



256 This reaction allowed Rutherford to conclude that the Hydrogen nucleus was a
257 elementary constituent of atomic nuclei [63]. In the late 1950s, experimental results
258 published by W. McAllister and R. Hofstadter exposed some of the eternal structure
259 of the proton [31, 54]. The European Muon Collaboration(EMC) produced results in
260 the early 1980s showing a difference between the internal structure of the deuterium
261 nucleus and Iron [65, 41]. In the current era, scientific labs can produce beams of
262 leptons, hadrons, and heavy ions. These beams can be produced with a large energy
263 spread from "cold" neutrons of $10^{-2}eV$ to protons of $10^{12}eV$. The data received from
264 scattering experiments using beams with a complex structure like alpha particles
265 of heavy ions contain information about the target, the beam, and the interaction
266 between the two.

267 This thesis will discuss using deep inelastic scattering to study the internal structure
268 of two light nuclei and gain a better understanding of the effects of the slight difference
269 between these two light nuclei as part of the E12-010-103 experiment. The discussion
270 will include the motivations, approach, and the outcome from one analysis technique.

271 1.1 Electron scattering

272 Deciphering and analyzing data from scattering experiments that use complex
273 beams can be convoluted because the scattering interaction contains information
274 about the internal structure of the target and the beam along with the complex inter-
275 actions and forces between the two [63]. In order to remove some of the complexity in
276 scattering experiments, one may employ highly relativistic electrons. Electrons being
277 point-like particles without any internal structure allow the elimination of some of
278 the analysis difficulties due to the complex nature of the internal structure of more
279 complex scattering tools. Electrons and the target either a nucleus, nucleon, or quark
280 interact via the exchange of a virtual photon. Using quantum electrodynamics (QED),

281 these interactions can accurately be described by the well known electromagnetic
282 interaction.

283 The electromagnetic interaction describes the coupling of fundamental particles
284 via their electric charge. The interaction between two electrically charged particles
285 begins when a virtual photon is emitted. The amplitude for the emission of photon
286 is proportional to $\sqrt{\alpha}$. Where α is the fine structure constant. Higher order terms
287 of this process contribute very little due to the coupling constant $\alpha \approx 1/137$, being
288 much smaller than one.

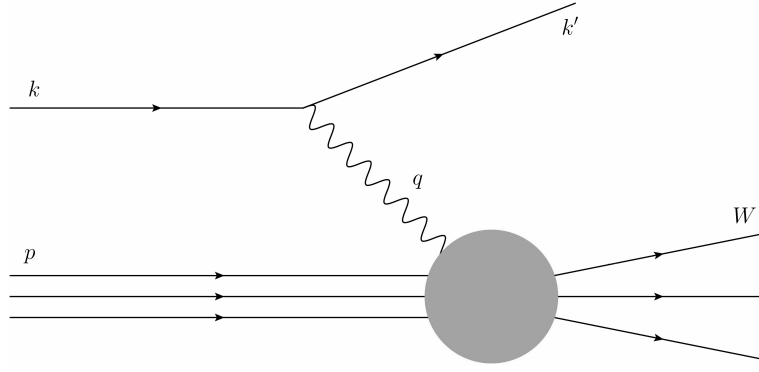
289 The Feynman diagram in figure 1.1 represents an electron scattering from a proton.
290 The incoming or incident electron's four-momentum is described as $k = (E, \vec{k})$ and the
291 scattering electron's four-momentum is represented by $k' = (E', \vec{k}')$. The exchange
292 of the virtual photon in this electromagnetic interaction is defined by the four-
293 momentum transfer q . Q^2 , the square of the momentum transfer is the mass of
294 the virtual photon that interacts with the hadron.

$$Q^2 \equiv -q^2 = 4EE' \sin^2(\theta/2). \quad (1.2)$$

295 In equation 1.2, E is the electrons incident energy and E' is the energy of the scattered
296 electron. Theta is the angle that describes the deflection of E' vector from the
297 electron's incident path. Along with Q^2 , the variables ν , W , and x_B are used to
298 narrate the evolution of the electron scattering process. ν , defined as $P \cdot q/M$. Where
299 P is the 4-vector of the target proton. In the laboratory frame, ν can be described
300 by 1.3. The transformation to laboratory frame allows the use of the resting nature
301 of the target proton. Therefor $P = (Mc, \mathbf{0})$ and $q = ((E - E')/c, \mathbf{q})$.

$$\nu = E - E'. \quad (1.3)$$

Figure 1.1: Simple Feynman diagram of an electron scattering from a proton [31].



Simply, ν is the magnitude of energy loss by the electron during the scattering interaction. The invariant mass of the system, W , defines the hadronic state produced by the scattering event.

$$W^2 \equiv (q + p)^2 = M^2 + 2M\nu - Q^2. \quad (1.4)$$

In the general case of electron scattering off of a free proton or neutron elastically, the scattered energy of the electron will be a function of the incident electron's energy and the scatted angle of the electron, shown in the following equation.

$$E' = \frac{E}{1 + \frac{E}{Mc^2}(1 - \cos\theta)} \quad (1.5)$$

A scattering event with the invariant mass equal to the the mass of the nucleon, M , falls in the regime of elastic scattering and the final state of hadron is a recoiling proton. Increasing the W above M will transform the scattering interaction from an elastic scattering interaction to an inelastic scattering event due to the excited state of the scattered byproduct.

The intrinsic likelihood of an event with a certain Q^2 , ν , and W is defined by the scattering cross section. An electron scattering off of a target with a charge of $Z * e$ can be described by the Rutherford cross-section. Povh et. al. details the Rutherford

³¹⁶ cross section as:

$$\left(\frac{d\sigma}{d\Omega} \right)_{Rutherford} = \frac{(zZe^2)^2}{(4\pi\epsilon_0)^2 * (eE_{kin})^2 \sin^4(\theta/2)}. \quad (1.6)$$

³¹⁷ In the early 1920s, German physicists Stern and Gerlach performed an experiment
³¹⁸ with a beam of silver atoms. The SternGerlach experiment measured the deflection of
³¹⁹ a beam of silver atoms from an inhomogeneous magnetic field[37]. The observations
³²⁰ made by Stern and Gerlach demonstrated that particles bear an intrinsic angular
³²¹ momentum. In 1925, a forbidden spectral line of ionized helium raised questions
³²² of the current understanding of the quantum numbers used. This forbidden line
³²³ lead to the discovery of electron spin by Uhlenbeck and Gloudsmit[36]. The Mott
³²⁴ cross-section is the evolved version of the Rutherford cross-section. The Rutherford
³²⁵ cross-section neglects the spin of an electron and the target. Evolving the Rutherford
³²⁶ cross-section allows for the modifications needed to include the intrinsic spin of the
³²⁷ target and electron. The Mott cross-section is described in equation 1.7 [43, 63].
³²⁸ Where α is the fine structure constant. This constant is related to the strength of
³²⁹ the interaction between an electron and proton[56].

$$\left(\frac{d\sigma}{d\Omega} \right)_{Mott} = \frac{4Z^2\alpha^2(\hbar c)^2 E'^2}{|\mathbf{q}c|^4} \cos^2(\theta/2). \quad (1.7)$$

³³⁰ The inclusion of the interaction between the current of the electron and the target
³³¹ nucleon's magnetic moment creates the necessity to define the magnetic moment.
³³² Equation 1.8 describes the magnetic moment of a charged, spin -1/2 particle. The
³³³ magnetic momentum is build using M , the mass of the particle and g , a factor of 2
³³⁴ relating to relativistic quantum mechanics [63].

$$\mu = g \cdot \frac{e}{2M} \cdot \frac{\hbar}{2} \quad (1.8)$$

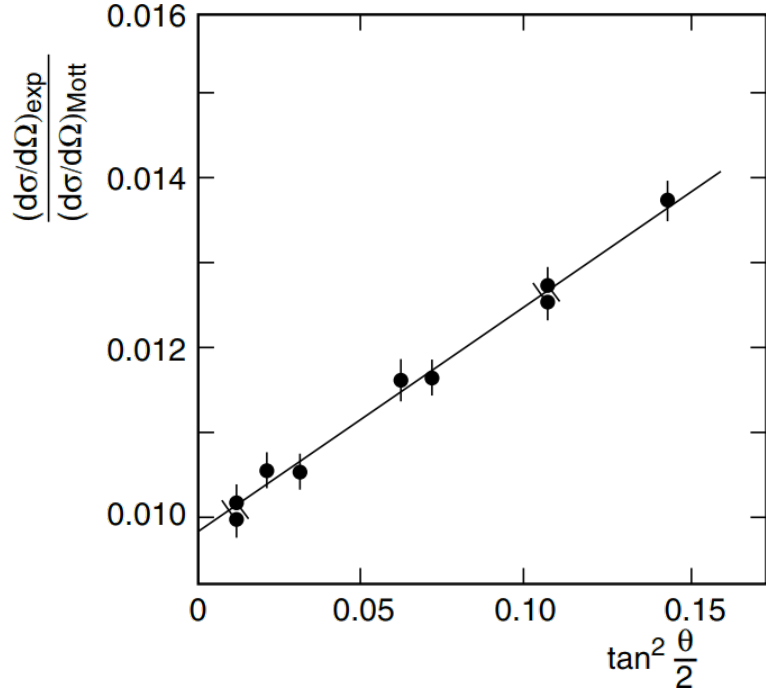


Figure 1.2: Ratio of experimentally measured cross section to the Mott cross-section versus $\tan^2\theta/2$ for a Q^2 of $2.5 \text{ GeV}^2/\text{c}^2$. [2]

335 Modifying the Mott scattering cross section equation to include a spin degree of
 336 freedom, is shown in equation 1.9. τ is used in the cross section formalism to account
 337 for the magnetic moment of a nucleon and is defined as: $\tau = \frac{Q^2}{4M^2c^2}$ [63].

$$\left(\frac{d\sigma}{d\Omega} \right)_{\substack{\text{point} \\ \text{spin } 1/2}} = \left(\frac{d\sigma}{d\Omega} \right)_{\text{Mott}} \cdot \left[1 + 2\tau \tan^2 \frac{\theta}{2} \right] \quad (1.9)$$

338 The interaction described in the Mott cross section equation is mediated by a
 339 single photon and is electromagnetic in nature. For an electromagnetic interaction
 340 conducted at a low resolution, there is an agreement between the measured cross
 341 section and the theoretical Mott cross-section. This agreement is maximized when
 342 in the limit of $|\mathbf{q}| \rightarrow 0$ for scattering events of electrons off of a target nuclei. As
 343 $|\mathbf{q}|$ climbs furtherer from zero and the resolution of probe grows, the experimentally
 344 measured cross sections will begin to differ from the Mott cross section, systematically

345 decreasing [63]. The comparison of the Mott calculated cross section to experimentally
 346 measured cross section for a Q^2 of $2.5 \text{ GeV}^2/\text{c}^2$ is shown in figure 1.2. Increasing the
 347 $|\mathbf{q}|$ of an interaction reduces the size of the wavelength of the virtual photon that
 348 mediates the electromagnetic interaction between the electron and target nuclei and
 349 therefore increases the resolution of the probe. The wavelength of this virtual photon
 350 is inversely proportional to $|\mathbf{q}|$, and can be described by the following: $\lambda = \frac{\hbar}{|\mathbf{q}|}$ [63].
 351 Increasing the amount of momentum transferred in an electromagnetic reaction allows
 352 one to study deeper into the nucleus. The act of probing deeper into the nucleous or
 353 nucleon allows for the substructure of the target.

354 Studying the internal structure of a nucleus with the electromagnetic interaction
 355 requires increasing the momentum transferred. Pushing $|\mathbf{q}|$ to be comparable with the
 356 mass of a nucleon adds more complexity to the details of the scattering interaction.
 357 At the appropriate levels of $|\mathbf{q}|$ to study the nucleons in the nucleus, the Mott cross-
 358 section equation requires modifications to include additional factors that incorporate
 359 information about the target. The Rosenbluth formula is based on the Mott
 360 cross section and embraces target recoil, magnetic moment, and charge and current
 361 distributions. Povh writes the Rosenbluth formula as:

$$\left(\frac{d\sigma}{d\Omega} \right) = \left(\frac{d\sigma}{d\Omega} \right)_{Mott} * \left[\frac{G_E^2(Q^2) + \tau G_M^2(Q^2)}{1 + \tau} + 2\tau G_M^2(Q^2) \tan^2 \frac{\theta}{2} \right]. \quad (1.10)$$

Equation 1.10 contains $G_E^2(Q^2)$ and $G_M^2(Q^2)$, the electric and magnetic form
 factors. These form factors depend on Q^2 , and this measured dependence provides
 information on the radial charge distributions and magnetic moments of the scattering
 participants. For the instance of $Q^2 \rightarrow 0$, the values of $G_E^2(0)$ and $G_M^2(0)$ are
 physically important.

$$\begin{aligned} G_E^P(Q^2 = 0) &= 1 & G_E^n(Q^2 = 0) &= 0 \\ G_M^P(Q^2 = 0) &= 2.79 & G_M^n(Q^2 = 0) &= -1.91 \end{aligned} \quad (1.11)$$

362 The $G_E^2(0)$ corresponds to the electric charge of the target. $G_M^2(0)$ is simplified to
363 the magnetic momentum normalized by the nuclear magneton. The result of $G_E^2(0)$
364 and $G_M^2(0)$ for the proton and neutron are shown in equation 1.11[63]. There were
365 many experiments at SLAC that studied the Q^2 dependence of these form factors in
366 the early seventies. The results from these form factor experiments determined that
367 $G_E^p(Q^2) = \frac{G_M^p(Q^2)}{2.79} = \frac{G_M^n(Q^2)}{-1.91} = G^{dipole}(Q^2)$. Where $G^{dipole}(Q^2)$ is a dipole fit that
368 describes the form factors very well[63].

369 1.2 Deep inelastic scattering

370 The first generation of electron scattering experiments achieving a significantly
371 large $|\mathbf{q}|$ used a linear accelerator with a 25 GeV maximum beam energy, and following
372 generations increased the total interaction energy to substantially higher thresholds.
373 At these high incident beam energies, individual resonances cannot be separated in
374 the invariant mass spectrum above 2.5 GeV. Observations made into this convoluted
375 invariant mass spectrum has shown that many strongly interacting particles are
376 produced, known as hadrons. Scattering interactions that generate these hadrons
377 are considered to be inelastic.

378 Figure 1.3 contains the invariant mass spectrum for an electron scattering from a
379 proton target for an incident energy of 4.9 GeV and angle of 10° [16]. These results
380 are from an experiment at Deutsches Elektronen-Synchrotron (DESY) published in
381 1968. The elastic scattering peak is scaled down by a factor of 15 to provide an
382 appropriate scaling of the complete spectrum. As ν increases or the scattered electron
383 energy decreases relative to the incident energy, the invariant mass of the scattering
384 interaction increases. As W rises, the resonance begin to convolute together. This
385 behavior is indicative of reaching a new threshold. For scattering interactions with
386 $W \gtrsim 2.0\text{GeV}/c^2$, observations are made that result in the discovery of the production
387 of many strongly interacting particles.

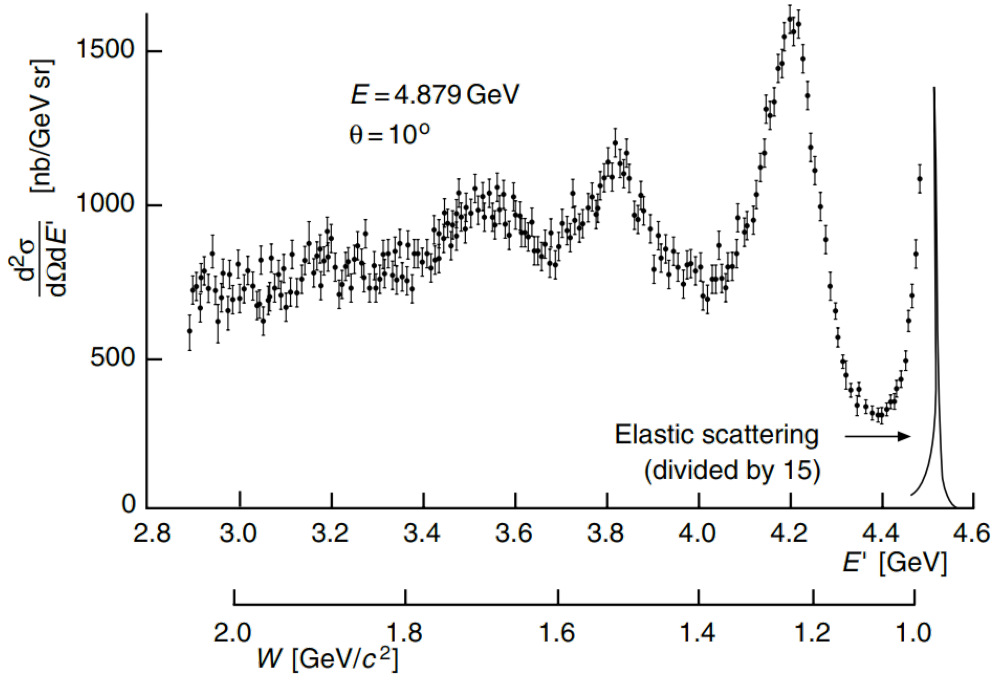


Figure 1.3: Electron-proton scattering for incident energy of 4.9 GeV and scattering angle of 10° [16].

388 Inelastic scattering events contain the possibility of conceiving additional resultants
 389 causing an increase in the complexity of a scattering interaction. In order to create
 390 an inelastic event, the wavelength of the virtual photon has to be comparable to
 391 the radius of the struck nucleon. Increasing the amount of transferred momentum
 392 so that $Q^2 R^2 \gtrsim 1$, will increase the resolution of the probe to a level that allows
 393 for the interaction to be with the charge constituents within the nucleon. When
 394 the scattering event probes the fundamental elements of a nucleon, the scattering
 395 process is titled deep inelastic scattering(DIS). Due to the increase in complexity, an
 396 additional degree of freedom has to be introduced into the scattering cross section
 397 formalism. Modifying the Rosenbluth formula to include the inelastic scattering
 398 structure functions $F_1(Q^2, \nu)$ and $F_2(Q^2, \nu)$ evolves the Rosenbluth formula to contain
 399 the needed complexity of an inelastic event. These modifications are shown in
 400 equation 1.12. The F_1 and F_2 structure functions provide the details for describing the
 401 internal composition of the nucleon [63]. For elastic scattering events $2M\nu - Q^2 = 0$,

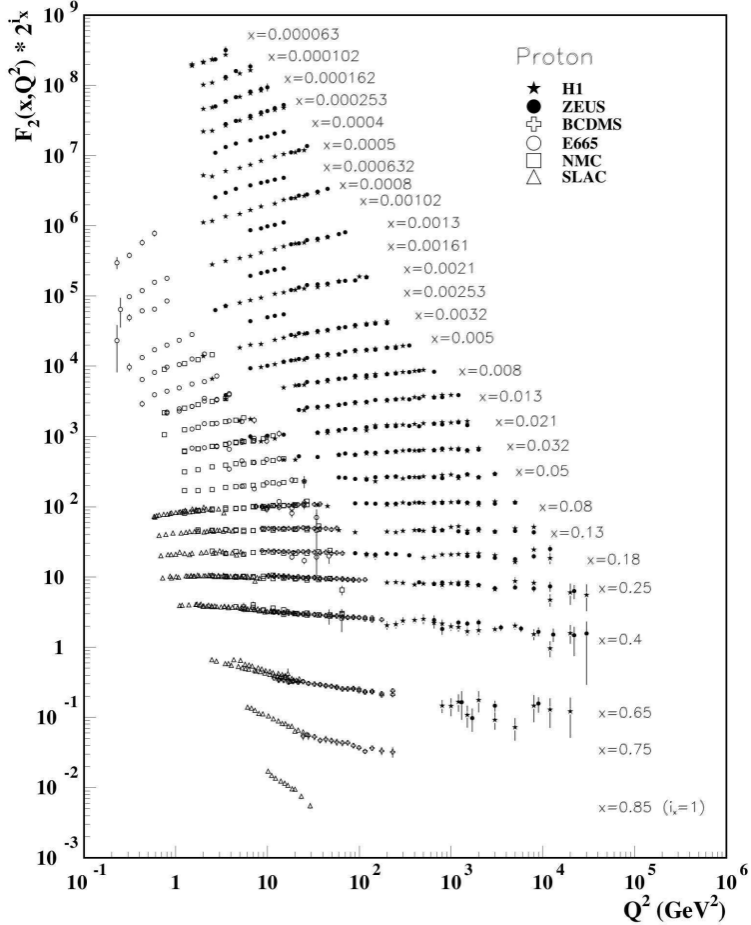


Figure 1.4: Measurements of the proton structure function $F_2(x, Q^2)$ for different x settings[29].

402 this forces only one kinematic parameter to vary freely. However for inelastic
 403 scattering events $2M\nu - Q^2 > 0$, this creates an additional free parameter and is
 404 the reason for the F_1 and F_2 structure functions being functions of both Q^2 and ν .

$$\frac{d^2\sigma}{d\Omega dE'} = \left(\frac{d\sigma}{d\Omega} \right)_{Mott} \left[\frac{F_2(Q^2, \nu)}{\nu} + \frac{2F_1(Q^2, \nu)}{M} \tan^2 \frac{\theta}{2} \right]. \quad (1.12)$$

405

406 **1.2.1 Scaling**

407 The Bjorken scaling variable, x_B or x , is a dimensionless quantity that measures
408 the in-elasticity of a scattering process and is defined as: $x \equiv \frac{Q^2}{2M\nu}$. Measurements
409 from the Standford Linear Accelerator(SLAC) and others for the DIS F_2 structure
410 function are displayed in figure 1.4. This plot displays results of F_2 as a function of
411 x and Q^2 . The x dependence of F_2 is strong and shows that F_2 will decrease as x
412 increases. However, at a constant value of x , the dependence of Q^2 on F_2 is weak
413 for moderate values of x . This phenomenon of a solo dependence on x was known
414 as scaling. This scaling was observed to be present for scattering interactions with
415 $Q^2 > 2\text{ GeV}^2$ and $\nu > 2.5\text{GeV}$ [14]. In the Bjorken limit, $v \rightarrow \infty$ and $Q^2 \rightarrow \infty$, the
416 deep inelastic structure functions can be described as functions of only x .

417 **1.2.2 Quark Parton Model**

418 In the case of DIS off of a proton, the electron probe is used to explore the exclusive
419 internal structure of the proton, it's constituents. In 1969, Feynman assumed the
420 internal make up of the proton was that of point-like partons [20, 48], the basis
421 of the parton model. As part of this model, the impulse approximation makes an
422 assumption that the duration of the interaction between the mediating photon and
423 parton is relatively short, allowing for the interaction between individual partons to
424 be neglected. Thus in a DIS interaction, the partons can be described as quasi-free,
425 with minimal internal interactions. Under this understanding, an electron-nucleon
426 DIS interaction would characterize the properties and motions of the partons that
427 form the struck nucleon[48].

428 The characteristics, (the motions and properties), of the partons are formalized into
429 a parton distribution function $f_i(x_B)$ [63]. The relationship for the parton distribution
430 function with the F_2 structure function is shown in equation 1.13. The F_1 structure
431 function is the DIS equivalent to the magnetic form factor from equation 1.11, and

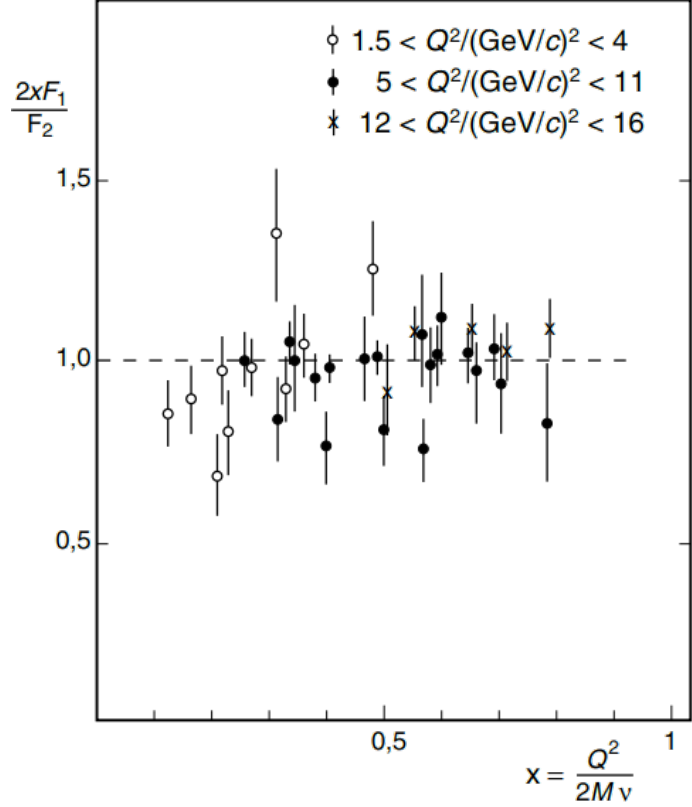


Figure 1.5: Data from SLAC plotting the ratio of the structure functions $2x \cdot F_1(x)$ and $F_2(x)$ vs. x [63, 62].

will vanish for scattering from spin zero particles [63]. Figure 1.5 shows the linear relationship of the ratio of $\frac{2xF_1}{F_2}$ as a function of x . This data from SLAC helped confirmed theories from C. G. Callan Jr. and David J. Gross that the partons that are found in the nucleons of a nucleus are spin 1/2 [22, 32]. The relationship between F_1 and F_2 is known as the Callan-Gross relation [63]. This relationship can be seen in equation 1.14.

$$F_2(x) = x \sum_i e_i^2 f_i(x) \quad (1.13)$$

$$F_1(x) = \frac{1}{2x} F_2(x) \quad (1.14)$$

438

$$F_2(x) = x \cdot \sum_f z_f^2 (q_f(x) + \bar{q}_f(x)) \quad (1.15)$$

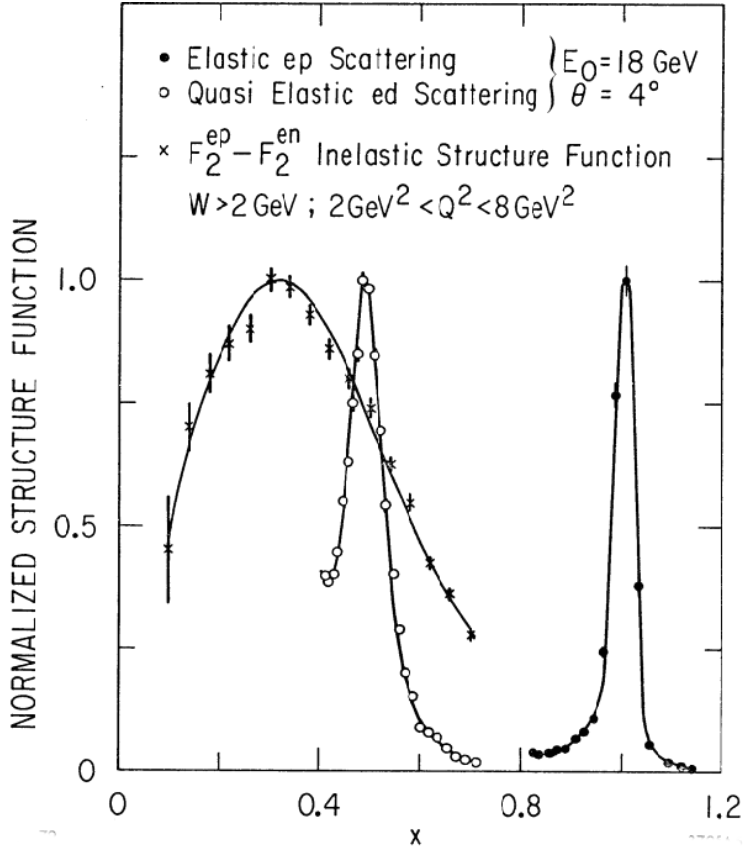


Figure 1.6: Structure function results measured from three lepton-nucleon scattering experiments [14].

439 The electromagnetic interaction that occurs during a scattering event happens
 440 between two charged bodies. The electron carries a charge of $-e$ and the proton
 441 carries a charge of $+e$. The partons that makeup the proton or neutron must carry a
 442 total charge equal to the charge of the proton or neutron. Using DIS scattering from
 443 electron, neutrino, and muon beams, the amount of charge carried by the partons
 444 was determined by using the equation 1.15 [63, 32, 22].

445 Figure 1.6 from Atwood et. al. (1982), contains data on three unique experiments
 446 plotting structure function results against x . Solid dots are elastic electron proton at
 447 an incident energy of 18 GeV and scattered angle of 4° . The elastic peak at x of 1
 448 is due to the scattering event happening elastically off the entire proton. The open

Three Generations of Matter (Fermions)			
I	II	III	
mass → 2.4 MeV charge → $\frac{2}{3}$ spin → $\frac{1}{2}$ name → u up	mass → 1.27 GeV charge → $\frac{2}{3}$ spin → $\frac{1}{2}$ name → c charm	mass → 171.2 GeV charge → $\frac{2}{3}$ spin → $\frac{1}{2}$ name → t top	mass → 0 charge → 0 spin → 1 name → γ photon
Quarks			Gauge Bosons
mass → 4.8 MeV charge → $-\frac{1}{3}$ spin → $\frac{1}{2}$ name → d down	mass → 104 MeV charge → $-\frac{1}{3}$ spin → $\frac{1}{2}$ name → s strange	mass → 4.2 GeV charge → $-\frac{1}{3}$ spin → $\frac{1}{2}$ name → b bottom	mass → 0 charge → 0 spin → 1 name → g gluon
Leptons			
mass → <2.2 eV charge → 0 spin → $\frac{1}{2}$ name → e electron neutrino	mass → <0.17 MeV charge → 0 spin → $\frac{1}{2}$ name → νμ muon neutrino	mass → <15.5 MeV charge → 0 spin → $\frac{1}{2}$ name → ντ tau neutrino	mass → 91.2 GeV charge → 0 spin → 1 name → Z⁰ weak force
mass → 0.511 MeV charge → -1 spin → $\frac{1}{2}$ name → e electron	mass → 105.7 MeV charge → -1 spin → $\frac{1}{2}$ name → μ muon	mass → 1.777 GeV charge → -1 spin → $\frac{1}{2}$ name → τ Tau	mass → 80.4 GeV charge → ±1 spin → 1 name → W± weak force

Figure 1.7: Elementary particles including leptons, quarks, and bosons with mass, charge, and spin [56].

points are quasi-elastic scattering from deuterium. The peak is located at 0.5 in x because the scattering event happens from the proton and neutron, which individually contain only half of the mass of the complete deuteron. The data represented by an 'x' displays result from an inelastic electron scattering measurement. The data plotted is the difference between two nucleon structure functions. The peak is located at one-third. The location of the peak at one-third demonstrates that the struck constituents of the nucleon have a mass approximately one-third of the nucleon and there exist three constituents inside the nucleon with equal mass[14, 63].

Nuclear physicist of the mid 19th century changed the understanding of the building blocks of nature by discovering fundamental constitutes of the protons and neutrons. It was unearthed that these partons have an electric charge, spin of $1/2$, and some mass. Due to these partons having these properties, they can be identified as quarks from Gell-Mann's symmetry scheme, the eightfold way. This theory was based on the SU(3) mathematical symmetry [37, 34]. Through nuclear and high energy

⁴⁶³ experiments six quarks have been discovered[19]. A table of the elementary particles
⁴⁶⁴ is shown in figure 1.7.

⁴⁶⁵ A scattering interaction between a lepton probe and a target nucleus probes the
⁴⁶⁶ structure of the target. A DIS interaction delves inside the nucleus to observed the
⁴⁶⁷ nucleons and their quarks and gluons. The European Muon Collaboration (EMC)
⁴⁶⁸ used DIS experiment to study the internal structure of a few targets. Their use of
⁴⁶⁹ DIS in 1983 discovered a new phenomenon defined as the EMC effect [63, 41].

470 **Chapter 2**

471 **EMC Effect**

472 **2.1 European Muon Collaboration**

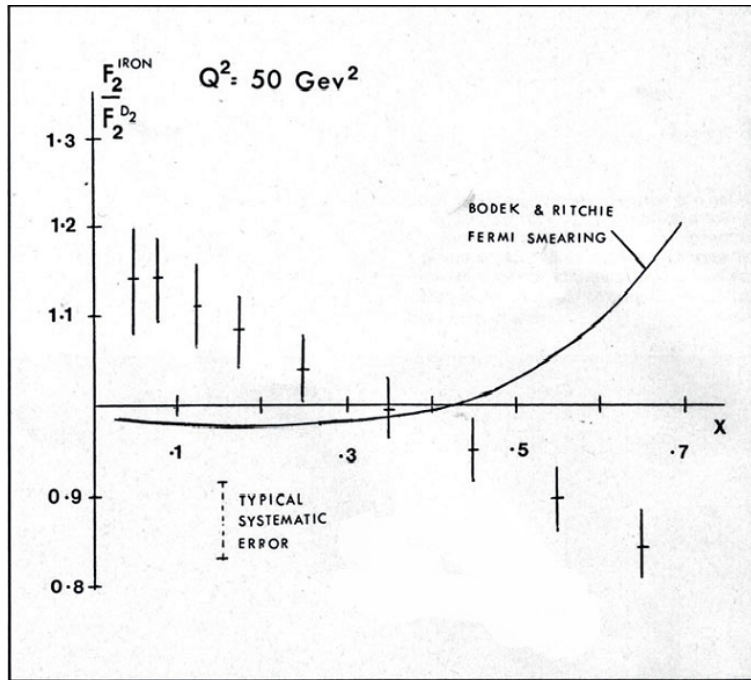
473 The European Muon Collaboration (EMC) performed a deep inelastic measurement
474 with 120-280 GeV muons on iron, hydrogen, and deuteron targets to begin a
475 comprehensive study of muon scattering [53, 59]. The EMC used muons in order
476 to reach their goal of achieving interactions at a large Q^2 [66]. The EMC studied
477 the per nucleon normalized Fe/D structure function ratio versus the Bjorken scaling
478 variable, x . The EMC expectations for this ratio originally was unity for x between
479 0.05 and 0.7 and would deviate at higher x due to Fermi smearing[41]. The reasoning
480 for this expectation was the belief that at large magnitude of Q^2 the interaction
481 between protons and neutrons would not contribute to the total structure function of
482 the nucleus. This was the understanding because the binding energy of a few MeV
483 would not interferer with the GeV scale of the DIS interaction [26]. The expected
484 structure function for a nucleus could be written as:

$$F_2^A = NF_2^N + ZF_2^P. \quad (2.1)$$

485 In this quasi-free nucleon picture, the nucleons are used to build up the nuclear
486 structure (F_2^A) by summing up the neutron structure functions (F_2^N) with the proton

487 structure functions(F_2^P) for each nucleon. Their results for their ratio comparison
 488 of iron and deuterium are shown in Figure 2.1. The $\frac{A}{D}$ structure function ratio
 489 showed an unexpected downward slope. This phenomenon was titled the EMC
 490 effect. This finding demonstrated to the EMC that their understanding of the nucleus
 491 was incorrect. A nucleon's structure function and thereby, the constituent quark
 distributions are altered by the structure of the nuclear medium.

Figure 2.1: Graph of the ratio of A/D structure functions vs x from the EMC.
 [41, 10].



492

493 2.2 Ratios - cross-sections and Structure Func- 494 tions

495 In chapter one, we defined the inelastic cross-section in equation 1.12.

$$\sigma^A = \frac{4\alpha^2 E'^2}{Q^4} \left[2 \frac{F_1^A(x)}{M} \sin^2 \frac{\theta}{2} + \frac{F_2^A(x)}{\nu} \cos^2 \frac{\theta}{2} \right]. \quad (2.2)$$

⁴⁹⁶ In figure 2.1, the EMC collaboration analyzed the ratio of F_2 structure functions.
⁴⁹⁷ The per nucleon cross-section of two different nuclei can be reduced to the ratio of
⁴⁹⁸ the F_2 structure functions.

$$\frac{\sigma_{A_2}}{\sigma_{A_1}} = \frac{F_2^{A_2}}{F_2^{A_1}} \quad (2.3)$$

⁴⁹⁹ The reduction of the ratio of two nuclei begin by using the ratio of longitudinal and
⁵⁰⁰ transverse cross-sections as a function of F_1/F_2 .

$$R = \frac{\sigma_L}{\sigma_T} = \left(1 + \frac{\nu^2}{Q^2}\right) \frac{MF_2}{\nu F_1} - 1 \quad (2.4)$$

⁵⁰¹ The ratio of two unique per nucleon cross-sections is:

$$\frac{\sigma_{A_2}}{\sigma_{A_1}} = \frac{F_2^{A_2}}{F_2^{A_1}} \frac{\left[1 + 2\frac{\nu F_1^{A_2}}{MF_2^{A_2}} \tan^2 \frac{\theta}{2}\right]}{\left[1 + 2\frac{\nu F_1^{A_1}}{MF_2^{A_1}} \tan^2 \frac{\theta}{2}\right]} \quad (2.5)$$

⁵⁰² Where A_1 and A_2 denote the different nuclei. Using the definition of R in equation
⁵⁰³ 2.5, the per nucleon cross-section ratio of A_1 and A_2 can be simplified to equation
⁵⁰⁴ 2.3 [10, 66]. The simplification of the cross-section ratio to the structure function
⁵⁰⁵ ratio is based on the use of R . The longitudinal and transverse cross-section ratio
⁵⁰⁶ has been studied extensively for many nuclei. The measurements of R have shown
⁵⁰⁷ no dependence on the number of nucleons [10].

⁵⁰⁸ The x spectrum of a per nucleon cross-section ratio of some nucleus with A nucleons
⁵⁰⁹ and deuterium also known as an A/D ratio or an EMC ratio is broken into 4 different
⁵¹⁰ regions.

- ⁵¹¹ • For $x < 0.1$, the shadowing region has an EMC ratio that shows a decline of
⁵¹² the nuclear structure functions. A coupling of the photon to strongly interacting
⁵¹³ quarks causes this feature [63].
- ⁵¹⁴ • The anti-shadowing region of the x spectrum lies at $0.1 \leq x < 0.3$. The results
⁵¹⁵ of DIS experiments show an EMC ratio slightly larger than unity in this region.

516 This increase is caused by constructive interference among the multi-scattering
517 amplitudes in the nucleus [21].

- 518 • X between 0.3 and 0.7 is the EMC effect region. This region will be discussed
519 furtherer in this chapter.
- 520 • For $X > 0.7$, the EMC ratio grows rapidly above unity. This region is the Fermi-
521 motion region. The motion of the nucleons inside a nucleus creates a distribution
522 of the nucleons' momentum. The convolution between the nucleons' structure
523 function and momentum distribution form the nuclear structure function. This
524 causes the nuclear structure function of an $A > 2$ nucleus to rise quickly
525 compared to a deuterium nucleus [26, 63].

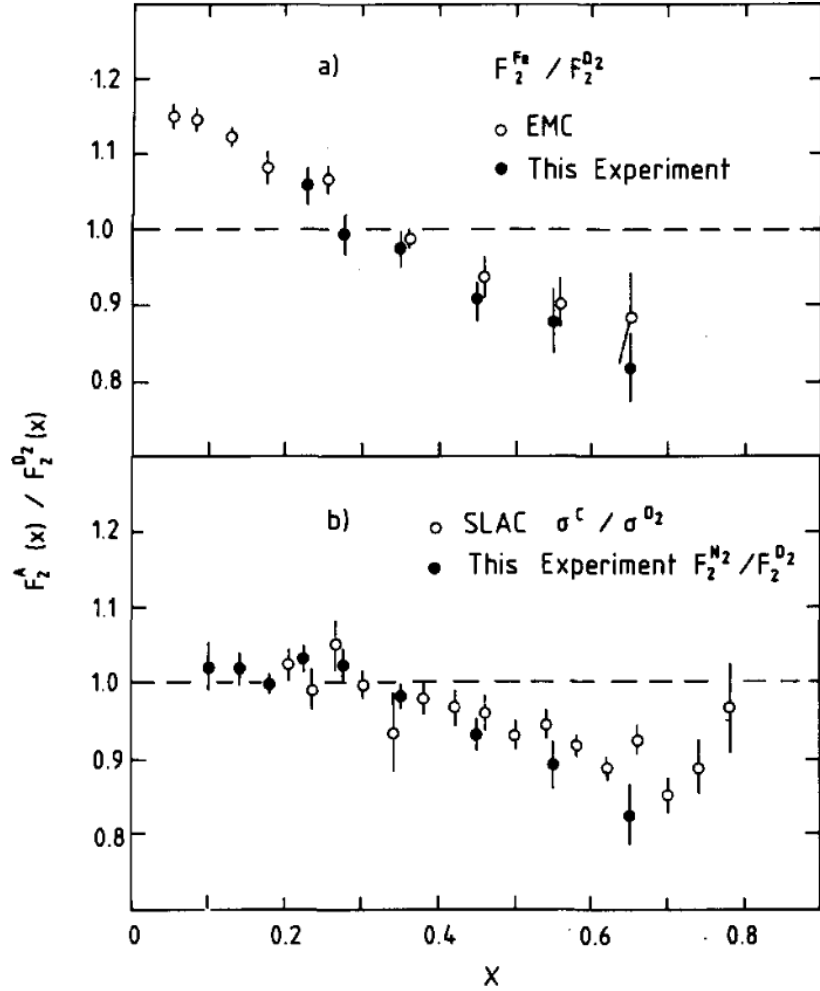
526 2.3 EMC Experiments

527 2.3.1 Experiments at CERN

528 **EMC** The EMC published results from muon beam experiments in 1981-1983 [9,
529 10, 11, 12]. The EMC used data from this group of experiments to form the first
530 EMC ratios, shown in 2.1. The experiments used muon beams of 120 to 280 GeV to
531 extract nuclear and nucleon structure functions from iron, deuterium and Hydrogen
532 targets. The use of multiple indecent beam energies allowed these experiments to
533 have a Q^2 for x of 0.05 between 8 and 20 GeV^2 and a Q^2 for x of 0.65 between 35 and
534 200 GeV^2 [12]. Throughout this run of experiments, the EMC used the EMC forward
535 detector but the experiments were conducted at different times causing a rise in the
536 total uncertainties for the EMC ratios[10]. After publishing the results for the EMC
537 effect, the EMC conducted another round of experiments for two reasons. First the
538 EMC focused on decreasing the systematic uncertainties that were seen in the first
539 EMC effect analysis. They also want to expand the knowledge of the EMC effect of

540 more nuclei [8, 26]. This included measuring muon scattering on carbon, copper, and
 541 tin [8].

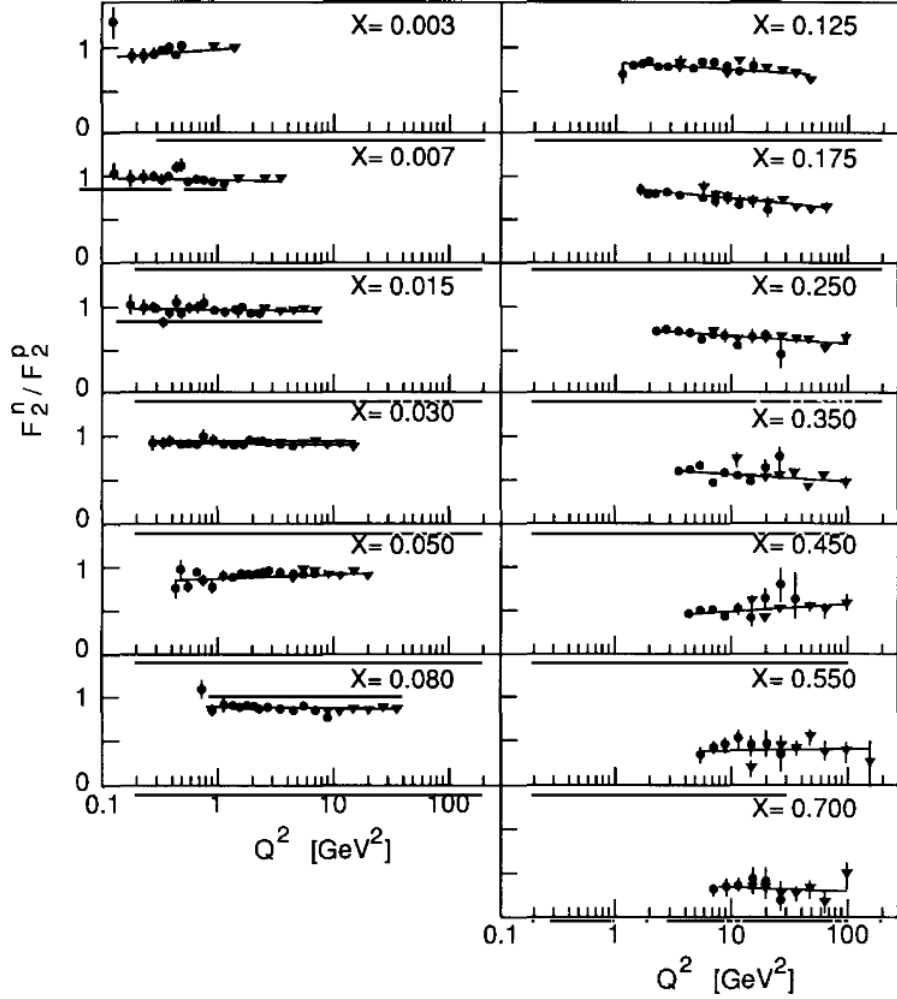
Figure 2.2: EMC effect from the BCDMS collaboration [15]. The BCDMS results show in plot 'a' a good comparison from their EMC effect for iron and the results from the EMC. In plot 'b', BCDMS collaboration compare their nitrogen EMC results to SLAC's carbon EMC results.



542 **BCDMS** The Bologna-CERN-Dubna-Munich-Saclay(BCDMS) collaboration at CERN
 543 continued the study of the EMC effect by comparing their measurement of the cross-
 544 section of nitrogen and iron to deuterium. This experiment used a 40m long iron
 545 toroid magnet with 8 modules consisting of scintillators and multiwire proportional
 546 chambers [15]. The data collected from this spectrometer is shown in figure 2.2. The

⁵⁴⁷ BCDMS collaboration compares their data to the EMC collaboration, demonstrating
⁵⁴⁸ the consistency of their measurement for the EMC effect for iron [15, 59].

Figure 2.3: The Q^2 dependence of (F_2^n/F_2^p) for a value of x [6].



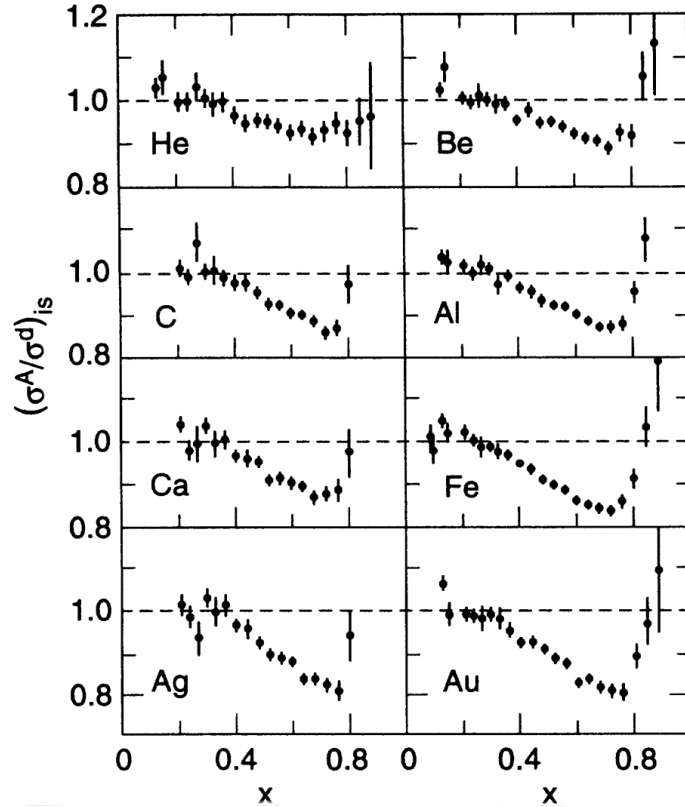
⁵⁴⁹ **NMC** In the winter of 1985, the New Muon Collaboration(NMC) purposed to used
⁵⁵⁰ the muon beam at CERN to expand the understanding of the A dependence for the
⁵⁵¹ EMC ratios at low- x and to understand the Q^2 dependence of the EMC ratios. Along
⁵⁵² with the EMC ratios, the NMC also wanted to improve the current measurements
⁵⁵³ for the neutron structure function, F_2^n , and the neutron to proton structure function
⁵⁵⁴ ratio, (F_2^n/F_2^p) [58]. This experiment consisted of completing muon scattering on
⁵⁵⁵ solid targets of Be, C, Al, Ca, Fe, Sn, and Pb. The data for this experiment covered

556 a kinematic range in x of 0.01 to 0.8, and in Q^2 from 2 to 70 GeV^2 [6]. The NMC
 557 concluded the Q^2 for the EMC ratios is small and the dependence of A for the EMC
 558 effect is approximately logarithmic [6, 26].

559 2.3.2 Experiments at SLAC

560 Scientists at the Stanford Linear Accelerator Center(SLAC) extracted EMC ratios
 561 for many nuclei including; ${}^4\text{He}$, ${}^9\text{Be}$, ${}^{12}\text{C}$, ${}^{27}\text{Al}$, ${}^{40}\text{Ca}$, ${}^{56}\text{Fe}$, ${}^{108}\text{Ag}$, and ${}^{197}\text{Au}$. This
 562 experiment used an electron beam of 8 to 24.5 GeV. The data spanned a large range
 563 of x , from 0.089 to 0.8, and Q^2 , from 2 to 15 GeV^2 to extract cross-sections ratios.
 564 The EMC ratios were extracted by counting the electrons detected by the SLAC 8-
 565 GeV/c magnetic focusing spectrometer [35]. The EMC ratios for the eight different
 nuclear targets are shown in figure 2.4.

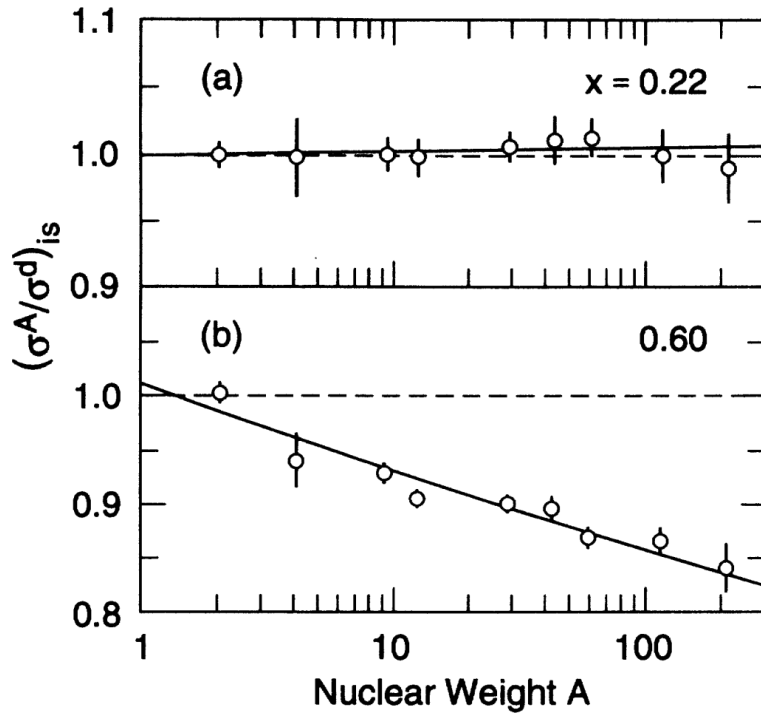
Figure 2.4: EMC ratios from SLAC. The plot shows the Q^2 average cross-section ratios with isoscalar corrections for different nuclei [35].



566

567 The analysis of these ratios revealed the magnitude of the EMC effect, taken to
 568 be the A/D ratio at $x = 0.6$, was found to be different for the various nuclei, and
 569 roughly scaled with the size or density of the nuclei. Figure 2.5, shows the EMC
 570 effect magnitude as a function of the nuclear weight of the targets. It demonstrates
 571 an agreement with data from the NMC, that the EMC effect's dependence on A, to
 be approximately logarithmic [26, 35, 66].

Figure 2.5: The dependence of the atomic mass number on the EMC effect[35].



572

573 2.3.3 HERMES at DESY

574 The High-Energy Radiation Megavolt Electron Source(HERMES) collaboration
 575 used the Hadron-Electron Ring Accelerator(HERA) at Deutsches Elektronen-Synchrotron
 576 (DESY), German Electron Synchrotron, to study the DIS cross-section ratios of ${}^3\text{He}$,
 577 ${}^{14}\text{N}$, and ${}^{84}\text{Kr}$ with respect to D [3]. Data was collected at x kinematics ranging
 578 from 0.010 and 0.65 with Q^2 varying between 0.5 and 15 GeV 2 [3]. The HERMES

579 collaboration used a 27.5 GeV positron beam to scatter off of gaseous targets into the
 580 HERMES forward angle spectrometer.

581 2.3.4 Experiments at Jefferson Lab

582 Experiments at Thomas Jefferson National Accelerator Facility(JLab) produced
 583 two notable EMC ratio results. In 2006, an experiment designed to study the scaling
 584 of the structure functions of the target nucleus produced data for the extraction of
 585 EMC ratios for C, Fe, and Au. The kinematics of this experiment produced data in
 586 the resonance region with a $Q^2 \approx 4 \text{ GeV}^2/c^2$ and $1.2 < W^2 < 3 \text{ GeV}^2/c^2$. This data
 587 is shown in figure 2.6 compared with data from SLAC and BCDMS.

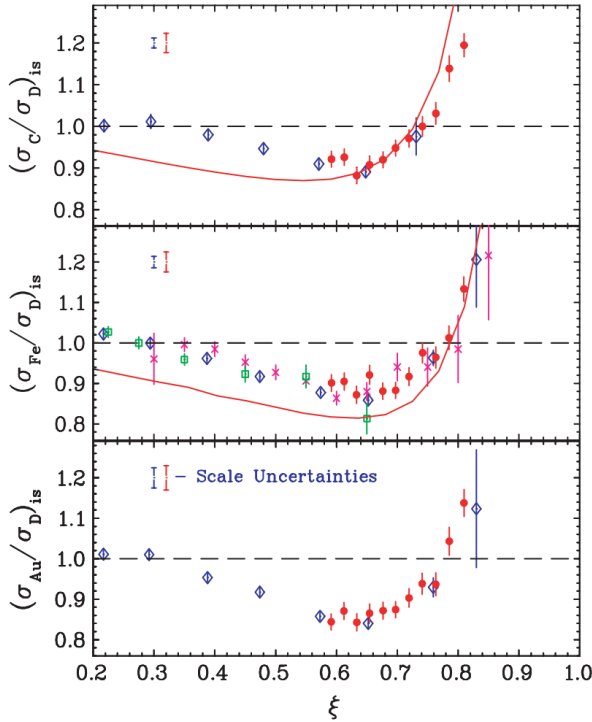


Figure 2.6: Ratio of nuclear to deuterium cross-section per nucleon corrected for neutron excess[7]. The JLab data in red is compared with SLAC data in Blue [35] and BCDMS data in green [15].

$$\xi = \frac{2x}{\sqrt{1 + \frac{4M^2x^2}{Q^2}}} \quad (2.6)$$

588 The SLAC and BCDMS experiments took data in the DIS region with a $W^2 >$
 589 $3 \text{ GeV}^2/c^2$. The Q^2 value of the data needs to be accounted for in a comparison
 590 made between these three experiments. This has been done by using Nachtmann
 591 variable ξ , defined in equation 2.6 [7]. The results show that the EMC ratio in
 592 the resonance region matches the same ratio from the DIS region and therefore DIS
 593 structure functions information can be extracted from the resonance region [66].

594 In 2009, results from another Jefferson lab experiment were published describing
 595 the EMC effect in very light nuclei. This experiment measured the inclusive cross-
 596 section from D, ${}^3\text{He}$, ${}^4\text{He}$, ${}^9\text{Be}$, and ${}^{12}\text{C}$ for x between 0.3 and 0.9, with $Q^2 \approx 3\text{-}6$
 597 GeV^2 [65]. This experiment provided the first results for ${}^3\text{He}$ EMC ratios for high x .
 598 Also, results from all of the nuclear targets showed that the nuclear dependence of
 599 the EMC effect may depend on the local nuclear environment [65]. Previous results
 600 showed a logarithmic dependence of the EMC effect on A. The EMC results for ${}^9\text{Be}$
 601 create a disagreement from past results. This analysis is shown in figure 2.7 [65].

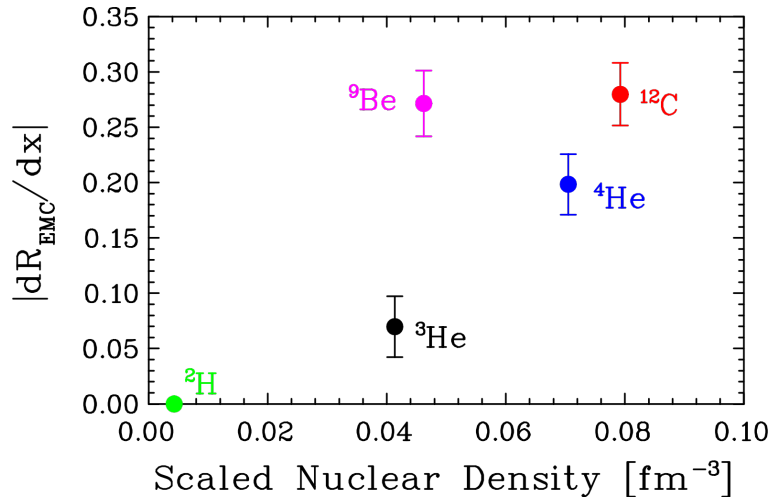


Figure 2.7: Isoscalar EMC effect as function of nuclear density [65].

602 **2.4 EMC Theory and Models**

603 Since the founding of the EMC effect, there have been numerous amounts of work
604 conducted on the theories to describe these EMC ratios. The models attempt to
605 characterize both the nuclear and nucleon structure functions for the entire range of
606 x from 0.0 to 1.0. This section will briefly discuss the basic idea of a few EMC models.

607 **2.4.1 Multiquark Cluster**

608 The multiquark cluster model discussed by K. M. Hanna et. al. [39] and R. L.
609 jaffe [44], states that it is possible to form color singlet quark clusters inside of a
610 dense nucleus. These quark clusters can contain $3N$ quarks (3,6,9...) [59]. These
611 quark clusters have the possibility to contain the momentum of multiple nucleons
612 [26]. Because of the overall momentum of these clusters, the multiquark cluster
613 models makes predictions for high x , but these clusters are not understood enough
614 to make predictions at low x [33, 18, 39, 26].

615 **2.4.2 Nuclear Binding**

616 Describing the EMC effect via nuclear binding was first attempted by Akulinechev
617 et. al. [4] and Dunne and Thomas [28]. For the nuclear binding model, an average
618 nucleon has a momentum and separation energy defined as \vec{p} and $\langle \epsilon \rangle$ respectively
619 [59]. The inclusion of the separation energy in the definition of the momentum of
620 the post scattering A-1 system causes a manipulation in the value of x . x becomes
621 $x' = \frac{Q^2}{2p' \cdot q}$, where p' is $(M + \epsilon, \vec{p})$ [59]. The modification of the momentum through
622 nuclear binding allows this EMC model to explain the EMC effect and the sharp rise
623 in the fermi motion area but fails to correctly describe the rise in the anti-shadowing
624 region around $x = 0.2$ [17, 18, 26].

625 **2.4.3 Medium Modification**

626 Smith and Miller [67] claim that measurements of nuclear observable could be
627 explained by modifications of the nuclear structure due to the medium. The medium
628 is filled with external fields created by the surrounding nucleons. These fields modify
629 the quark waveform of a single nucleon. Using medium modifications C. Cloet, W.
630 Bentz, and A. W. Thomas [23] were able to describe the EMC effect for a collection
631 of nuclear targets and calculate the correct A dependence of the EMC effect.

632 **2.4.4 Rescaling**

633 Nachtmann and Pierner [57] and Close et al [24] discovered a way to relate the DIS
634 structure functions of Fe and D with scaling variable. They found that by using a
635 relative shift in the scale of the Q^2 value that $F_2^{Fe}(Q^2) = F_2^D(\xi Q^2)$ [33]. Both teams
636 proposed that as nuclei get heavier their quarks are bound in an area larger compared
637 to the confinement area for a free nucleon. This dynamic rescaling model is applicable
638 for $0.2 < x < 0.8$, but does not match the EMC ratio for the Fermi motion region
639 with $x > 0.8$ [18, 24, 33, 57].

640 The models discussed here are only a small subset of the models that have been used
641 to describe the EMC ratios. The downfall for most of these models is the inability to
642 consistently predict the EMC ratio for all nuclear targets and the entire range of x in
643 DIS. In order to better constrain the EMC effect and gain a better understanding of
644 DIS, we need to conduct more experiments directly targeting specific regions of the
645 complex problem.

646 **2.5 MARATHON**

647 Experiment E12-010-102, MARATHON (MeAsurement of the $F_2^n/F_2^p, d/u$ RAtios
648 and A=3 EMC Effect in Deep Inelastic Electron Scattering Off the Tritium and

649 Helium MirrOr Nuclei), will use deep inelastic scattering off of the mirror nuclei ^3H
650 and ^3He to measure the EMC effect for both ^3H and ^3He , to determine the ratio of
651 the neutron to proton inelastic structure functions, and to find the ratio of the down
652 to up quark distributions in the nucleon [25].

653 The MARATHON experiment will provide DIS data to determine the EMC effect
654 for the two A=3 mirror nuclei. Previous experiments to measure the ^3He EMC ratios
655 were able to gather data at low and medium x for DIS kinematics, and data in the
656 resonance region for higher x . The data gathered from this experiment has provided
657 the first DIS data in the high x region. The DIS data on ^3H will be able to provide
658 the first-ever measurement of the EMC effect for ^3H covering a large range of x from
659 0.2 to 0.8.

660 The goal of my research is to use the data from the MARATHON experiment
661 to determine the EMC effect for both of the A=3 systems. The following chapters
662 will describe how that was achieved. Chapters will include the information on the
663 production and detection of electrons, the analysis steps to count electrons, the
664 method of measuring the cross-section, and the extraction of the EMC effect.

665 Chapter 3

666 Experimental Setup

667 3.1 Thomas Jefferson Lab

668 Thomas Jefferson Lab (Jlab) in Newport News, Virginia hosted the MARATHON
669 experiment in the Fall of 2017 and Spring of 2018. Jlab uses support from the U.S.
670 Department of Energy(DOE) and the state of Virgina to complete the lab's mission of
671 delivering productive research by exploring the atomic nucleus and its fundamental
672 constituents, including precise tests of their interactions. Along with applying an
673 advanced particle accelerator, particle detectors and other technologies to develop
674 new basic research capabilities and to address the challenges of a modern society.

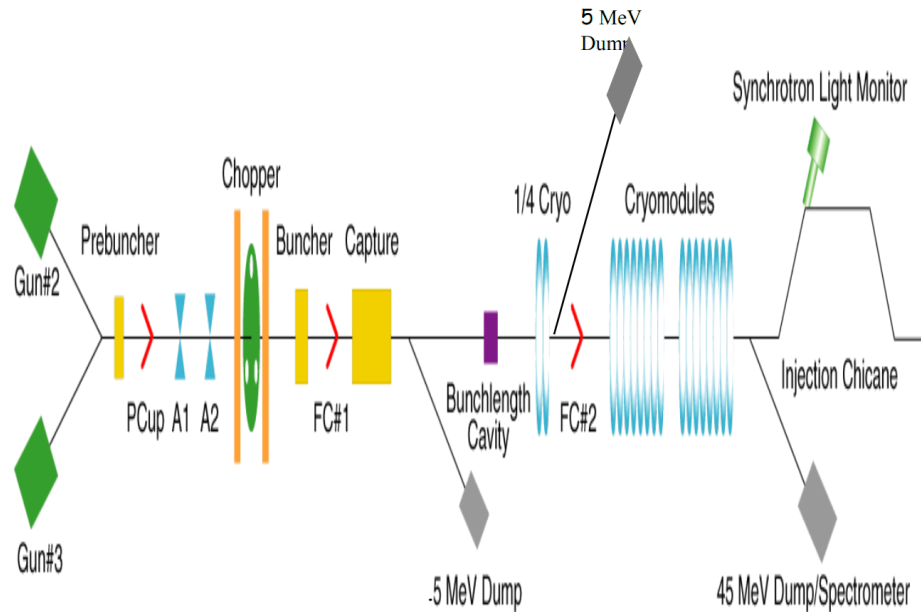
675 3.1.1 CEBAF

676 The Continuous Electron Beam Accelerator Facility (CEBAF) was recently
677 upgraded to a 12 GeV accelerator, upgrading it to be able to supply a 11 GeV
678 beam of continuous electrons of up to $200 \mu\text{A}$ of current to three experimental halls
679 (A,B,C) and 12 GeV to the recently constructed hall D.

680 3.1.2 Injector

681 CEBAF uses a micro-pulsed structure from the photo-electron gun to produce
682 electrons in an efficient manner. This micro-pulsed structure is used to prolong the
683 lifetime of the photocathode. The delivery of unique current and energy to all four
684 halls requires the micro-pulses to have a 250 MHz or 500MHz structure and four
685 individually tuned lasers. Frequencies of 250 MHz and 500MHz are chosen because
686 these are sub-harmonics of the fundamental accelerator operating frequency of 1500
MHz.

Figure 3.1: Drawing of the Injector layout.



687

688 Electrons are produced when laser light shines on a gallium arsenide photo cathode.
689 A laser pulse excites electrons from the photo cathode via the photoelectric effect.
690 These excited electrons form from the gallium arsenide wafer when the electrons are
691 excited out of the valence band into the conduction band. Gallium arsenide was
692 chosen because the energy level of the conduction band for this photo cathode sits
693 above the energy of an electron vacuum. Electrons in the conduction band escape

694 from the material and are accelerated away from the wafer due to high negative
695 potential on the photo cathode wafer [56].

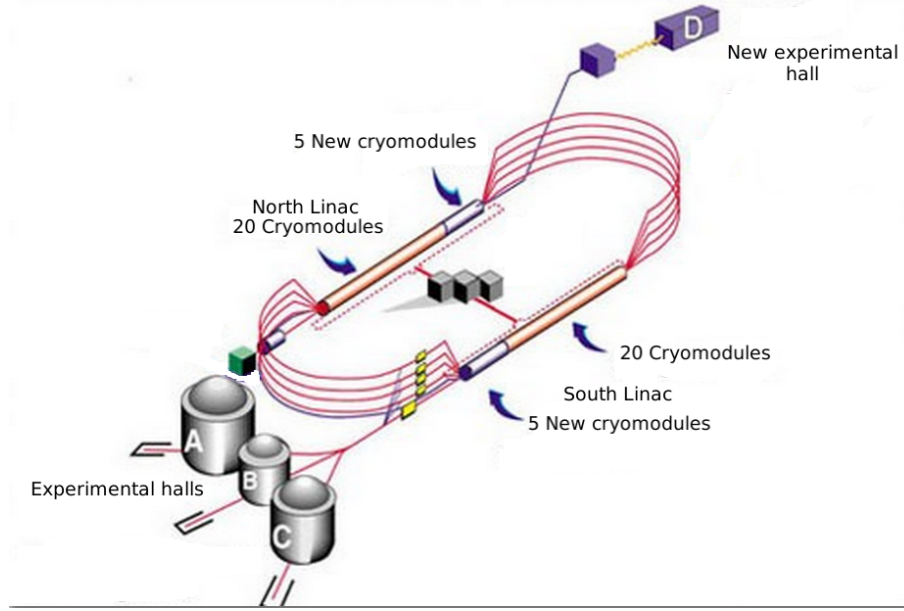
696 These electrons are accelerated into the injector beam line via the electron gun.
697 Tunning the amount of electrons in a bunch happens at the chopper. Slits in the
698 chopper allow for greater regulation of the currents sent to the four experimental
699 halls. Testing and calibration of the four beams are done throughout the injector
700 beam lines via the Faraday cups located at different spots in the beam line. The
701 polarized gun can supply electrons with up to 80% polarization and the polarization
702 direction can be controlled by a wien filter. To ensure the level of polarization, a
703 5 MeV Mott polarimeter may be used to measure the level of polarization[5]. The
704 injector accelerates the electrons up to 123 MeV before allowing them into the north
705 LINAC [50, 61, 47].

706 3.1.3 Accelerator

707 The electrons are conveyed through two LINACs and two bending arcs per complete
708 pass of the accelerator. The two LINACs are approximately a quarter mile long and
709 are thirty feet below the surface. The beam lines are kept under vacuum between
710 E^{-6} and E^{-11} torr to provided an efficient medium for transfer. Electrons traveling
711 to Halls A, B, and C complete a maximum of four and a half revolutions around the
712 accelerator. These particles receive approximately 2.2 GeV in energy for each cycle
713 through the accelerator.

714 The radio frequency (RF) cavities in each LINAC use an oscillating electromagnetic
715 field to supply a force to accelerate the passing electrons. These Niobium RF
716 cavities are cooled to 2 K in order to create conditions that allow the cavities to be
717 superconducting [5]. The superconduction RF(SRF) cavities provided a negatively
718 charge field behind the electrons and positively charged field in front to accelerate
719 the electrons through a set of cavities inside a cryomodule. A central helium liquefier

Figure 3.2: Schematic Layout of CEBAF.

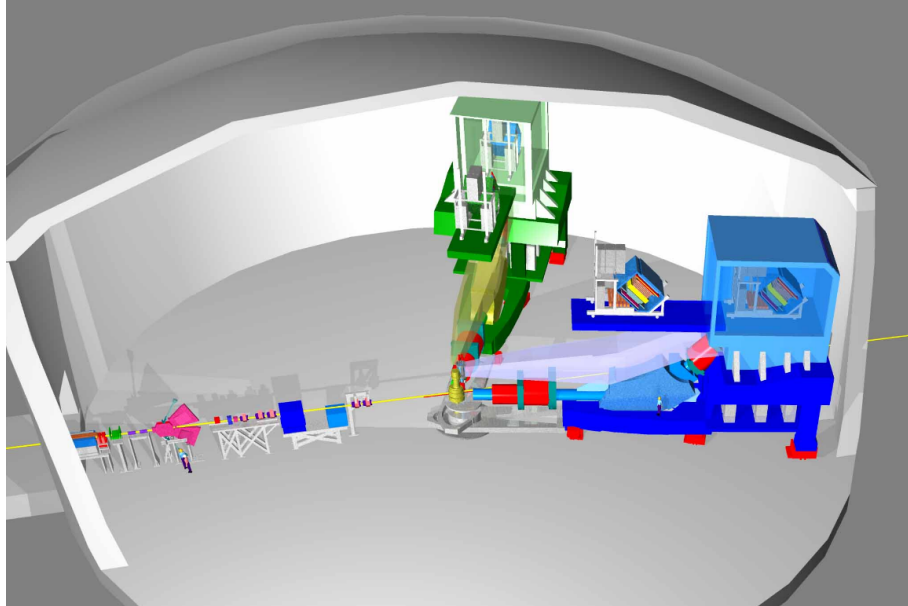


720 circulates up to 17000 gallons of chilled liquid helium to control the temperature of
721 the cryomodules. A dedicated 5 kW klystron provides a 1500 Mhz RF driving signal
722 for each cryomodules.

723 The electron beam exiting the north LINAC enters the east arc. The east and west
724 arcs contain large dipole and quadrupole magnets to steer and focus the beam as the
725 beam is accelerated back to the other LINAC. After electrons exit the south LINAC,
726 they either continue on around the accelerator for another pass to increase in energy,
727 or a RF separator projects the electron beam into the proper experiment hall [50].
728 Energy loss, beam position, and beam charge monitors lie throughout the beam line,
729 and are used to insure the quality of beam delivered to the experimental halls.

730 **3.2 Hall A Beam Line**

Figure 3.3: A 3D drawing of Hall A.



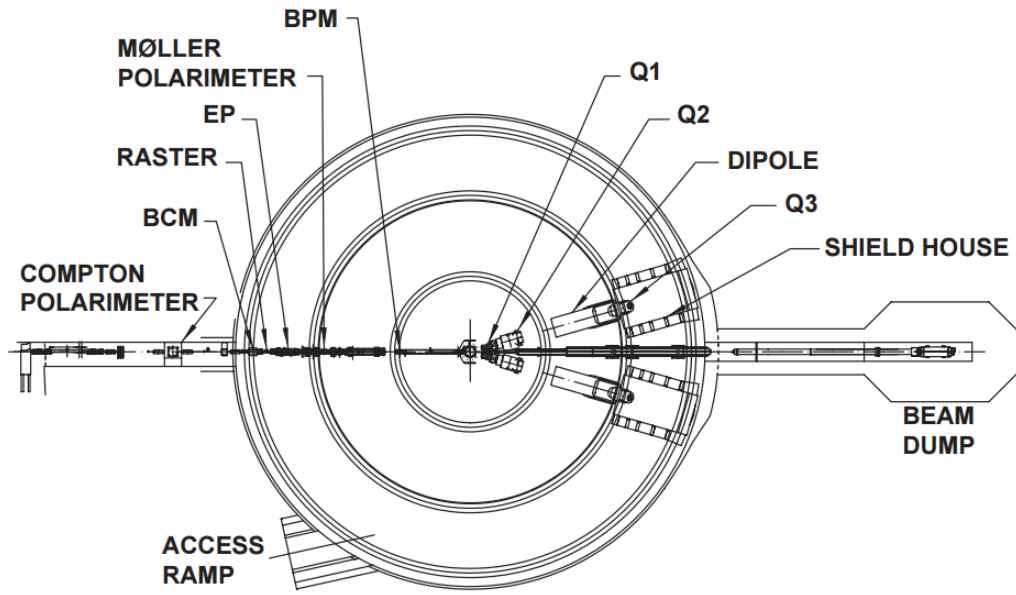
731 The experimental Hall A and the scientific equipment used were designed for
732 detailed investigations of the internal structure of nuclei. Two high resolution
733 spectrometers in Hall A use the inclusive (e,e') and exclusive $(e,e' p)$ reactions to gain
734 a greater understanding of the structure of the nucleus. Completing detailed studies
735 with high resolution and extreme accuracy requires knowing the beam position, size,
736 energy, and current when the beam strikes the target. The instrumentation used in
737 the precise measurement of these quantities in Hall A are shown in figure 3.4 [5]. The
738 information provided by these detectors originate through small changes in current
739 and voltage sent through the electronics. These signals are transformed into useful
740 information through calibrations.

741 **3.2.1 Beam Position Monitors**

742 A pair of Beam Position Monitors(BPM)s are used to measure the relative beam
743 position without affecting the beam. The two Hall A BPMs are located at 7.524 m

744 and 1.286 m away from the target. Using the standard difference-over-sum technique,
 745 the relative beam position is determined with an accuracy of 100 μm with a beam
 746 current of at least 1 μA [5]. The BPMs' positional data is recorded in two ways.
 747 Every second of beam time, the beam position average over 0.3 seconds is logged
 748 into the Experimental Physics and Industrial Control System (EPICS) database.
 749 The BPMs also transmit data event-by-event to the CEBAF online Data Acquisition
 750 system(CODA).

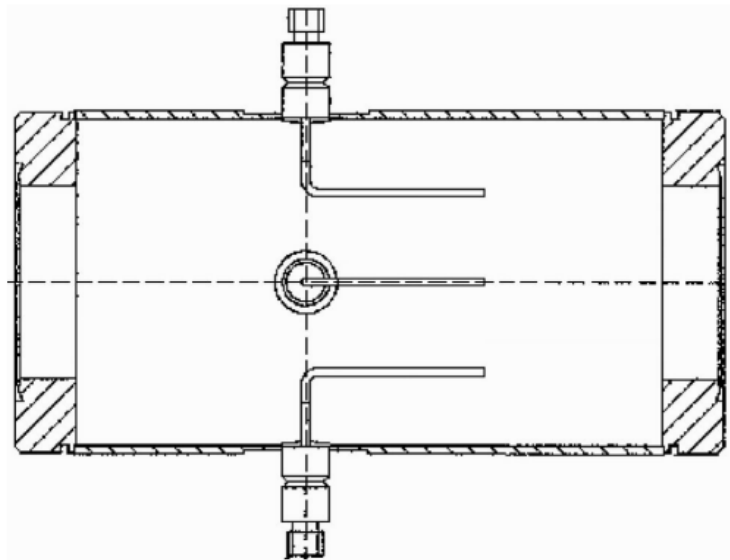
Figure 3.4: A schematic layout of the beam line in Hall. [5]



751 The main beam line components of the BPMs consist of four open-ended antennas.
 752 Figure 3.5 shows a BPM chamber and figure ?? shows the layout of the four antennas
 753 as you look down the beam line. In this chamber, the design of three of the four
 754 antennas can be seen. The antennas are titled u_+ , u_- and v_+ , v_- . The antennas
 755 receive an induced signal as electrons pass to determine the beam position in the
 756 u and v directions. The BPMs send a DC offset to the DAQ. This DC offset is
 757 turned into a positional measurement via looking at both signals in one direction.
 758 The position in the frame of the u and v antennas are calculated by taking the

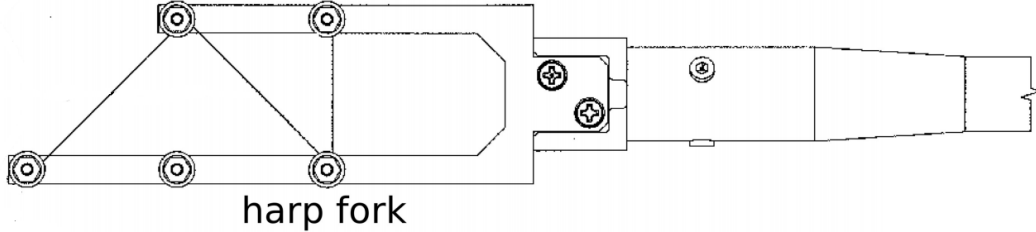
759 difference over the sum of the two wires in the u and v directions. The accuracy of the
760 BPMs requires an absolute measurement of the electron beam's position to calibrate
761 the BPMs[64, 71].

Figure 3.5: BPM design diagram, from JLab instrumentation group. Beam direction is from left to right [71].



762 Two harps were used to provide the absolute measurement required for the
763 calibrations. Each harp is located immediately after the BPM on the beam line.
764 The harp forks are aligned perpendicular to the beam line to allow the harps to be
765 moved in and out of the beam line. A wire that transverse between the fork tines
766 at three different angles in respect to the harp is used to determine the horizontal
767 and vertical position of the beam. The two sloped sections of the wire are angled at
768 45° relative to the harp frame. As the harp fork is moved into the beam, the wires
769 receive a signal as the beam interacts with the wires. The two sloped wires are used
770 together to determine the vertical position of the beam. The vertical wire is used to
771 determine the horizontal position of the beam [64, 71]. The harps are not used during
772 production phases due their intrusive nature caused by the interaction of the beam
773 with the harp wire.

Figure 3.6: A schematic layout of a harp fork [71]



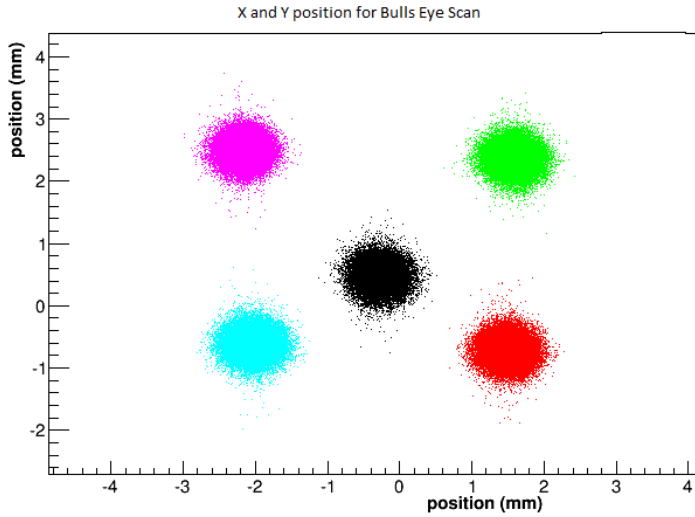
774 The location of the wires on the harp frame and the position of the harp fork were
 775 used to calculate the absolute beam position. Figure 3.7 shows an example of five
 776 positions used to calculate the BPM calibration coefficients. This method of using
 777 beam positions at the nominal center and surrounding the center is called a bull's
 778 eye scan. The harp scan results are substituted into equation 3.1 for the X and Y
 779 positions. Using all five points and an R^2 regression technique, the coefficients can
 780 be determined with great accuracy. These highly accurate BPMs were crucial in
 781 reducing systematic error in the final results obtained from this experiment.

$$\begin{pmatrix} X_{position} \\ Y_{position} \end{pmatrix} = \begin{pmatrix} C(0,0) & C(0,1) \\ C(0,0) & C(0,1) \end{pmatrix} * \begin{pmatrix} X_{BPM} \\ Y_{BPM} \end{pmatrix} + \begin{pmatrix} X_{offset} \\ Y_{offset} \end{pmatrix} \quad (3.1)$$

782 3.2.2 Raster

783 Damage to a target system from intense beam can cause extreme fluctuations in
 784 the target's temperature and density. A raster was used to counteract the damage
 785 caused by a focused beam. The raster used two magnetic fields produced by two
 786 dipoles to spread the electron beam out. This produces a large rectangle interaction
 787 area on the front face of the target container. A triangle wave of 25 kHz was used to
 788 control the coils of the dipole magnets. The raster systems are located ≈ 17 meters
 789 before the target chamber (upstream of the target[71]). The rasters position can be
 790 seen in figure 3.3. Safety constraints administrated by the target group at JLAB

Figure 3.7: The X and Y position for a Bulls eye scan for BPM calibration.



791 limited the minimum size of the raster spot for the MARATHON experiment to two
792 millimeters by two millimeters. This limit was installed has a safety concern for the
793 tritium target.

794 The Hall A raster system consists of four dipoles. Two dipoles produce magnetic
795 fields in the horizontal direction of the lab frame and two in the vertical. The upstream
796 raster and downstream rasters include one vertical and one horizontal dipole. The
797 relative change in position of the incoming electrons are controlled by the current
798 supplied to the dipoles. This current that drives the dipoles is recored by an ADC. In
799 order to obtain the change in beam position due to the rasters, a calibration between
800 the raster current and measured beam position were obtained.

801 The raster calibration is done by creating a line that maps the raster current
802 measured by ADC bins to a position. This calibration process is done to extract
803 positions at the locations of both BPMs and the target center along the beam line.
804 The calibration of the linear mapping of raster current to beam position took two
805 process. The first process was to determine the size of the rastered beam spread. In

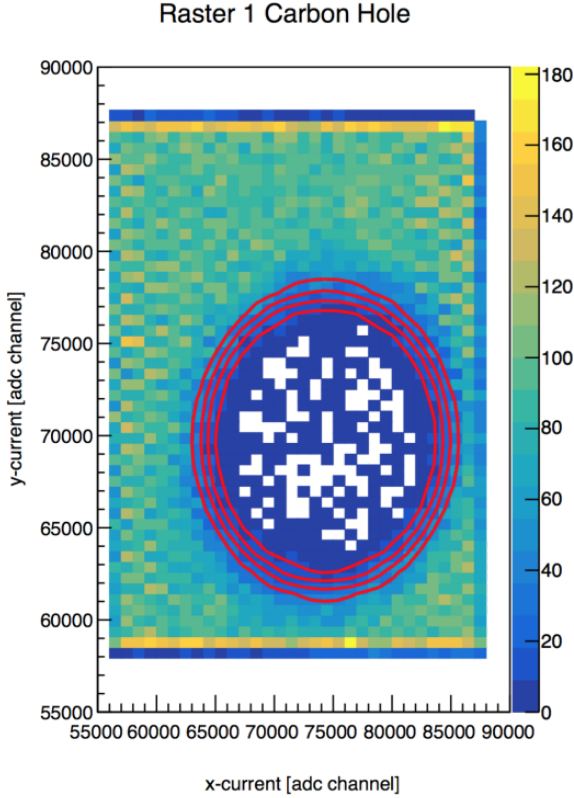


Figure 3.8: The X and Y current of the raster with a carbon hole. The size of the carbon hole is fit with a radial sigmoid[38].

order to accurately determine the width and height of the beam spread due to the raster, a carbon foil with a hole of a diameter of 2mm was used. A radial sigmoid was used to fit the hole. The fit of the carbon hole gives the width of the raster, the slope of the linear mapping term. In figure 3.8, the raster current in x and y directions are fitted using this radial sigmoid. Once the slope of the linear calibration is determined, the offsets can be found. This is discovered by using the calibrated BPM mean positions for a phase of rastered beam. The mean positions for both BPMA and BPMB are used to produce a track from the BPMs to the target. This projection provides a mean location of the beam at the target. Using equation 3.2, the offsets also known as the intercepts can be solved for using the slope (m_x, m_y), the

816 raster mean current value (R_x, R_y), and the mean BPM position(x, y). [38]

$$\begin{pmatrix} x \\ y \end{pmatrix} = \begin{pmatrix} R_x \\ R_y \end{pmatrix} * \begin{pmatrix} m_x & 0 \\ 0 & m_y \end{pmatrix} + \begin{pmatrix} O_x \\ O_y \end{pmatrix} \quad (3.2)$$

817 3.2.3 Beam Energy

818 The electron beam energy is located in many of the equations used in an electron
819 scattering experiment. This can cause a noticeable increase in systematic error if the
820 beam energy measurement is not made precisely. At JLAB for the MARATHON
821 experiment, the beam energy was measured in two ways. In Hall A, the beam energy
822 was measured by using the (e,e/p) method. On the beam line, 17 meters upstream
823 from the target an ep scattering chamber is located. The beam was directed into the
824 target containing a rotating 10-30 μm thick tape of CH_2 . The scattering angle of the
825 electron and the recoil angle of the proton are used to determine the beam energy
826 using equation 3.3. Where M_p is the mass of the proton and θ_p, θ_e are the scattered
827 angle of the proton, electron respectively.

$$E = M_p \frac{\cos\theta_e + \frac{\sin\theta_e}{\tan\theta_p} - 1}{1 - \cos\theta_e} \quad (3.3)$$

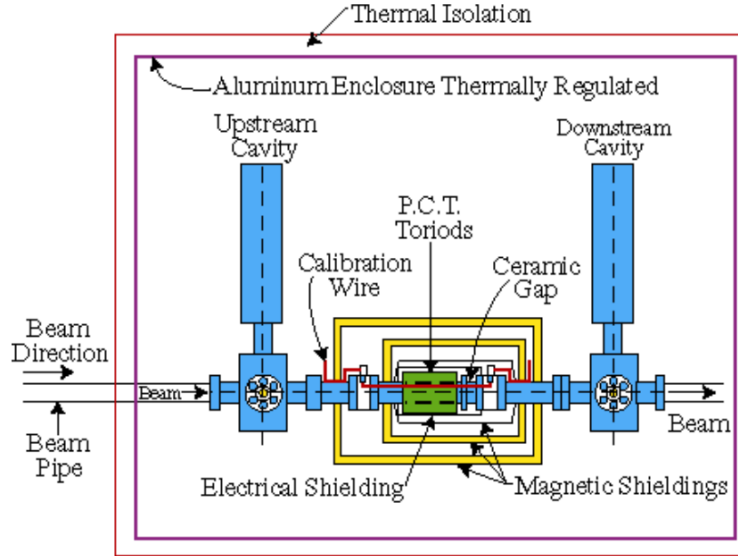
828 The beam energy was also measured using the ark measurement method [31]. This
829 method uses changes in beam position and precise measurements of the magnetic
830 fields around the beam line to determine the energy of the electron beam. The angle
831 at which the electrons are bent through is related to the momentum of the electrons,

$$p = k \frac{\int \vec{B} \cdot d\vec{l}}{\theta}. \quad (3.4)$$

832 In equation 3.4, p is the momentum of the electrons, θ is the bend angle, and \vec{B} is the
833 magnetic field the electron experiences. Then using the momentum of the electron,
834 the energy of the beam can be extracted. The error on the beam energy measurement

835 is $\delta E/E \approx 2 * 10^{-4}$ [69, 31]. The MARATHON experiment used both methods to
836 accurately determine the electron beam energy.

Figure 3.9: Hall A Current Monitor components [27].



837 3.2.4 Beam Current Monitors

838 The main process of measuring the scattering yield for a calculation of a cross
839 section looks at finding the ratio of the number of electrons scattered to the number of
840 electrons sent. In order to accurately determine the number of electrons sent to scatter
841 with our target system, Hall A use a set non-invasive beam current monitors(BCMs).
842 The Hall A BCMs have an absolute accuracy of 0.2 percent as long as the current is
843 between 1 and 180 μA . The BCMs used in Hall A consist of three main components:
844 a Parametric Current Transformer (PCT) and two pill box cavities. Figure 3.9
845 shows the components in the Hall A BCM. The BCM produces an RF signal that is
846 proportional to the beam current. A 10 kHz down converter, RMS-to-DC converter,
847 voltage-to-Frequency converter, and a scaler are used to inject the current signal
848 into the Hall A DAQ. Proportionality constants are determined in the calibration
849 process to correctly integrate the charge for a given amount of beam current[27]. The
850 process of calibrating the BCM converts the frequency received from the BCMs to

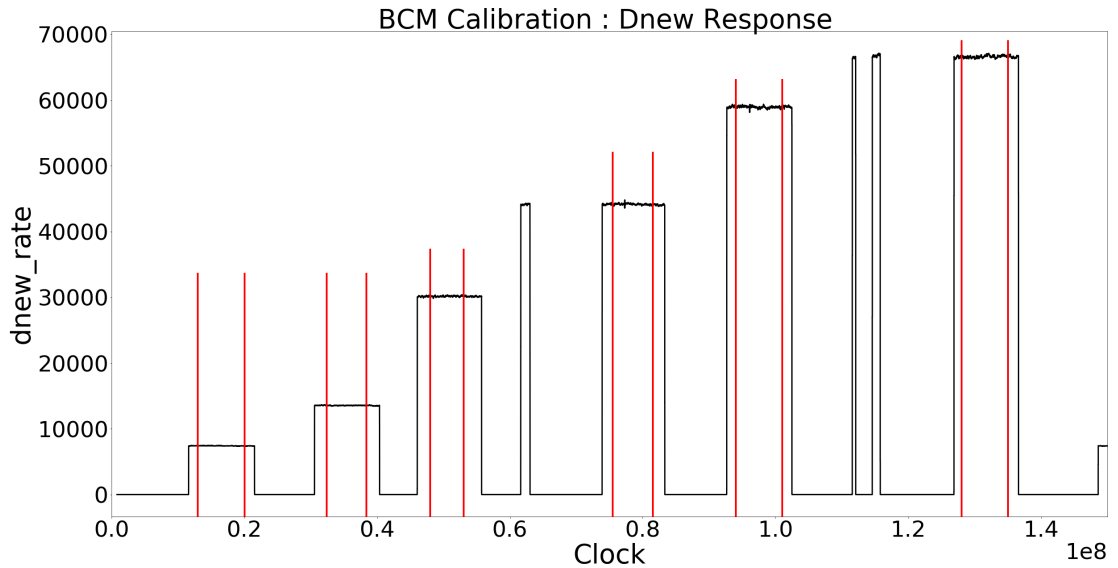


Figure 3.10: BCM calibration [60].

851 an amount of current in μA . In order to calibrate the BCMs in Hall A, a separate
 852 intrusive calibration of an unser must be done. The unser is calibrated by inserting a
 853 known current through a wire inside the beam pipe. The calibration of the unser is
 854 known to drift over time, which makes the unser unfeasible to use as the main source
 855 of charge calculation. Once the unser is calibrated, the BCM calibration procedure
 856 can be completed. The BCM calibration requires the delivery of the electron beam
 857 with unique procedure. This process consist of oscillating the beam on and off status
 858 while increasing the current. This process can be seen in figure 3.10. This stepping
 859 up procedure provides an adequate number of data points to complete a linear fit
 860 of the BCM frequency verses the calibrated unser current. The linear fit parameters
 861 supply a multiplicative gain and an additive offset for the calibration of the BCMs.
 862 Figure 3.11 shows a linear fit that provides gain and offset calibration constants for
 863 the BCM used in the calculation of charge.

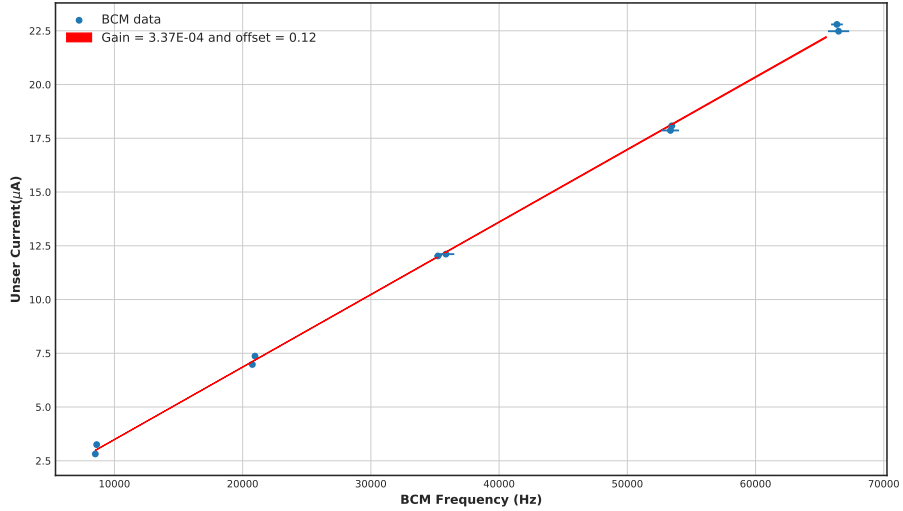


Figure 3.11: BCM frequency for BCM calibration [60].

864 3.3 Target

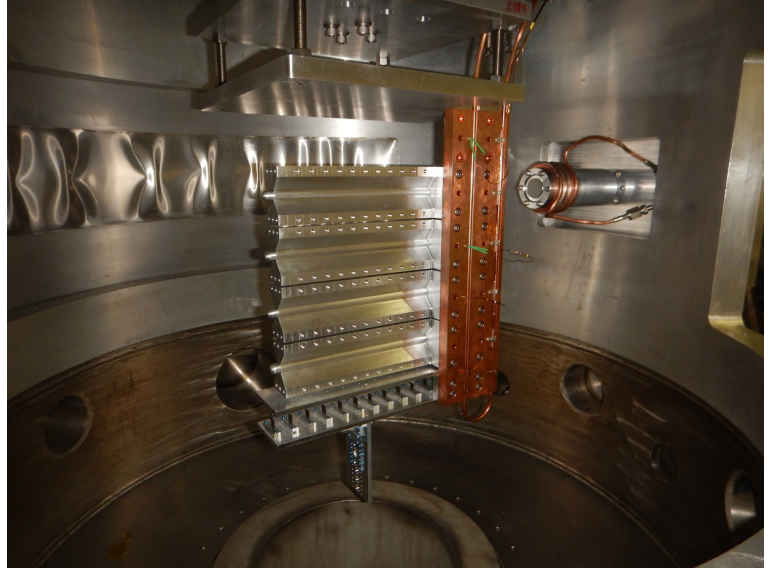
865 The Hall A Tritium Target(HATT) system was used for the Tritium run group of
 866 experiments. The HATT target chamber was repurposed from a previously used cryo-
 867 target chamber in order to reduce the financial cost of designing a new target chamber.
 868 The refurbishing of the cryo-target chamber consisted of adding in new safety features
 869 to prevent and mitigate a tritium leak. A 4 inch long collimator with an inner diameter
 870 of 0.4 inch was added inside of the target chamber but upstream of the target ladder
 871 to prevent the beam from striking the thin side wall of the aluminum cell. In case of
 872 a tritium leak in the target chamber, an exhaust system was installed to control the
 873 amount of tritium exposed to the Hall.[55] Figure 3.12 shows the HATT system with
 874 the target ladder in the home position and the scattering windows removed. A picture
 875 of the HATT ladder installed in the HATT system is shown if figure 3.12. The ladder
 876 contains both gaseous cells and solid targets. The MARATHON experiment had five
 877 gas cells. The top four of the gas cells were filled with tritium, deuterium, hydrogen,
 878 and $^3\text{helium}$, from top to bottom respectively. Due to safety restricts the tritium
 879 cell was not installed until the HATT system could be closed. The bottom most
 880 cell was left empty, to complete end cap subtractions. The lower half of the target

Figure 3.12: Target Images

(a) A image of the HATT. [42]



(b) Image of the Hall A Tritium Target Ladder. [42]



881 ladder contains the solid targets used during the MARATHON experiment. Listed
882 from top to bottom, the solid targets used were a pair of thick aluminum foils, carbon
883 multifoil, single carbon foil, and a carbon foil with a 2mm diameter hole. The thick
884 Al foils were used to aid the target window background subtraction. The multifoil
885 target also known as the optics target was used to calibrate the z-axis reconstruction
886 of the optics matrix. The single carbon foil and carbon hole were used to calibrate
887 the BPMs and rasters and to determine the off set of the central line of the detector.

888 **3.4 High Resolution Spectrometers**

889 Electrons that successfully scatter from the target may end up in either of the two
890 HRSs(High Resolution Spectrometers). The HRSs were designed to detect charged
891 particles with a high degree of precision. In order to achieve a high level of resolution
892 in momentum and angle, the HRSs were designed with a magnet configuration of
893 QQD_nQ (quadrupole, quadrupole, dipole, and quadrupole). The vertical bending

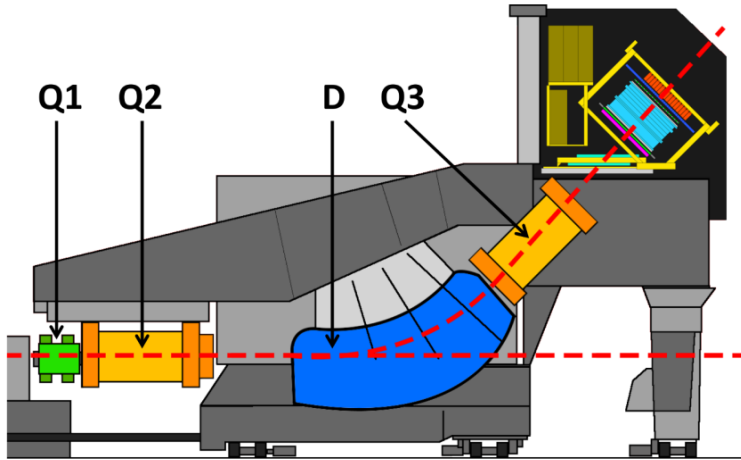


Figure 3.13: A side view of a HRS [5].

894 dipole provides the field required to transport the scattered particles through the
 895 45° bending angle to the detector hut. A drawing of an HRS can be seen in
 896 figure 3.13. The first quadrupole(Q1) focuses the incoming electrons in the vertical
 897 plane. The following two quadrupoles (Q2 and Q3 provide transverse focusing. This
 898 optical design allows the use of extended gas targets with no substantial loss in solid
 899 angle[5]. The spectrometers were designed to perform various functions which include:
 900 triggering the data acquisition system (DAQ) when certain requirements are met,
 901 gathering the position and direction of individual particles to reconstruct a track,
 902 provide precise timing information for time of flight calculations, and identify many
 903 different particle types that pass through the detector system. In order for both
 904 the Left HRS (LHRS) and Right HRS (RHRS) to complete the required task, they
 905 contain a myriad of detectors. The HRSs use drift chambers, scintillators, cerenkov
 906 detectors, and shower calorimeters. Both the Left and Right HRSs contain two planes
 907 of scintillators to function has the main trigger for the detector package. The vertical
 908 drift chambers (VDC) that lay at the front of the detector in conjunction with the
 909 Shower that lies in the back of the detector provide information for reconstructing the
 910 particle tracks and precise timing. Particles are identified by the cerenkov, shower
 911 calorimeters, and pion rejectors that are contained in the left or right HRS. The

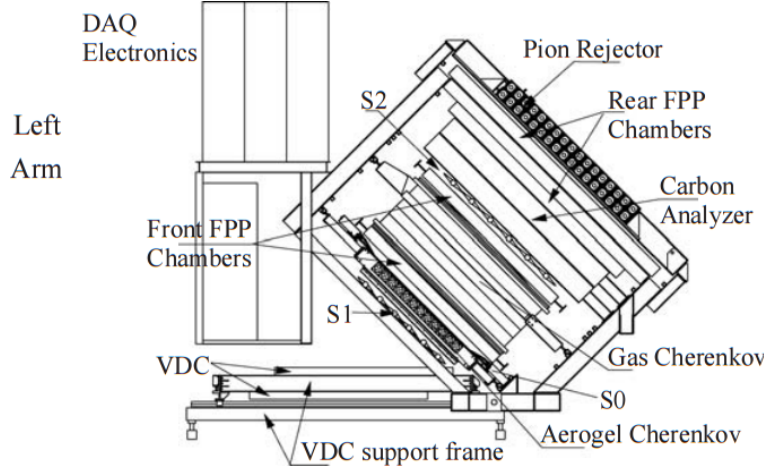


Figure 3.14: A view of both the left (top) and right (bottom) detector stacks inside the left and right HRS [5].

912 layout of the individual detectors that make up the left and right detector package
 913 are shown in figure 3.14 [5].

914 3.4.1 Vertical Drift Chambers

915 Each of the spectrometers housed in Hall A contains two vertical drift cham-
 916 bers (VDC). Each VDC incorporates two planes of crossing sense wires. Shown in
 917 figure 3.15, the two planes of the VDC lie a distance of 0.335m apart [30]. The lower
 918 plane of the VDC is positioned at the approximate focal plane of the HRS and lies
 919 in the horizontal plane of the Hall A coordinate system. The sense wires located in
 920 the VDCs cross orthogonally. They are offset by 45° in respect to the dispersive and
 921 non-dispersive directions. Each plane of the VDC uses 368 sense wires, with 4.24 mm
 922 between each wire. The signals from these wires are transmitted to the electronics via
 923 a set of printed circuit boards that contain a 16-channel connector and twisted pair
 924 ribbon cables. These ribbon cables transmit the VDC signal to a set of common stop
 925 TDC with 0.5 ns resolution [30]. The VDC sense wires are held at ground potential
 926 between two planes of high-voltage. Particles that enter the gas filled VDC, collide
 927 with molecules of an argon (62%) and ethane (38%) mixture [5]. This collision causes
 928 the ionization of the gaseous mixture producing drift electrons.

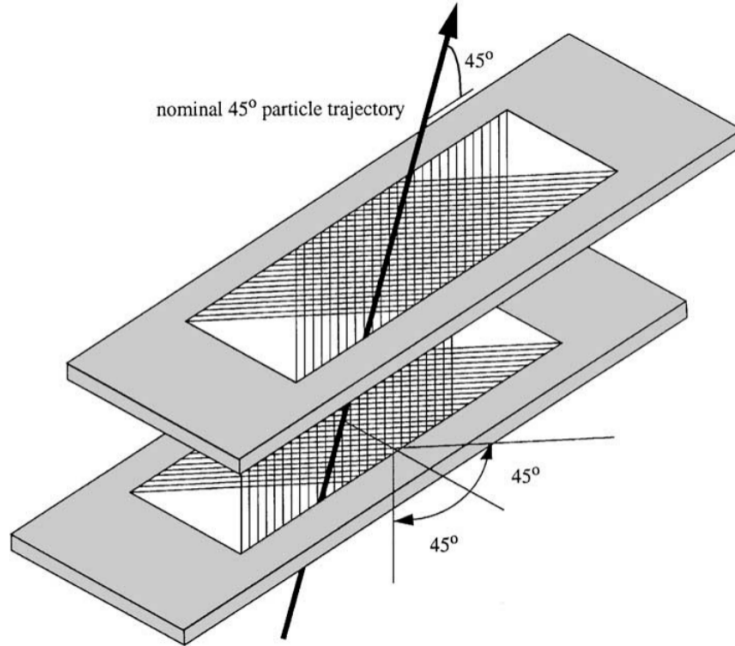


Figure 3.15: A sketch of the two VDC planes in the HRSs with a particle traveling through the detector at 45° .[30].

929 Particles that transverse the VDCs will travel through regions close to several sense
 930 wires. As the indecent particle ionizes gas in each of these regions, the VDC sense
 931 wires pick up the corresponding signal from the drift electrons. The drift electrons
 932 will travel to the sense wires via the parallel electron field lines until the electrons get
 933 close to the sense wires. Once close the sense wires, the electron field transitions to
 934 a radial field and the drift electrons then move to the sense wires. An example of a
 935 drift electron's trajectory is shown in figure 3.16, in which a cluster of 5 wires sense
 936 scattered particle.

937 The drift chamber's performance is constantly monitored throughout the experi-
 938 ment. The efficiency of an individual wire is determine by an algorithm that scans a
 939 plane for an event that fires a cluster of wires. A wire is determine to be efficient for
 940 that event if it fired along with it's two nearest neighbors. This efficiency calculation
 941 is used during the online analysis to keep track of the performance of the VDCs and
 942 to assistant the maintenance of the HRSs throughout the experiment.

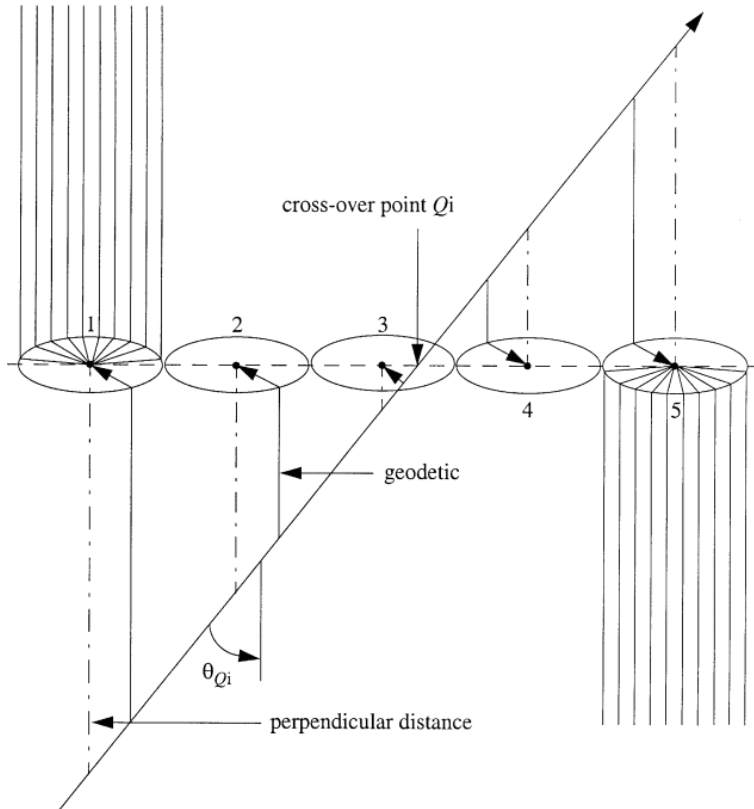


Figure 3.16: A possible track that causes signals in wires. The drift electrons will follow the arrow path. The dot/dashed lines correspond to the projected distance used to reconstruct the path of the incident particle. The transition point from parallel to radial field lines is represented by the ellipses. [30]

943 The VDC's main task during an electron counting experiment is to determine
 944 the track of the scattered electron. The track of the electron is used to ascertain
 945 the electron's scattering momentum and scattering angle. Due to the electron's
 946 relativistic nature the primary ionization event for each wire region happens
 947 simultaneously compared to the resolution of the TDCs. The common stop TDCs
 948 used for the VDC signals record the amount of time from drift electron's signal in
 949 the sense wires to the stop signal formed by the trigger. This creates a high TDC
 950 signal for short drift distances. The raw TDC values recorded by the VDC include
 951 time associated with the signal but also the time required to form the trigger and
 952 time of flight for electrons between the VDCs and detectors used in the formation of a
 953 trigger. The calibration of the VDC removes these extra sources of time in the TDC

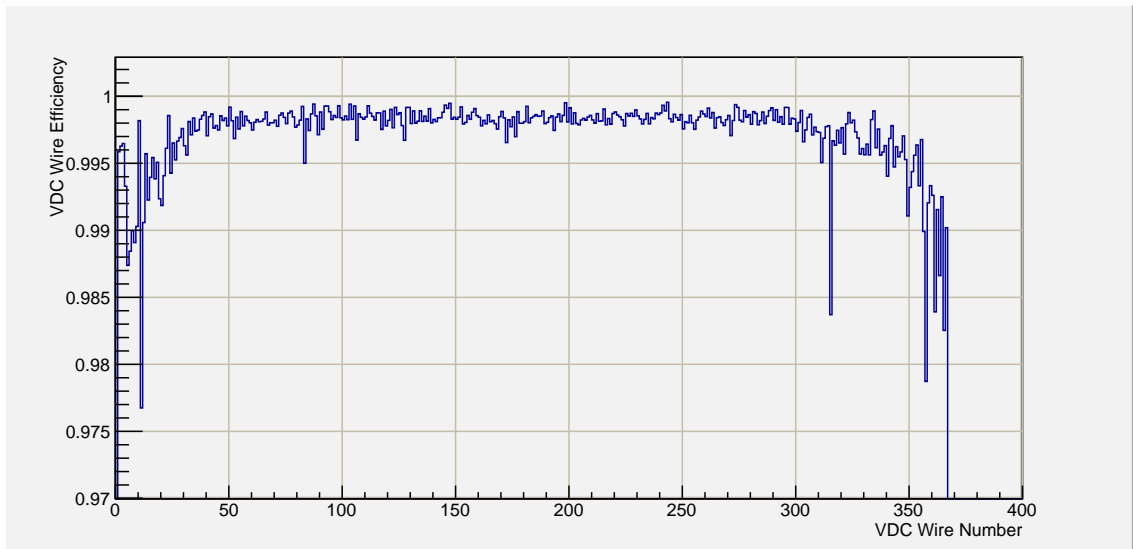


Figure 3.17: The VDC efficiency for one plane of wires.

954 signal. In order to calibrate the VDC raw signals, a reference time is determined for
 955 every wire on every plane. This references time (t_0) is chosen as the TDC value of
 956 the sharp decrease on the outside of the peak in region C shown in figure 3.18. The
 957 time recorded from the TDCs is used to construct a location of the ionization event
 958 for each sense wire across the trajectory of the scattered electron. The analyzing
 959 software will use these drift distance from the four VDC planes to find a track for the
 960 scattered electron.

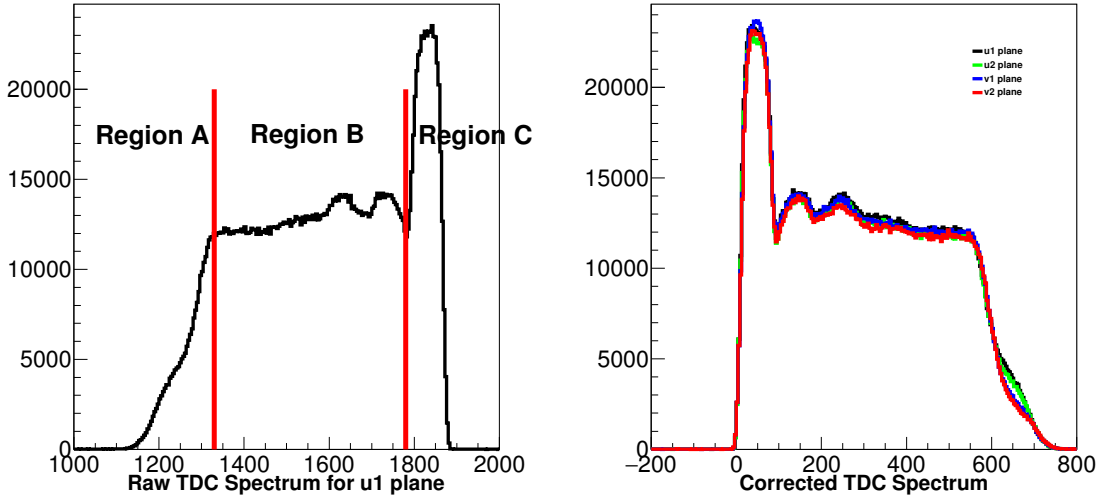
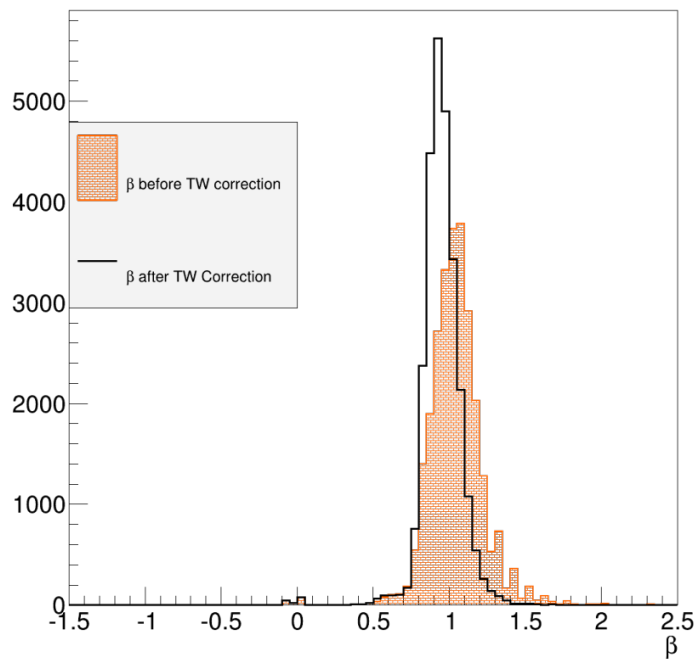


Figure 3.18: Histograms of VDC signals before(left) and after(right) calibration of t_0 [45].

- Region A: In this region, the point of primary ionization is far from the sense wire. As this distance increases, the chance of detecting the transversing particles by this wire is decreased.
- Region B: The probability of sense wires detecting a primary ionization event in this region are uniform due to the uniform electric field though out the region.
- Region C: The primary ionization position for these events are very near the sense wire and the electric field from this area is going to change to radial shape and the probability to detect a particle is going to increase in this area. The sense wire exist in the region, so the ionization event will have a minimum distance. This is shown in the sharp decline on the outside of the peak in region C. [45]

961 3.4.2 Scintillators

962 A pair of scintillator planes form the primary triggering apparatus for the HRSs.
963 The planes of scintillator S0 and S2 consist of a collection of plastic scintillating
964 paddles with photo multiplier tubes(PMTs) attached to both ends of the paddle.
965 S0 the first scintillator in the stack consist of one scintillating paddle in a vertical
966 direction. S2, the second scintillator was build with 16 overlapping paddles with
967 PMTs attached to both ends. As electrons enter the scintillating plastics energy
968 is absorbed by the material scintillating light. This light is detected by the PMTs
969 on either side of the bar. The passing of the electron can happen at positions at
970 an unequal distances from the PMTs on a scintillator bar. These relative differences
971 cause a distortion in the timing calculation in the TOF known as the time walk effect.
972 The scintillators are used in the calculation of β , the v to c ratio. Beta is calculated
973 using the time of flight(TOF) between the two scintillator planes and distance traveled
between the points of interaction. Once calibrated, each plane has a time resolution



974 **Figure 3.19:** Histogram of β before and after time walk correction.

975 of about 0.3 ns. This high time resolution and quick response makes the scintillators
976 the perfect detector to form the main trigger.

977 3.4.3 Cherenkov

978 After a particle passes through S0, it will enter the large gas chamber for the gas
979 cherenkov(GC). The GC is filled with CO_2 with an index of refraction of 1.00041.
980 This high index of refraction creates a momentum threshold of 0.017 GeV/C for
981 electrons, 4.8 GeV/C for pions, and 32 GeV/c for protons[13]. Relativistic particles
982 entering the GC will produce a cone of cherenkov radiation. This cone of light will
983 be focused by a set of mirrors on the back plane of the GC. These mirrors direct
984 the focused light onto a set of PMTs. An depiction of the GC from a top down
perspective is shown in figure 3.20. The raw data recorded from the GC is in the

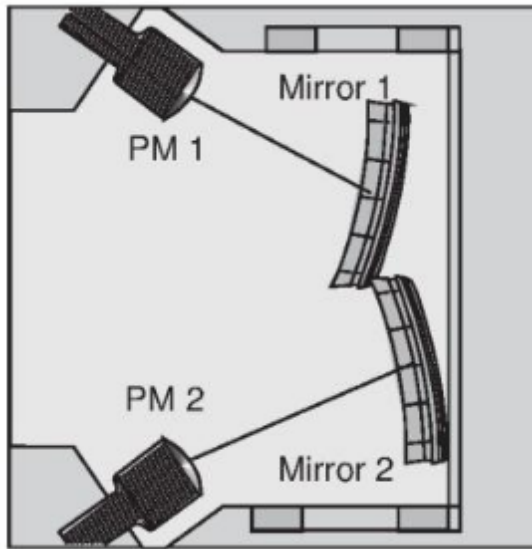


Figure 3.20: Top down depiction inside the GC [13].

985
986 form of raw ADC, or the size of the pulse seen by the PMT. In order to use this
987 information, the ADC input needs to be calibrated. For the GC, two parts of the
988 signal needs to be calibrated. Each ADC channel sees a different amount of noise and
989 signal background from electronic fluctuations. This signal background is defined as

990 the ADC pedestal, and is the first calibration offset determined. Figure 3.21 shows the
 991 raw signal from one cherenkov PMT. This signal shows the pedestal at approximately
 992 5800 ADC channels. The pedestal is subtracted from the raw ADC signal to normalize
 993 the background electronic noise for all PMT-ADC pairs in the cherenkov. The second
 994 calibration for the GC ADC signals is the photo electron peak. The voltage used to
 995 power the PMTs in the cherenkov is tuned before the experiment to allow the PMT
 996 to give the best pedestal to signal ratio while also persevering the life of the PMT
 997 and signal quality. This forces a different signal strength to be seen by each PMT for
 998 the same amount of light experienced in the chamber. The photo electric peak in the
 ADC signal is then normalized to the same value across all PMTs by a gain factor.

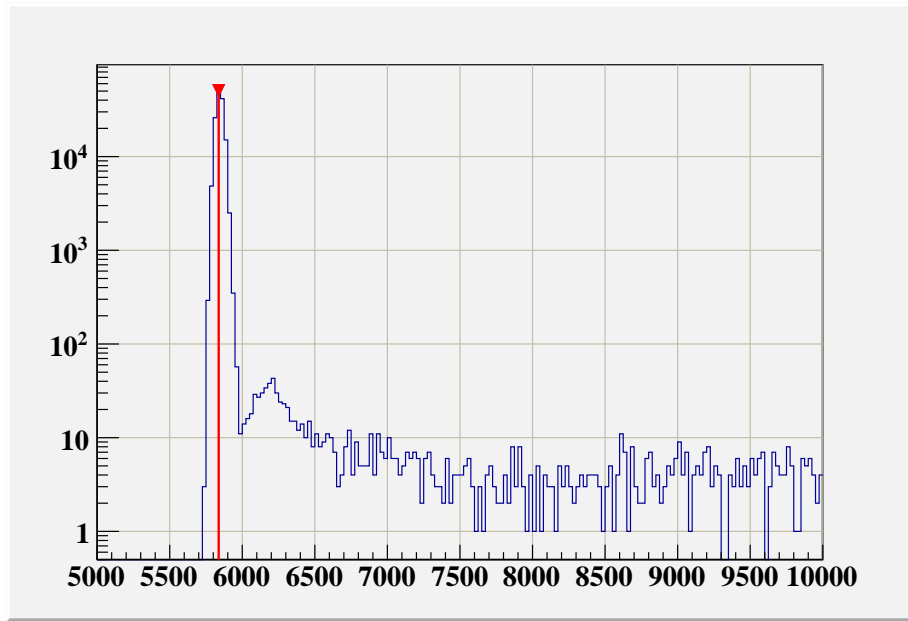


Figure 3.21: The raw signal captured from a single cherenkov PMT, PMT[1], with a fit to the pedestal peak and a line draw to demonstrate its ADC channel number.

999

1000 The GC's main task during an experiment is to help in the identification
 1001 of particles(PID). During the MARATHON experiment, the GC was used to
 1002 differentiate between negatively charged pions and electrons that passed through
 1003 the detector. MARATHON used the GC in PID for data capture and analysis.

1004 During data capture, the GC signal was used in the formation of the main trigger.
1005 Using the GC in the trigger by forcing a certain threshold in signal strength from
1006 the GC, allowed for the exclusion of many unwanted events. During the analysis of
1007 MARATHON data, pion suppression was done using the GC signal and signals from
1008 the calorimeter.

1009 **3.4.4 Calorimeter**

1010 The last detector in the spectrometer that particles interact with is the lead
1011 glass calorimeter. The Left HRS (LHRS) calorimeter system is made up of the
1012 preshower(PS) and shower(SH). The PS contains two columns of 24 blocks of lead
1013 glass with a PMT attached to the end. The SH has five columns, and each column as
1014 16 blocks with a PMT. The right HRS'(RHS) calorimeter system is constructed of
1015 the pion rejector 1(PR1) and the pion rejector 2(PR2). The two PRs on the RHS
1016 consist of 34 blocks arranged in two, 17 block columns.

1017 The calorimeters are used during the analysis process to help in PID. As high energy
1018 electrons pass through the dense leaded glass, the electron will lose its energy through
1019 bremsstrahlung radiation resulting in the emission of a photon. These photons begin
1020 a electromagnetic shower through the creation of positron-electron pairs. The shower
1021 of photons are detected by the PMTs attached to each block. The amount of energy
1022 contained in the scattered electron is directly proportional to the amount of photons
1023 generated during the shower.

1024 The signal from the calorimeters is recorded as an ADC. These ADC signals need
1025 to be calibrated similar to the cherenkov detector, subtracting the pedestal and
1026 determining the normalizing gain factor to match all PMT-ADC combinations. The
1027 total signal seen from the calorimeter can be seen in figure 3.22a. In order to use
1028 this ADC signal to help ID particles, the calorimeter needs an energy calibration.
1029 The calibration process uses a χ^2 minimization. Equation 3.5 demonstrates the

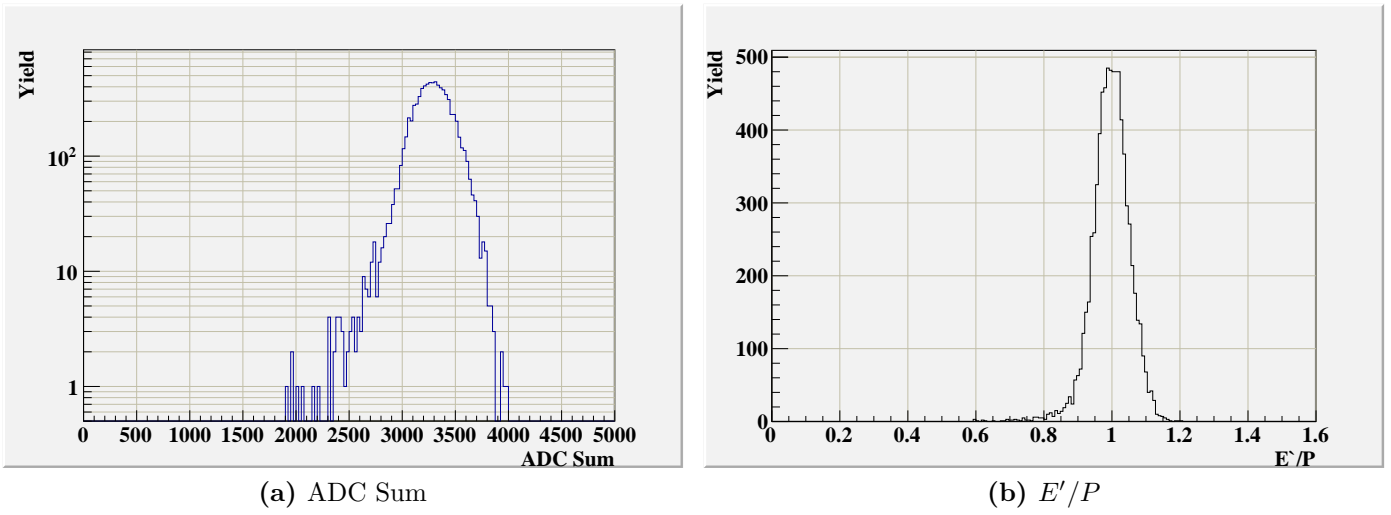


Figure 3.22: Left: The sum of all ADC channels from the LHRS calorimeters. Right: The total energy deposited into the LHRS calorimeter scaled by the momentum setting. Electron cuts have been applied.

minimization technique applied. In this equation, C_j is the calibration coefficient being determined for the calorimeter block j. Cal_{ij}^{ADC} is the ADC signal received from block j during event i, and p_i is the momentum of the electron being detected.

$$\frac{\partial \chi^2}{\partial C_i} = \sum_i^{Events} \left(\sum_j^{Blocks} C_j * Cal_{ij}^{ADC} - p_i \right)^2 = 0 \quad (3.5)$$

Using these calibration constants, the ADC signal in figure 3.22a can be turned in the calibrated data in the histogram show in figure 3.22b. This can be used to from PID selection cuts, removing any unwanted background events.

3.5 Trigger Setup

The MARATHON experiment designed three triggers to accept the most probable good electron events, while limiting the number of background events and preventing loss of efficiency due to electronic dead time. The design of these trigger are depicted in figure 3.23. Each trigger is build by the coincidence of signal between S0, S2 and

1041 the gas cherenkov. Trigger 1(T1) is the logical $\&$ between the S0 and S2. This is used
 1042 as a loose trigger to help test the detector timing and efficiencies. Trigger 2(T2) is the
 1043 main trigger used for good electron selection for the MARATHON experiment and
 1044 is by combining T1 and GC with a logical $\&$. The addition of the GC helps remove
 1045 many background pions and cosmic rays compared to T1. Trigger 3(T3), a logical \parallel
 1046 between s0 and S2 and $\&$ with the GC, was designed to help with the study of the
 1047 efficiency of T1 and T2. The RHRs uses the same triggers, T4 copy of T1, T5 copy
 1048 of T2, and T6 copy of T3.

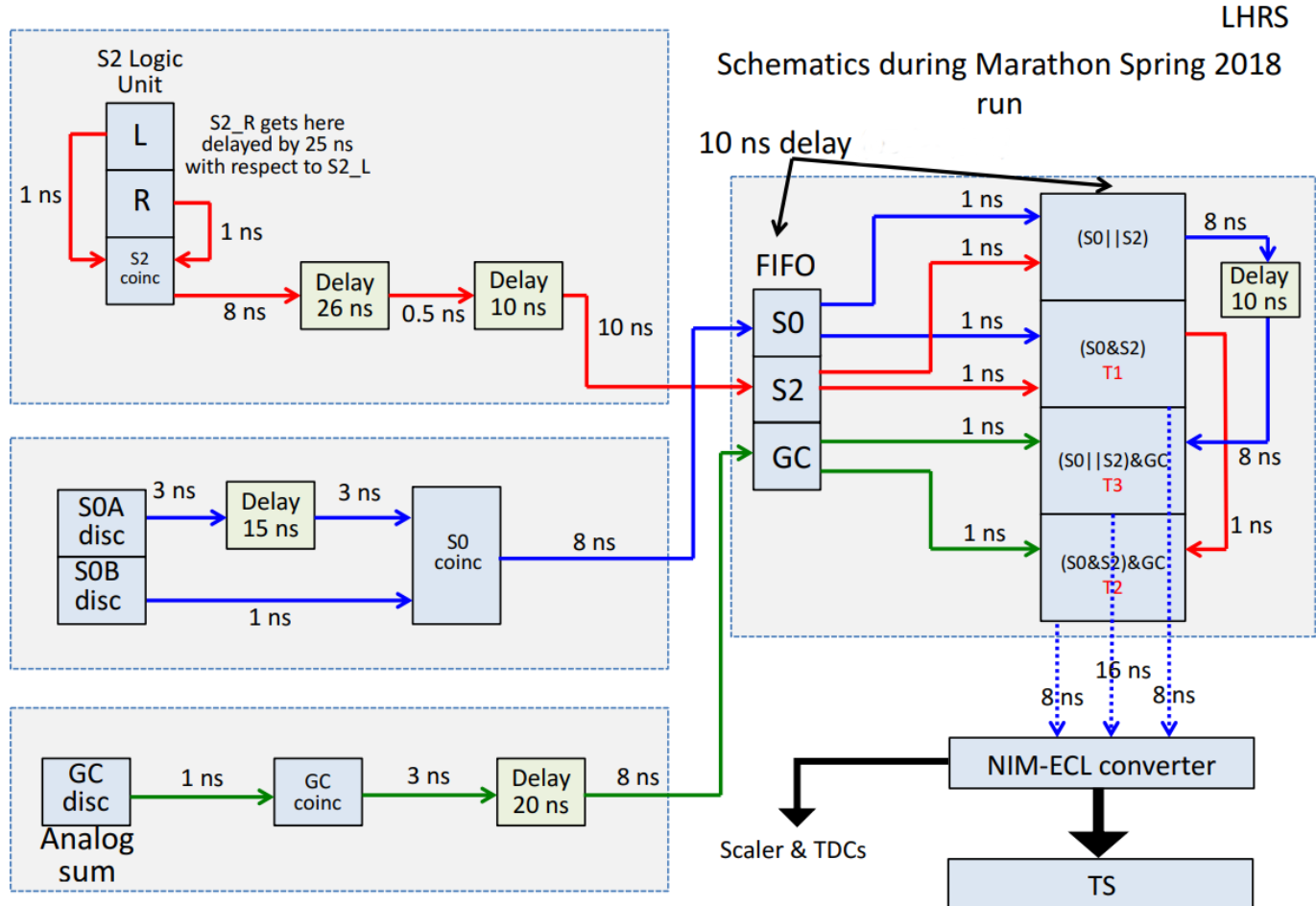


Figure 3.23: Scematic drawing of the trigger logic and timing for the MARATHON experiment [40].

1049 The trigger signal from S0 is the logical and between the signals of the two PMTS
1050 of S0. S0A has an additional time delay. This delay forces the leading edge of S0B
1051 to be the leading edge of the output of the S0 coincidence. The trigger signal for
1052 S2 is build by a coincidence in both the left and right PMT attached to each bar
1053 of the scintillator. The signal from the right pmt is used as the leading edge of the
1054 coincidence signal. S2 has many bars so the trigger source is formed by a coincidence
1055 in any of the S2 scintillator bars. The S2 trigger signal has an additional delay
1056 compared to the S0 trigger signal. This delay forces S2R to be the leading edge of
1057 all the logical & triggers The GC signal is formed by a sum of all the PMTs in the
1058 GC. If this sum meets some discriminator threshold, a trigger signal from the GC
1059 will be formed. The signals formed from the logic units for each of these trigger
1060 signals receive additional delays to prefect their timing in respect to each other. This
1061 tweaking of the timing spreads the trigger signals apart to help prevent the trigger
1062 signals from overlapping and allowing the recording of all possible triggers.

1063 **3.6 Kinematic Settings**

1064 The MARATHON experiment's goal is to study cross section ratios of ${}^3\text{H}$, ${}^3\text{He}$,
1065 ${}^2\text{D}$, and H. as a function of X . The MARATHON collaboration originally proposed
1066 to use the kinematics in table 3.1, allowing for the LHRs and RHRs to have mirror
1067 settings to expedite the rate of data collection at each position of X . The plan was
1068 to complete one kinematic setting and push the spectrometers out in angle from
1069 near 18 degrees at kinematic 1 to near 35 degrees at kinematic 16 while keeping the
1070 momentum settings of the spectrometers at 3.10 GeV for the 1st 15 settings, then
1071 decreasing the momentum to 2.9 for the last kinematic.

1072 Due to time and physical constraints caused by issues with the running of all
1073 four halls simultaneously, the kinematics where adjusted to provided the best chance
1074 of reaching the statical goals at a large range in X . The angle setting for each

Kin.	X_{Bj}	W2 GeV 2	Q2 GeV 2	E' GeV	Theta Degree	H2 est. hours	H3 est. hours	He3 est. hours	Total hours
1	0.23	12.30	3.41	3.10	18.19	0.28	0.45	0.28	1.02
2	0.27	11.70	4.00	3.10	19.73	0.42	0.69	0.43	1.54
3	0.31	11.11	4.60	3.10	21.15	0.62	1.03	0.62	2.27
4	0.35	10.52	5.19	3.10	22.49	0.90	1.50	0.89	3.29
5	0.39	9.92	5.78	3.10	23.76	1.29	2.17	1.27	4.73
6	0.43	9.33	6.37	3.10	24.97	1.85	3.13	1.81	6.79
7	0.47	8.74	6.97	3.10	26.12	2.66	4.52	2.57	9.75
8	0.51	8.14	7.56	3.10	27.23	3.80	6.53	3.66	13.99
9	0.55	7.55	8.15	3.10	28.30	5.52	9.56	5.27	20.36
10	0.59	6.96	8.75	3.10	29.34	5.12	14.19	7.70	30.01
11	0.63	6.37	9.34	3.10	30.34	12.12	21.39	11.41	44.92
12	0.67	5.77	9.93	3.10	31.31	18.56	33.08	17.35	68.99
13	0.71	5.18	10.53	3.10	32.26	29.08	52.35	26.98	108.41
14	0.75	4.59	11.12	3.10	33.18	47.19	85.80	43.47	176.46
15	0.79	3.99	11.71	3.10	34.08	87.73	150.03	74.76	306.51
16	0.83	3.40	12.30	3.10	34.96	155.36	287.74	141.21	584.30

Table 3.1: Kinematics originally planned for the MARATHON experiment including an estimation of time required for three of the gas targets in hours. Estimations provided by John Arrington and Zhihong Ye[46].

kin	X	W2	Q2	E'	theta	D2 count	He3 count	H3 count
1	0.22	11.89	3.07	3.1	17.58	94.0	93.0	124.3
2	0.26	11.33	3.62	3.1	19.11	109.0	103.0	120.5
3	0.3	10.76	4.19	3.1	20.58	121.0	78.0	101.1
4	0.34	10.2	4.76	3.1	21.93	78.0	64.0	69.8
5	0.38	9.63	5.32	3.1	23.21	25.0	39.0	39.3
7	0.46	8.51	6.45	3.1	25.59	40.0	40.0	41.2
9	0.54	7.38	7.57	3.1	27.78	36.0	36.0	35.5
11	0.62	6.2	8.76	3.1	29.92	29.0	27.0	27.6
13	0.7	5.13	9.82	3.1	31.73	23.0	23.0	23.0
15	0.78	4.0	10.96	3.1	33.56	21.0	23.0	22.8
16*	0.82	3.51	11.82	2.90	36.12	24.2	23.9	24.6

Table 3.2: Kinematic settings used during the MARATHON experiment. Kinematic 1-15 for LHRs, and kinematic 16 using RHRs. The good electron count is in units of thousands.

1075 kinematic were adjusted slightly. Most kinematics experience a slight degrees in
 1076 angle setting to increase the rate of electron counting. During the first few days of
 1077 running the MARATHON experiment the RHRS dipole experience a power supply
 1078 failure. This issue could not be resolved quickly. In order to complete our goal, the
 1079 MARATHON experiment adjusted the kinematic plan to remove RHRS from running.
 1080 The statical precision goal of the MARATHON experiment forced the collaboration to
 1081 remove a few kinematic points from the plan. The kinematics that the MARATHON
 1082 experiment were able to complete are listed in table 3.2. After the new plan was
 1083 solidified and data for the first few kinematics where complete, the RHRS was restored
 1084 to services. The RHRS was then set to kinematic 16 for rest of the experiment.

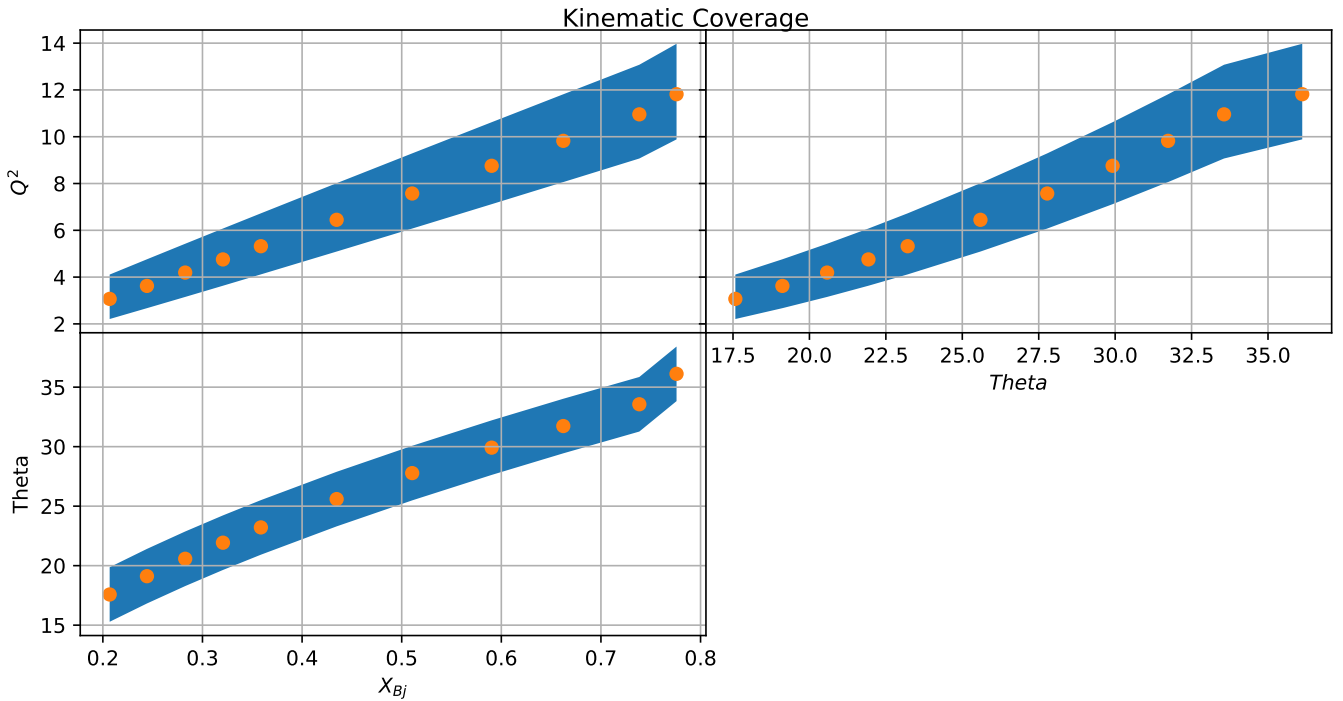


Figure 3.24: A kinematic coverage plot, demonstrating the Q^2 coverage for x and Theta. Also the relationship between x and Theta. The band around the points represents the approximate spectrometer acceptance in the y axis.

1085 **Chapter 4**

1086 **Data Analysis**

1087 The goal for the MARATHON experiment is to determine the EMC effect for
1088 the two A=3 systems ${}^3\text{He}$ and ${}^3\text{H}$, extract the F_2^n/F_2^p , and calculate the d/u quark
1089 distribution ratios. The goal of this analysis is to determine the EMC effect for
1090 the two A=3 systems via the ratio of measured cross sections. The cross-section
1091 of a scattering interaction is the probability of that event happening. In order to
1092 measure the probability of an event happening, a ratio has to be calculated between
1093 the magnitude of the number of those events versus the number of times that event
1094 could have happened. This analysis will use data from the HRSs, beam line detectors,
1095 and target information to measure the cross-section of ${}^3\text{He}$ and ${}^3\text{H}$ for kinematics of
1096 $0.2 < x < 0.82$.

1097 **4.1 Analysis Software**

1098 Hall A at JLab uses an analysis software (Analyzer) that is built on top of ROOT.
1099 The Analyzer is used to decode raw data received from TDCs, ADCs, and scalars
1100 into meaningful results. The decoding process uses raw data from the detectors in
1101 the HRSs and on the beam line to create an event. This event is assigned a track
1102 if applicable, and the events signal from the detectors are stored into a ROOT file.
1103 This ROOT file contains the raw and calibrated detector data from each signal, the

1104 track information, and physics variables calculated via the calibrated data and track
1105 information.

1106 4.1.1 Tracking

1107 The Analyzer uses calibrated VDC data to calculate the track of an event. The
1108 detector calibration was discussed in chapter 3. The event tracking is used to
1109 determine the scattered angle and momentum of the electrons detected. The track
1110 determined from the VDCs is in reference to the detector coordinate system. The
1111 Analyzer uses a optics matrix to relate the tracking information between all coordinate
1112 systems used in the Hall A analysis process. The coordinate systems will be briefly
1113 discussed in this section. A more complete guide with in-depth discussion of the
1114 coordinate systems is discussed in [1]. The coordinate system definitions and relations
1115 are obtained from [1, 51, 5].

- 1116 • **Hall Coordinate System(HCS):** The intersection of the electron beam and
1117 the vertical symmetry axis of the target system defines the origin of the HCS.
1118 This allows for \hat{z} to point along the beam line towards the beam dump and \hat{y}
1119 is up.
- 1120 • **Target Coordinate System (TCS):** The TCS is unique to the individual
1121 HRS. The \hat{z} axis of the TCS is defined by a line perpendicular to the surface
1122 of the spectrometers sieve slit aligned with the midpoint of the center hole. z_{tg}
1123 points away from the target towards the spectrometer. Nilange Liyange states
1124 in reference [51], "In the ideal case where the spectrometer is pointing directly
1125 at the hall center and the sieve slit is perfectly centered on the spectrometer,
1126 the z_{tg} axis passes through the hall center." Using the idea case, the origin of
1127 the TCS is defined by a set distance from the sieve surface. For the Left HRS,
1128 the TCS origin is 1.181m from the sieve, and for the Right HRS it is 1.178m.
1129 In the ideal case, the TCS origin is the HCS origin. Figure 4.1 shows the TCS
1130 with a an electron scattering event from a foil.

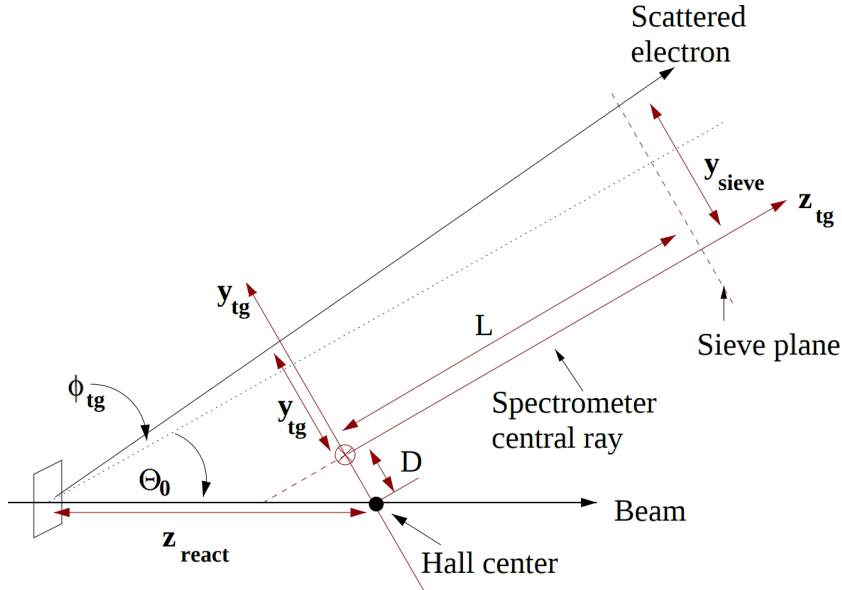


Figure 4.1: The TCS for an electron scattering event as seen from above. The event happens at z_{react} distance from the Hall center. \mathbf{L} is the distance from the Hall center to the sieve plane. \mathbf{D} is the horizontal displacement of the spectrometer axis from the ideal position. Θ is the spectrometer's central angle [51].

- 1131 • **Detector Coordinate System (DCS):** The origin of the DCS is at the
1132 intersection of wire 184 of the U1 and V1 planes of the first VDC. " \hat{y} is parallel to
1133 the short symmetry axis of the lower VDC [1]." \hat{z} is vertically up, perpendicular
1134 to the vdc planes. \hat{x} points away from the center of curvature of the dipole.
1135 The DCS values are calculated by using the intersection points of the 4 VDC
1136 planes and the spacial information of the VDC planes.
- 1137 • **Transport Coordinate System (TRCS) at the focal plane:** Rotating the
1138 DCS clockwise around its y-axis by 45° generates the TRCS. The TRCS can be
1139 expressed by DCS variables.
- 1140 • **Focal Plane Coordinate System (FCS):** The FCS is used to transport an
1141 event's track from the DCS to the TCS. The FCS is determined by rotating the
1142 DCS around its y-axis by the angle between the local central ray and the \hat{z} axis
1143 of the DCS. The local central ray is defined as a ray with $\theta = \phi = 0$ for the

1144 corresponding relative momentum $\frac{\Delta_p}{p}$ [51]. In the calculation of the FCS, the
 1145 offsets of the VDCs are used to correct any misalignments.

1146 The Analyzer provides two spatial coordinates and two angular coordinates for each
 1147 event. These coordinates are determined by data received via the VDCs and decoded
 1148 into the DCS. x_{det} and θ_{det} is the particle's position and tangent of the angle made by
 1149 its trajectory along the dispersive direction. y_{det} and ϕ_{det} is the particle position and
 1150 tangent of the angle perpendicular to the dispersive direction [51]. Using rotation
 1151 matrices and other transfer definitions these DCS coordinates are converted to the
 1152 FCS. The analyzer uses a calibration matrix to transport the FCS to the TCS. The
 1153 first order approximation of the matrix can be defined as:

$$\begin{bmatrix} \delta \\ \theta \\ y \\ \phi \end{bmatrix}_{tg} = \begin{bmatrix} \langle \delta | x \rangle & \langle \delta | \theta \rangle & 0 & 0 \\ \langle \theta | x \rangle & \langle \theta | \theta \rangle & 0 & 0 \\ 0 & 0 & \langle y | y \rangle & \langle y | \phi \rangle \\ 0 & 0 & \phi y | y \rangle & \langle \phi | \phi \rangle \end{bmatrix} \begin{bmatrix} x \\ \theta \\ y \\ \phi \end{bmatrix}_{fp}$$

1154 The relationship between the focal plane variables and the target coordinates our
 1155 conventionally can be expressed in a set tensors, defined as .

1156 4.2 Electron Counting

1157

1158 4.3 Efficiencies

1159 The high resolution spectrometers are capable of detecting a myriad of particles
 1160 that track through the detectors. The design of an experimental trigger uses the
 1161 properties of the individual detectors to capture data of meaningful events. Many
 1162 accidentals, background, and unwanted events trigger the data acquisition system,

Livetime for each kinematic

Kin	1	2	3	4	5	7	9	11	13	15
LiveTime	0.947	0.969	0.981	0.986	0.992	0.996	0.997	0.998	0.998	0.998

Table 4.1: Livetime during the MARATHON experiment calculated using trigger 2.

and some good electrons are missed by our DAQ. The removal of these unwanted events takes place during analysis via software cuts. Restricting the applicable signal from certain detectors through different cuts allows for the rejection of background particles and prevents contamination in the yield extraction.

4.3.1 Computer and electronic Lifetime

The signal from events that fire the DAQ travel through electronics like amplifiers and logic modules on its way to be recorded by the TDCs and ADCs. The processing of these signals require time at each stage. During that time another event will be discarded due to limitations in the hardware. This time when the DAQ system cannot handle another event is known as the dead-time of the system. Lifetime therefore is the percentage of time when an event can be recorded. The lost events need to be accounted for during the analysis process. The lifetime of the DAQ system for the MARATHON experiment was measured by determining the percentage of events that were recorded relative to the number of events that fired the corresponding trigger. The lifetime for the MARATHON experiment depended on the rate of events. The lifetime during the highest rate kinematic was determined to be 0.947, and climbs to 0.998 for the highest angle setting. Listed in table 4.1 are the calculated values for lifetime at each kinematic.

4.3.2 Particle Identification Efficiency

One of the largest sources of contamination for the MARATHON experiment are negatively charged pions. These pions are removed through software cuts made in the total signal from the ten cherenkov PMTs(photomultiplier tubes) and the energy

Cherenkov sum versus Total Energy deposited

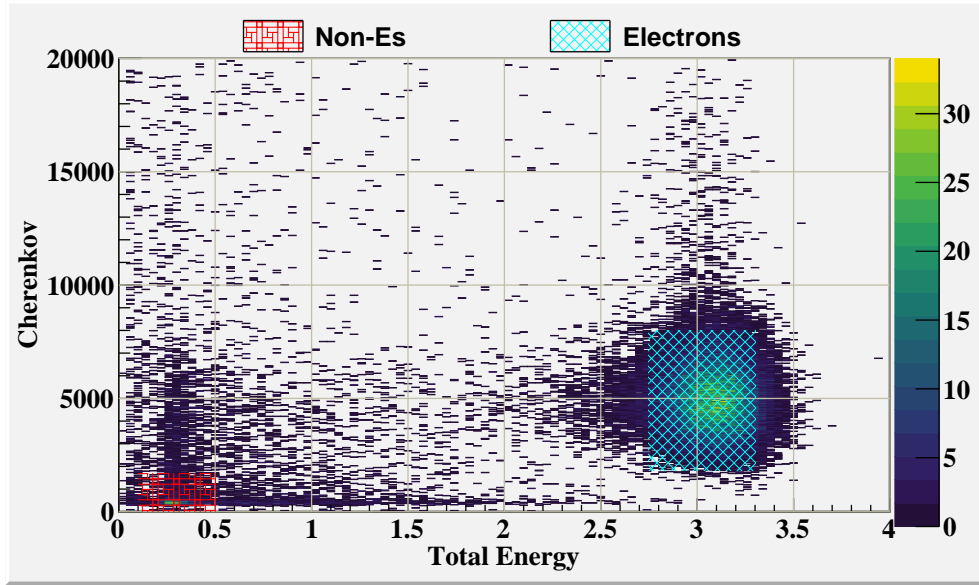


Figure 4.2: Two dimensional plot of the cherenkov sum versus Total Energy deposited, including electron sampling in teal and non-electron sampling in red.

1185 deposited into the blocks of both layers of the calorimeter. Electrons can be identified
 1186 by their behavior in the spectrometer. High-quality electrons will track through
 1187 the entire detector stack to deposit most of their energy into the total calorimeter
 1188 system and creating a large amount of light in the cherenkov. Though this knowledge
 1189 tight cuts can be used to study the efficiency of the particle identification system.
 1190 Plotting the signal in the cherenkov versus the energy deposited into both layers of
 1191 the calorimeter allows for visual representation of the sampling cuts made in the
 1192 efficiency studies, which can be seen in figure 4.2.

GE_{sample} = Known electron sample from tight cut

$$GE_{pass} = GE_{sample} \text{ and pass identification cut} \quad (4.1)$$

$$Electron_{eff} = \frac{GE_{pass}}{GE_{sample}}$$

1193

Particle ID and efficiency sampling for PID detectors

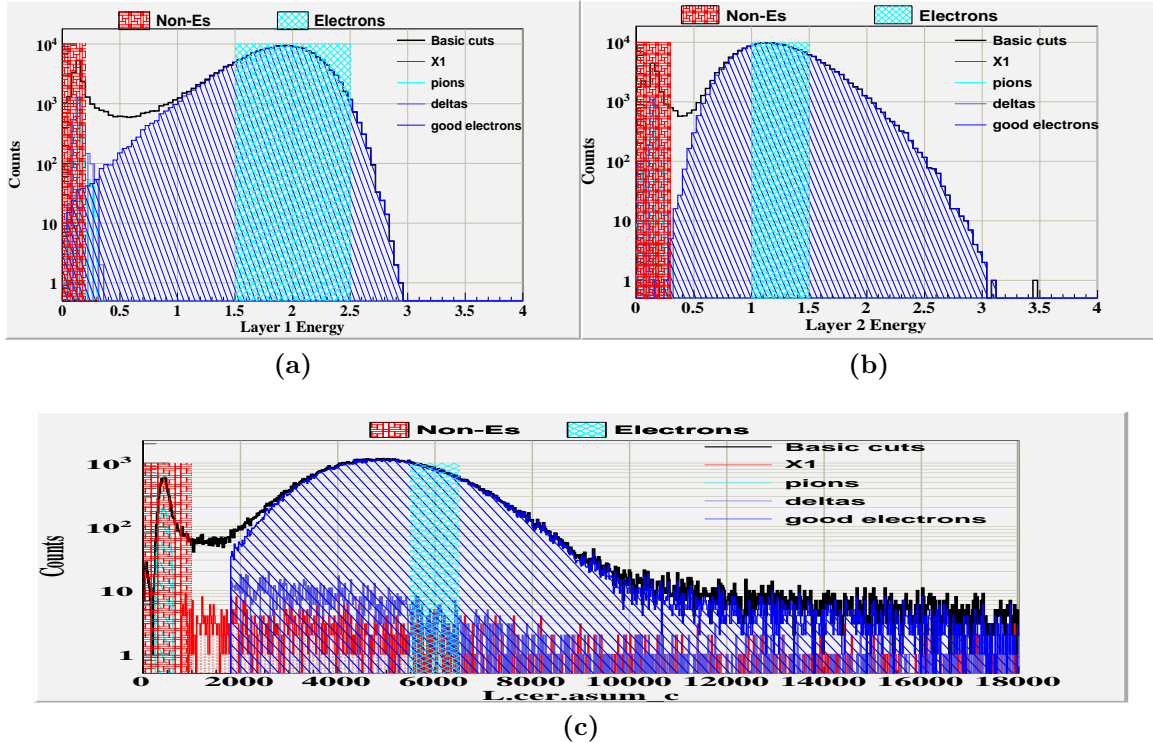


Figure 4.3: Electrons and other back ground particles identified via cuts in the total calorimeter and the gas cherenkov shown in the individual layers of the calorimeters and the cherenkov. Sampling cuts for Electrons in teal and Non-Electrons in red.

1194 The efficiencies of the spectrometer's particle identification(PID) detectors were
 1195 determined by using the first calorimeter layer, the second calorimeter layer, and the
 1196 cherenkov to provide samples of good electrons and other particles. The PID efficiency
 1197 of the individual detectors was determined using equation 4.1. The good electron
 1198 sample for calculating the efficiency of the single detector was defined by sampling
 1199 through the other two detectors. Sampling through the two layers of the calorimeter is
 1200 shown in figure 4.3a for the first layer of the calorimeter and 4.3b for the second layer.
 1201 The cherenkov good electron sample is shown in figure 4.3c. The electron sample
 1202 from the cherenkov is contaminated by delta particles and a combination of unknown
 1203 particles. These unidentified background particles are known to be relativistic due to
 1204 the amount of light seen in the cherenkov. However, the events do not deposit enough

energy into the calorimeter system to be considered as a good electron that scatter from our target through the detector. Using sampling in one layer of the calorimeter and the cherenkov, these unwanted low energy particles are rejected from sampling for efficiency calculations. The electron selection PID efficiency for the three PID detectors was determine at each kinematic setting to be approximately 98% . The efficiency was determined to be independent of the kinematic setting. Only small fluctuations were seen during the study, these small changes are due to decrease in statics, and all of the results fall within statiscal uncertainty of being independent of kinematic setting. The non-electron suppression efficiency was determine as part of this PID efficiency study to ascertain how many back ground particles leak into our sample of good electrons after cuts our made. The suppression efficiency of the cherenkov suffered due to the contamination of the relativistic low energy particles. Combining the two calorimeter detectors with the cherenkov increased the overall suppression efficiency for the spectrometer to 99.9% over the entire kinematic range of the MARATHON experiment.

4.3.3 Trigger Efficiency

The process of capturing data from the two HRSs begins with the firing of a trigger. The trigger design for MARATHON focused on triggering for electrons and reducing the amount of other particles. Figure 3.23 describes the design of MARATHON’s main trigger and efficiency triggers. MARATHON’s main trigger, trigger 2, consist of a ($So \& S2$) $\& Cer$. Due to inefficiencies of the electronics, logic, and detectors an event can produce a false trigger or a high quality electron may not fire the main trigger.

A low threshold in the cherenkov allows for an inclusive trigger limiting the overall number of quality electrons missed, but allows for a large quantity of false triggers. Software PID cuts prevent the contamination of false positives from trigger inefficiencies. The tight PID software cuts removes the false positive inefficiency

PID efficiency for each detector for all kinematics.

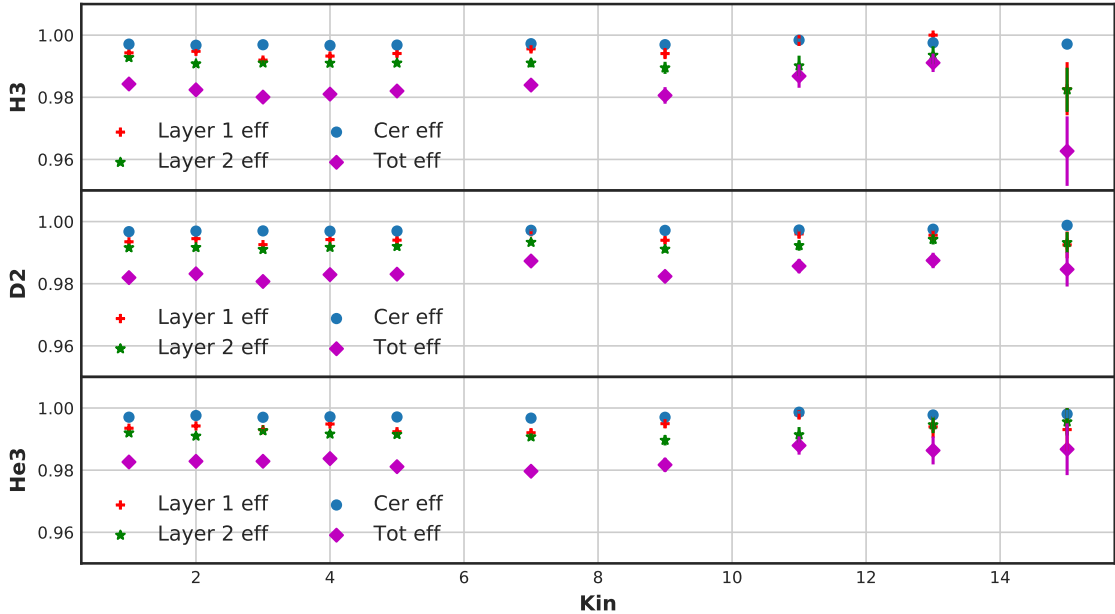


Figure 4.4: The PID efficiency for the cherenkov and both layers of the calorimeter,including the overall total PID efficiency for each of the gas targets at all of the kinematics.

Trigger efficiency for the MARATHON experiment

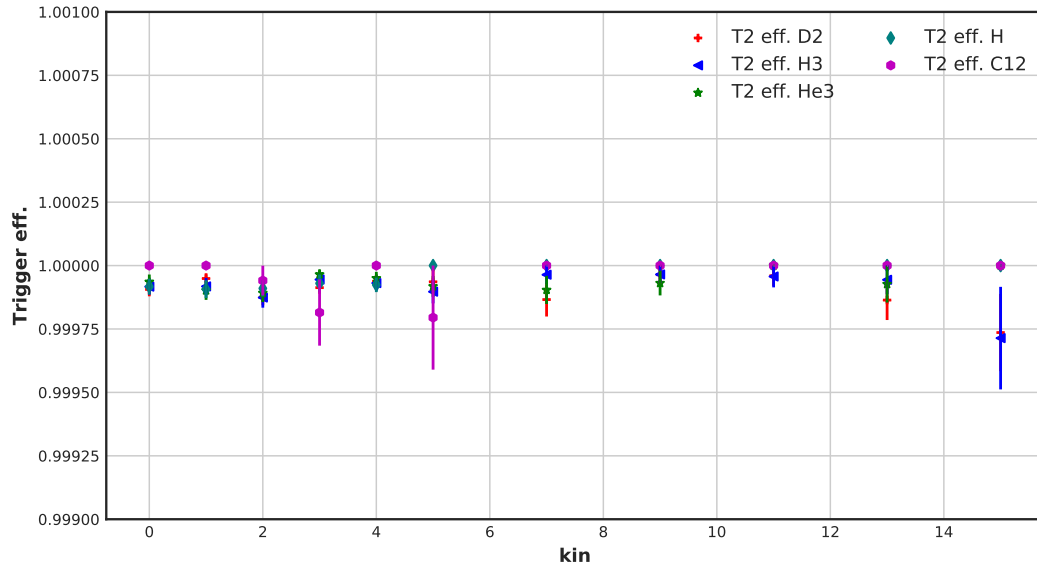


Figure 4.5: Trigger efficiency of trigger 2 for different targets at all kinematics calculated via sampling from trigger 1.

Tracking efficiency for the MARATHON experiment

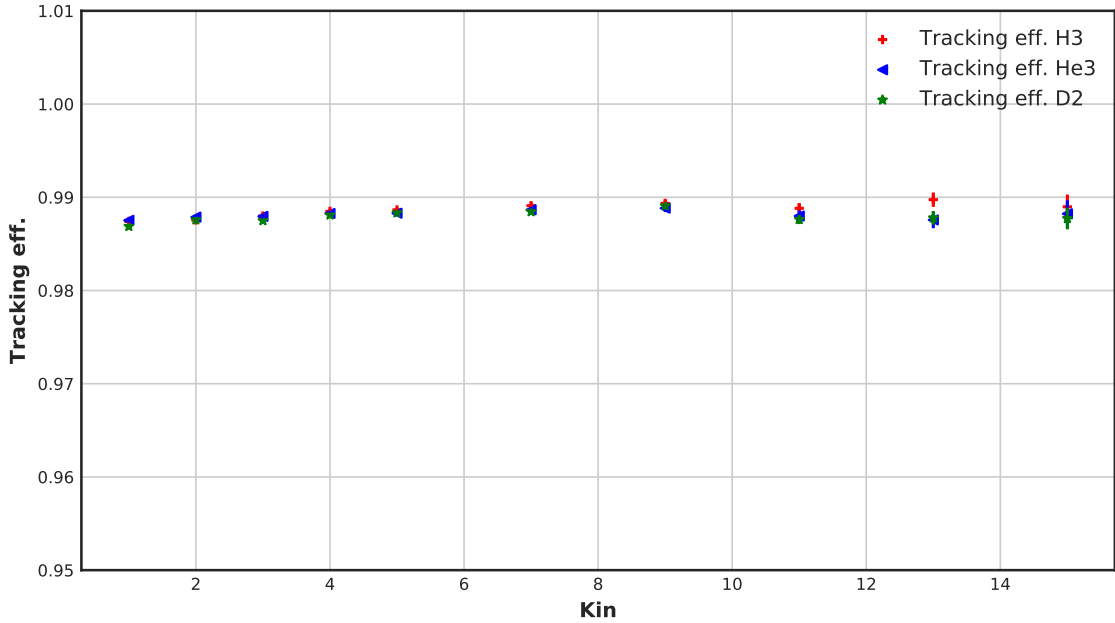


Figure 4.6: Tracking efficiency of the VDCs for different targets at all kinematics.

from the trigger design and is then considered in the PID efficiencies. The trigger inefficiency caused by missed high quality electrons was then calculated by sampling the high quality electrons in trigger 1, ($S_o \& S_2$). This ties the efficiency of trigger 2 with the performance of the scintillators. The efficiency of the two scintillating planes in conjunction is calculated by using sampling in trigger 3, ($S_o | S_2$) & Cer with strict PID cuts in both layers of the calorimeters and requiring a hit in the cherenkov. The two scintillator planes in conjunction have an efficiency greater than 99.7% for all kinematics. Combining the trigger efficiency of the main trigger shown in figure 4.5 with the performance of the scintillators give an over all efficiency for the trigger of the MARATHON experiment of greater then 99.6%.

4.3.4 Tracking Efficiency

Particles that travel through our detector could originated from sources wanted or unwanted. In order to control the source of the scatter electrons, we use a particle's

1245 track to identify its source. The signals received via the VDC is used to produce
1246 a particles track from the target to end of the spectrometer. The largest source of
1247 inefficiency for the VDCs are incorrectly identified tracks. High quality electrons
1248 that transverse the spectrometer should only have one good track, calculated via the
1249 tracking package in the analysis software. The capability of the VDCs to determine a
1250 good electron event's one good track is known as the one track efficiency for the VDCs.
1251 Quantitatively the one track efficiency (ϵ_{VDC}) can be obtained via:

$$\epsilon_{VDC} \equiv \frac{N_{1track}}{N_{all}} \quad (4.2)$$

1252 Where the number of good electron events that have one good track is defined as
1253 N_{1track} , and N_{all} are all of the electrons rather they have a good track or not. The
1254 good electron selection is made via PID cuts in the calorimeter and cherenkov, and
1255 cuts in the ADC and TDC of the scintillators. Direct cuts in the signal of the
1256 scintillators were made to include the nominal acceptance cuts, which were produced
1257 through tracking software. The tracking efficiency of HRSs during the MARATHON
1258 experiment is shown in figure 4.6 for the three gas targets during all kinematic ranges.
1259 The efficiency of the VDCs is not relative to the angle of the spectrometer. So the
1260 uniform tracking efficiency across all kinematics is expected and helps eliminate any
1261 concerns of the performance of the VDCs during the experiment.

1262 4.4 Background Subtraction

1263 The purpose of this analysis is to study the DIS cross sections of deuterium, helium-
1264 3, and tritium. The sample of scattered events used to determine the cross section
1265 of a given nuclear target then needs to be cleaned of any contamination produced
1266 from other targets and processes. The electrons detected by the spectrometers can
1267 be electrons that scattered from our chosen target, scattered from a source other
1268 than our target, or produced through process other than DIS scattering. The two

1269 sources of contamination for the MARATHON experiment are events scattered from
1270 the aluminum end caps of the target cell and pair produced electrons via photon
1271 interaction.

1272 4.4.1 End Caps

1273 The target cells used during the MARATHON experiment are shown in figure
1274 3.12. The majority of the events from the end caps can be removed easily via a cut
1275 in the reconstructed quantity of reaction vertex along the beam axis. The relatively
1276 large density thickness of the aluminum end caps cause a large amount of end cap
1277 contamination. The majority of the electrons that scatter from the end caps can be
1278 removed through software cuts in the reaction vertex along the beam axis(z). Show
1279 in figure 4.7 is a comparison of the reaction vertex of the electron events between the
1280 gaseous targets and the empty cell target at kinematic 4. The yield is normalized by
1281 the number of event in the histogram to remove any bias from the amount of time
1282 of beam on target. The empty target results in figure 4.7, demonstrate the form of
1283 scattering off of the aluminum windows of our target cell. Using the reconstructed
1284 vertex location of the scattering origin, the vast majority of the events from the
1285 windows can be removed. This vertex cut is shown by the two vertical blue lines.
1286 Only events that lie within these two line are considered good electrons from our
1287 chosen target.

The empty cell vertex z disruption does have content within the vertex cut. These events that remain after the cut are corrected for via an end cap contamination factor. This factor is calculated by determining the ratio of the number of good electrons that scatter from the empty cell and from each gas cells, resulting in ratio of $(\frac{Yield_{EC}}{(Yield_{Gas}+Yield_{EC})})$. Where the subscript EC denotes events from the end caps.

Scattering vertex along the beam axis.

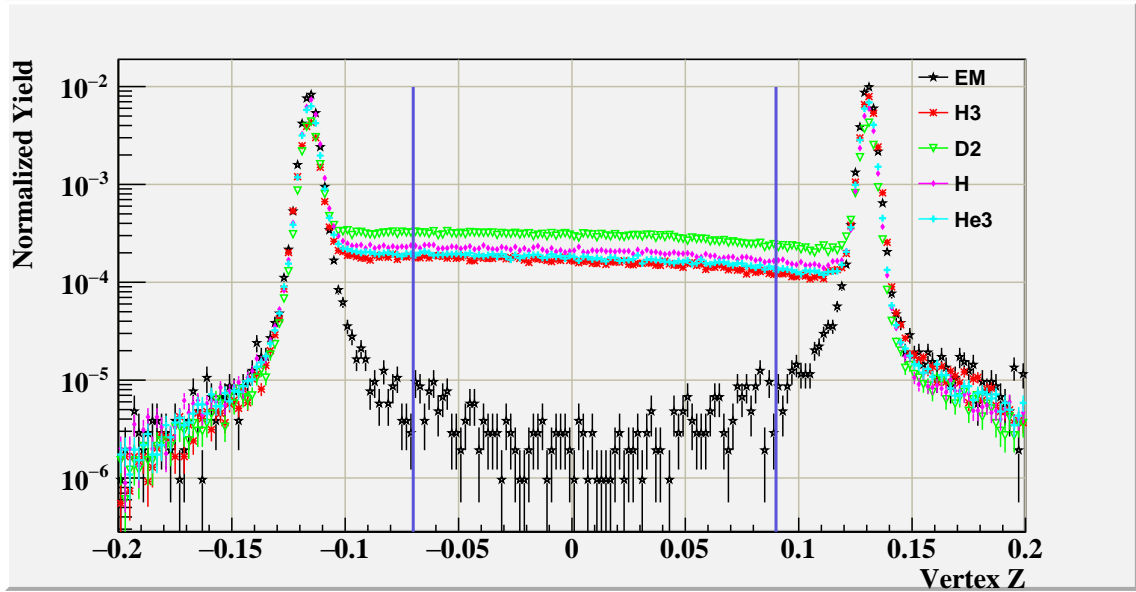


Figure 4.7: Comparison of the scattering vertex along the z axis for the empty target(EM) and the gas targets at kin. 4.

The correction factor applied to the yield calculation is defined as:

$$ECC = 1 - \left(\frac{Yield_{EC}}{(Yield_{Gas} + Yield_{EC})} \right) \equiv \frac{Yield_{gas}}{(Yield_{Gas} + Yield_{EC})}$$

1288 4.4.2 Pair Produced Electrons

1289 The high energy scattering interaction used to create deep inelastic scattering events
 1290 can produce high energy photons and pions. The high energy photons that have
 1291 energy greater than 1.022 MeV can convert into e^+e^- pairs when the photons interact
 1292 with a medium. A correction for the number of back ground electrons produced via
 1293 a pair production process was calculated by determining the amount of positrons
 1294 produced from equal targets and kinematics. The yield of positrons were measured
 1295 for kinematics one through five. The results were used to construct a function to
 1296 determine the amount of contamination at high x_{Bj} kinematics. Figure 4.8 shows the
 1297 amount of positron contamination for tritium and an exponential fit to extrapolate
 1298 over the entire ranged in x_{Bj} for the MARATHON experiment.

Tritium positron contamination.

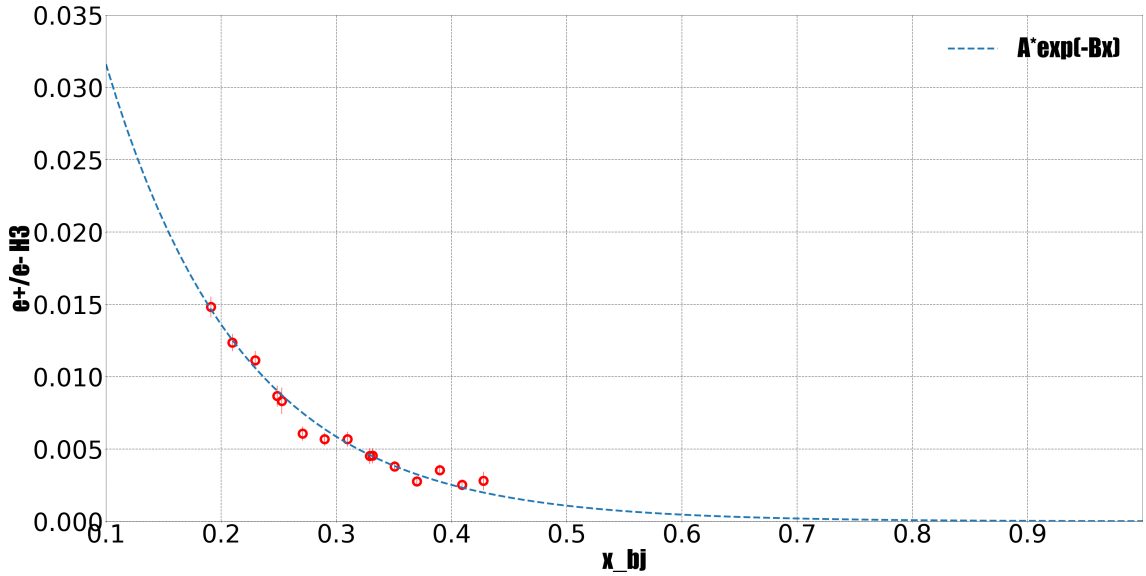


Figure 4.8: The ratio of positron events to electrons for tritium [68].

¹²⁹⁹ 4.4.3 Beta Decay of Tritium

Tritium a radioactive isotope of hydrogen will beta decay to ${}^3\text{He}$. Tritium has a half-life of 4500 ± 8 days [52]. The gas cell used to contain Tritium for the experiment was filled on October 23, 2017. The initial tritium thickness density of our tritium cell was 0.077 ± 0.001 grams per cm^2 . Tritium will decay to ${}^3\text{He}$ via a beta interaction. The tritium in our cell is diatomic and decays via two channels[70]. The possible decay channels and their branching probabilities are shown in equation 4.3. In DIS interactions, the molecular effects are ignored due to the size of the probe in a DIS scattering event which allows for the different channels to be treated as one.



The amount of ${}^3\text{H}$ and ${}^3\text{He}$ in our tritium cell will change in respect to the time since the filling of the cell. Equations 4.4 and 4.5 describe the amount of ${}^3\text{H}$ and ${}^3\text{He}$ in the tritium cell has a function of the time since fill date and the original amount of

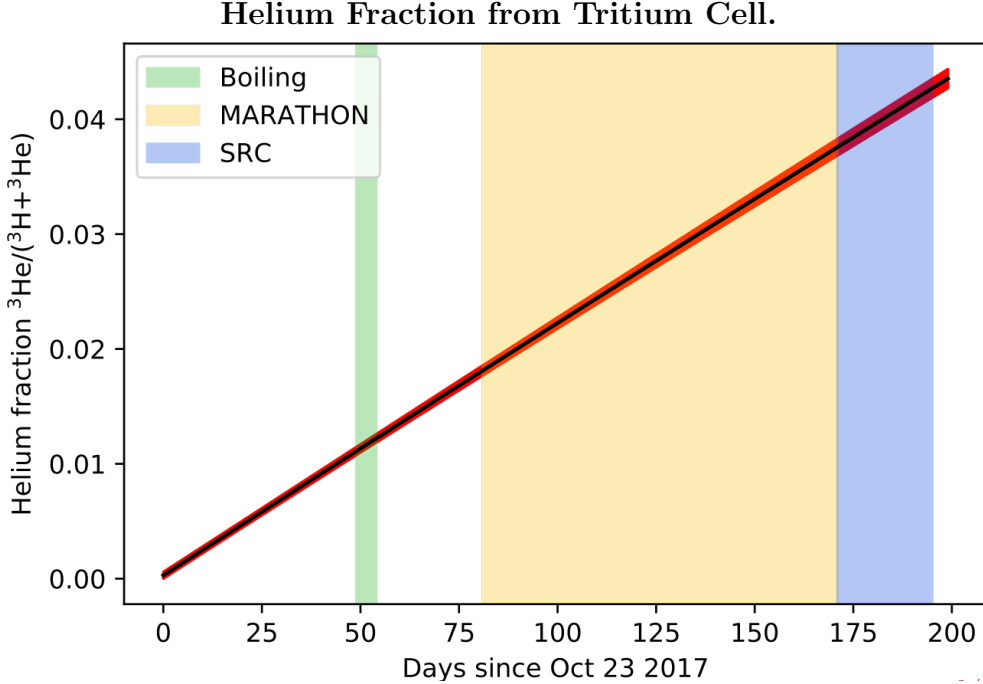


Figure 4.9: The amount of Helium in the Tritium cell in reference to the total amount of material in the cell as a function of time. Included are bands of time for different sections of the Tritium run group's plan [49].

${}^3\text{H}$ and ${}^3\text{He}$ in cell at filling. In equations 4.4 and 4.5, $n_T(n_H)$ is the time dependent amount of tritium(helium), and $n_T^0(n_H^0)$ is the amount of tritium(helium) in the cell at time of filling. t is the time since the cell was filled and τ is the mean lifetime of tritium.

$$n_T = n_T^0 e^{-t/\tau} \quad (4.4)$$

$$n_H = n_H^0 (1 - e^{-t/\tau}), \quad (4.5)$$

1300 As time passes the amount of ${}^3\text{He}$ increases, the contamination becomes a non-
 1301 negligible effect on the yield of scattered electrons. The fraction of ${}^3\text{He}$ in the tritium
 1302 can reach up to 3% for the data from the end of the MARATHON experiment. This
 1303 ${}^3\text{He}$ fraction as a function of time is shown in figure 4.9, with the period for running
 1304 the MARATHON experiment labeled as a color band.

$$Y = \frac{\sum N_i}{\sum Q_i n_i}, \quad (4.6)$$

$$Y_{raw} = \frac{\sum(T_i + H_i)}{\sum Q_i(n_{T,i} + n_{H,i})} \quad (4.7)$$

$$\langle f_H \rangle \equiv \frac{\sum Q_i f_{H,i}}{\sum Q_i} \quad (4.8)$$

1305 The events that scatted from Helium in our tritium cell need to be subtracted
 1306 from the measured yield to supply an accurate count. The yield from any target is
 1307 defined as the number of electrons per charge weighted scattering centers. The yield is
 1308 shown in equation 4.6 and defined as the number of counted events(N_i) per possible
 1309 scattering changes, or charge(Q_i) times number of scattering centers (n_i). Data is
 1310 recorded in many runs, so a sum over runs(i) is required to get the total yield. The
 1311 subtraction factor is calculated by breaking down the yield from the tritium cell as the
 1312 addition of the yield from tritium (Y_T)= $\Sigma(T_i/Q_i n_i)$ and helium (Y_H)= $\Sigma(H_i/Q_i n_i)$
 1313 in the tritium cell as shown in equation 4.7. The correction for the beta decay is
 1314 defined in equation 4.9. It can be determined by expanding equation 4.7 out and
 1315 solving for the tritium yield from the tritium cell. Where $\langle f_H \rangle$ is the charge weighted
 1316 helium fraction defined in equation 4.8 [45]. The helium fraction $f_{H,i}$ is the ratio of
 1317 helium scattering centers in the tritium cell to total number of scattering centers.
 1318

$$Y_T = Y_{raw} \left(\frac{1}{1 - \langle f_H \rangle} \right) - Y_H \left(\frac{\langle f_H \rangle}{1 - \langle f_H \rangle} \right) \quad (4.9)$$

1320 4.5 Luminosity

1321 4.6 Monte Carlo Ratio Method

1322 Use ECs slides need cite ,explain how to get CS from data/MC

₁₃₂₃ **4.6.1 Monte Carlo Simulation**

₁₃₂₄ gen - table -weight

₁₃₂₅ **4.6.2 Monte Carlo Comparison**

₁₃₂₆ acc - comp

₁₃₂₇ **4.7 DIS Cross Section**

₁₃₂₈ **4.8 Systematic Error**

₁₃₂₉ **Chapter 5**

₁₃₃₀ **Results**

₁₃₃₁ **5.1 EMC Ratios**

₁₃₃₂ **5.1.1 Isoscalar Correction**

₁₃₃₃ **5.1.2 EMC Effect**

₁₃₃₄ **Chapter 6**

₁₃₃₅ **EMC Simulation**

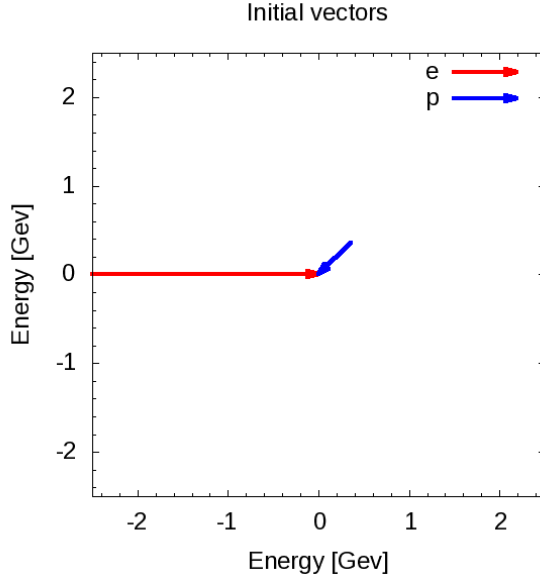
₁₃₃₆ Nuclei are systems of nucleons that interact strongly. The characteristic scale for the
₁₃₃₇ nucleons momentum is approximately the Fermi momentum, $k_F \approx 200 - 270 \text{ MeV}/c$
₁₃₃₈ [35]. However because of the strongly repulsive nature of the nucleon-nucleon
₁₃₃₉ interaction at short distances prevents two nucleons from laying in close proximately
₁₃₄₀ to each other. This strong interaction demands the presence of high-momentum
₁₃₄₁ components in the nuclear ground state wave function. A simulation was designed
₁₃₄₂ to phenomenologically study the effect of these high-momentum components on the
₁₃₄₃ nuclear EMC effect. This program was designed in two phases. The first phase used
₁₃₄₄ simple elastic scattering and a single value for the targets momentum to investigate
₁₃₄₅ overall effect of different target momentum on the yield in bins of x_B . The second
₁₃₄₆ phase of the simulation was created to lay out the effect of using different momentum
₁₃₄₇ distributions on the yield for the EMC effect region of x_B , 0.3 to 0.7.

₁₃₄₈ **6.1 Investigation**

₁₃₄₉ This simulation phenomenologically investigates the effect of a moving target on the
₁₃₅₀ EMC effect by scattering a beam of electrons off of a moving proton. The target
₁₃₅₁ protons are comprised of a directional vector of 0° to 360° in respect to the incoming
₁₃₅₂ electron beam and a momentum between 0 and 1 GeV/c. Figure 6.1 contains a

1353 possible event for the simulation. The electron approaches with 2.5 GeV of energy
1354 and collides with a proton moving with a momentum of 0.5 GeV/c with an angle of
45° in respect to the electron trajectory.

Figure 6.1: Example of the electron beam(red) with a energy of 2.5 GeV and the proton(blue) with angle of 45° in respect to the electron and with a momentum of 0.5 GeV/c.



1355
1356 Using conservation of momentum and conservation of energy in elastic collisions,
1357 this simulation calculates the final state of the electron and proton after the scattering
1358 event by randomly selecting a scattered direction for the electron. The vector
1359 representation of the scattered products are shown in figure 6.3a. In order to
1360 make these calculations systematic and to study cross sections models the simulation
1361 transform each event into the rest frame of the target before scattering.

1362 6.2 Transformation

1363 The Simulation completes a set of Lorentz invariant rotations and boost for each
1364 event to transform the lab frame of the electron and proton collision into the rest
1365 frame of the proton. First the simulation takes the initial proton and electron vectors

1366 and rotates them to align the proton vector to the horizontal axis, shown in figure
 1367 6.2b. This rotation uses the angle between the proton and the electron defined as λ .
 1368 This allows for a straight forward calculations for the Lorentz factors β and γ and
 1369 to boost into the rest frame of the target proton, figure 6.2c. Once in the boosted
 1370 frame, the angle between the electron and the horizontal axis is defined as δ . Right
 1371 before the simulation starts to calculate the scattered products, it completes one more
 1372 rotation to align the electron vector with the horizontal axis, figure 6.2d, to make the
 1373 scattering calculation systematic and unconditional.

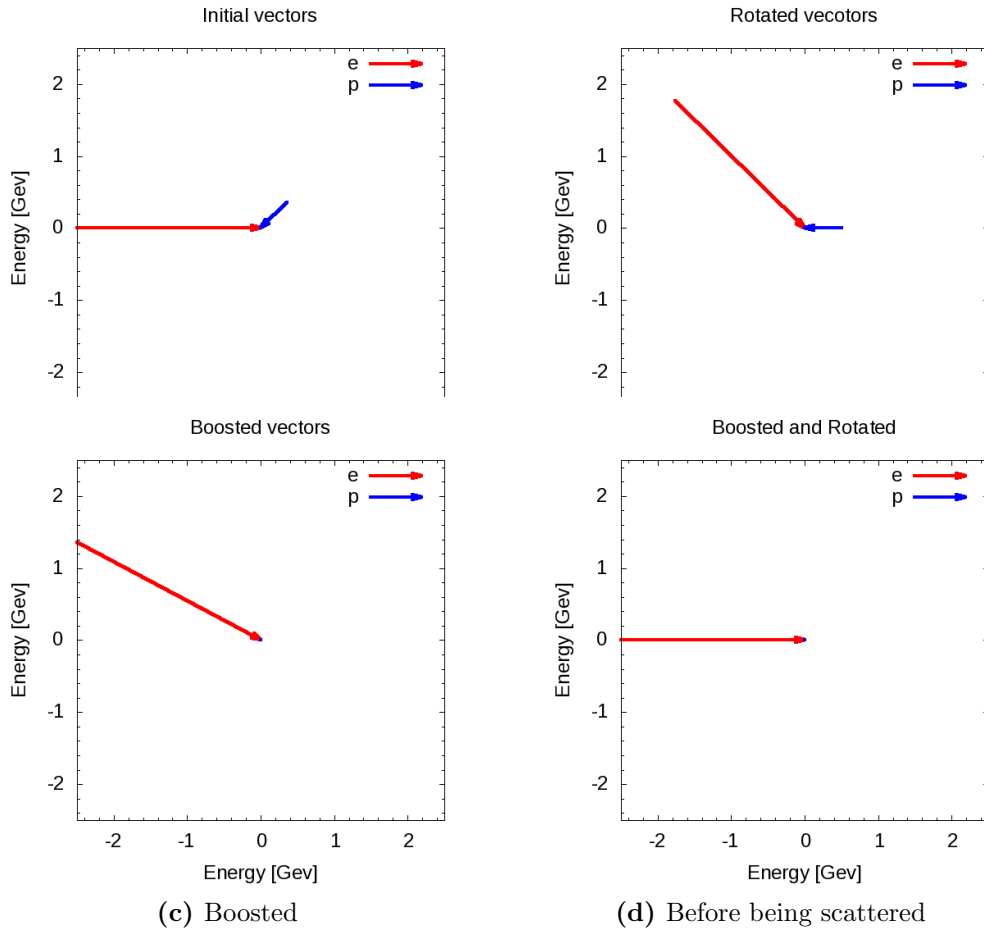


Figure 6.2: Vector representations of the momentum for the incoming electron(red) and target proton(blue) with units of GeV for each phase of their transformations before scattering.

1374 In order to gain a more complete understanding of the scattering products, the
1375 program completes a set of transformations to move from the rest frame of the target
1376 proton to the beginning lab frame. After the simulation calculates the scattered
1377 products it begins to transform back by beginning with a rotation by the angle δ ,
1378 figure 6.3b. Followed by the inverse of the previously used Lorentz boost. The
1379 last transformation, a rotation by λ , transforms the frame back into the lab frame.
1380 A proton vector and electron vector in the lab frame are the final products of the
1381 simulation. An image of the electron and proton vectors for each transformation can
1382 be found in figure 6.3. These vectors allow for calculation of kinematic variables such
1383 as Bjorken x and the four-momentum transfer (Q^2). This simulation will complete
1384 these steps for many electron and proton combinations.

1385 6.3 Results

1386 This electron scattering simulation produced results for two stages. The firsts stage
1387 used a fix proton momentum for each run to compare the yield in bins of x_B . Figure
1388 6.4 shows the results for three different runs, each having a unique fixed proton
1389 momentum. The red histogram represents a run with a proton momentum of 0 Gev/c.
1390 The result is an elastic peak at x_B of one. The blue histogram contains the results
1391 having a fixed proton momentum of 0.25 GeV/c. Increasing the initial momentum
1392 of the proton spreads the events into two peaks. The scattering interactions that
1393 form the peak above 1 x_B are produced by events were the proton's initial directional
1394 vector are orientated towards the electron. The events that produce an x_B below
1395 1 have a proton direction pointing away from the electron initially. Doubling the
1396 proton's initial momentum from 0.25 GeV to 0.50 GeV causes these peaks two spread
1397 out furtherer in x_B .

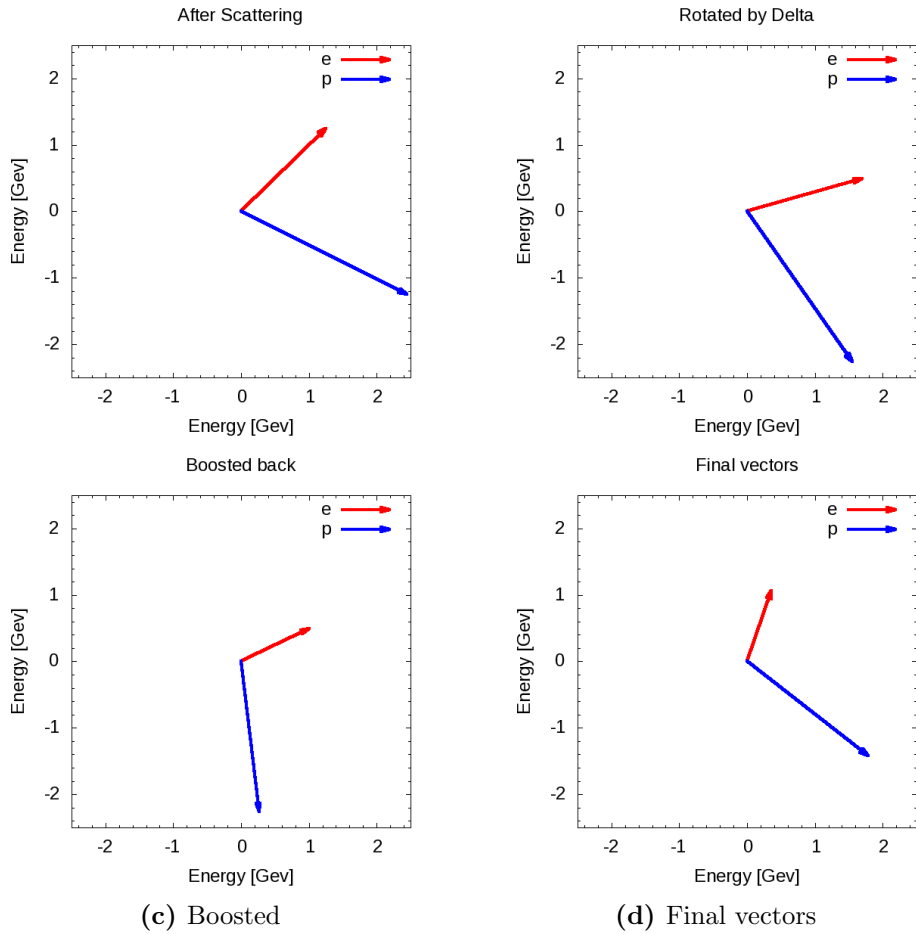
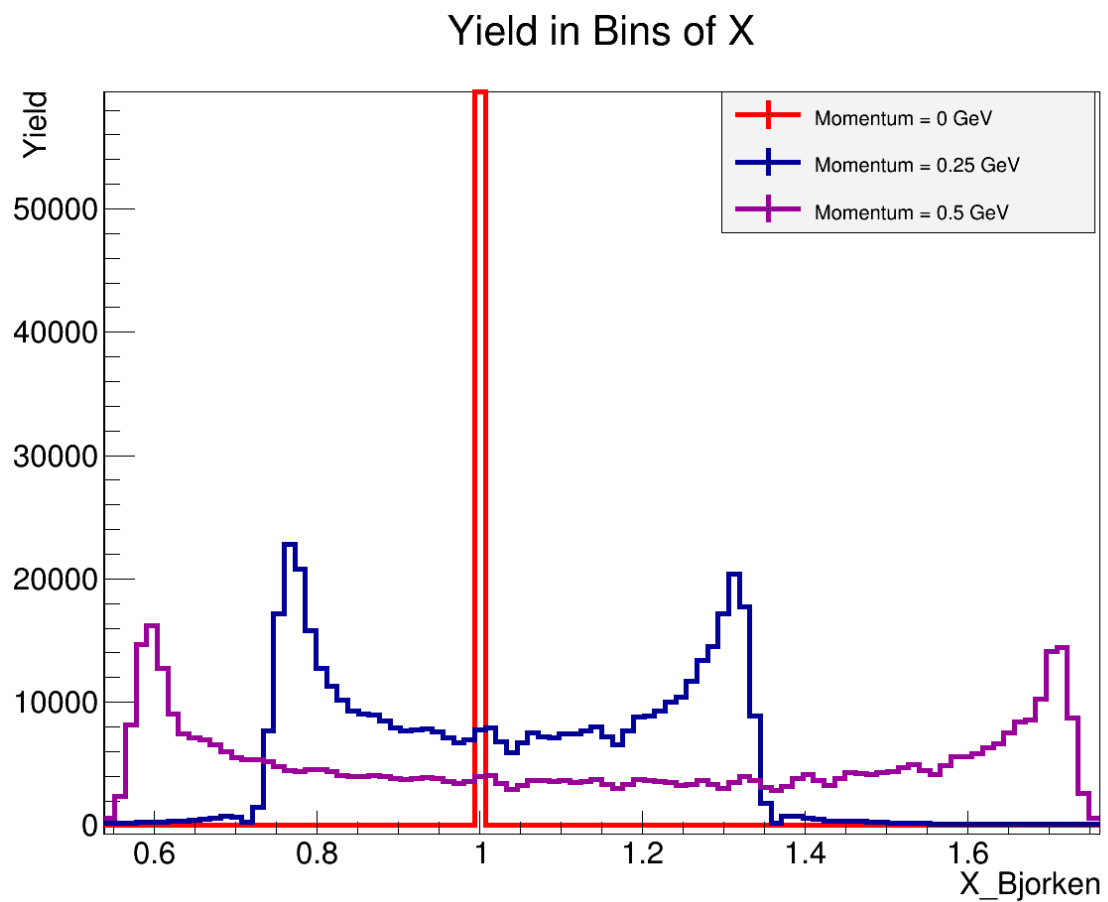


Figure 6.3: Vector representations of the momentum for the incoming electron(red) and target proton(blue) with units of GeV for each phase of their transformations after scattering).

Figure 6.4: Simulation results for fixed momentum protons. Three runs with unique proton momentum.



₁₃₉₈ Chapter 7

₁₃₉₉ Conclusion

Bibliography

₁₄₀₁ **Bibliography**

- ₁₄₀₂ [1] *ESPACE Manual, Event Scanning Program for Hall A Collaboration Experiments.* [60](#), [61](#)
- ₁₄₀₃
- ₁₄₀₄ [2] *Proceedings: International Symposium on Electron and Photon Interactions at High Energies, 3rd, Slac, 1967*, 1967. [vii](#), [6](#)
- ₁₄₀₅
- ₁₄₀₆ [3] A. Airapetian et al. Measurement of $R = \sigma(L) / \sigma(T)$ in deep inelastic scattering on nuclei. 2002. [23](#)
- ₁₄₀₇
- ₁₄₀₈ [4] S. V. Akulinichev, S. Shlomo, S. A. Kulagin, and G. M. Vagradov. Lepton-nucleus deep-inelastic scattering. *Phys. Rev. Lett.*, 55:2239–2241, Nov 1985. [26](#)
- ₁₄₀₉
- ₁₄₁₀ [5] J. Alcorn et al. Basic Instrumentation for Hall A at Jefferson Lab. *Nucl. Instrum. Meth.*, A522:294–346, 2004. [viii](#), [31](#), [33](#), [34](#), [44](#), [45](#), [60](#)
- ₁₄₁₁
- ₁₄₁₂ [6] P. Amaudruz et al. The ratio f_{2n}/f_{2p} in deep inelastic muon scattering. *Nuclear Physics B*, 371(1):3 – 31, 1992. [vii](#), [21](#), [22](#)
- ₁₄₁₃
- ₁₄₁₄ [7] J. Arrington, R. Ent, C. E. Keppel, J. Mammei, and I. Niculescu. Low-q scaling, duality, and the emc effect. *Phys. Rev. C*, 73:035205, Mar 2006. [viii](#), [24](#), [25](#)
- ₁₄₁₅
- ₁₄₁₆ [8] J. Ashman et al. Measurement of the ratios of deep inelastic muon-nucleus cross sections on various nuclei compared to deuterium. *Physics Letters B*, 202(4):603 – 610, 1988. [20](#)
- ₁₄₁₇
- ₁₄₁₈

- 1419 [9] J. J. Aubert et al. Measurement of the nucleon structure function f_2 in muon-
1420 iron interactions at 120,250 and 280 gev. *Physics Letters B*, 105(4):322 – 328,
1421 1981. [19](#)
- 1422 [10] J. J. Aubert et al. Measurement of the proton structure function F_2 in muon-
1423 - hydrogen interactions at 120-GeV and 280-GeV. *Phys. Lett.*, B105:315, 1981.
1424 [vii, 17, 18, 19](#)
- 1425 [11] J. J. Aubert et al. Measurement of the deuteron structure function f_{2d} and a
1426 comparison of proton and neutron structure. *Physics Letters B*, 123(1):123 –
1427 126, 1983. [19](#)
- 1428 [12] J. J. Aubert et al. The ratio of the nucleon structure functions f_{2n} for iron and
1429 deuterium. *Physics Letters B*, 123(3):275 – 278, 1983. [19](#)
- 1430 [13] T. Averett, B. Zhao, and B Wojtekowski. Bigbite heavy gas cherenkov detector
1431 at 6.6 and 8.8 gev. [ix, 51](#)
- 1432 [14] W B. Atwood, J D. Bjorken, Stanley Brodsky, and R Stroynowski. Lectures on
1433 lepton nucleon scattering and quantum chromodynamics. 01 1982. [vii, 11, 13,](#)
1434 [14](#)
- 1435 [15] G. Bari and other. A measurement of nuclear effects in deep inelastic muon
1436 scattering on deuterium, nitrogen and iron targets. *Physics Letters B*, 163(1):282
1437 – 286, 1985. [vii, viii, 20, 21, 24](#)
- 1438 [16] W. Bartel et al. Electroproduction of pions near the (1236) isobar and the form
1439 factor $g_m(q^2)$ of the (n)-vertex. *Physics Letters B*, 28(2):148 – 151, 1968. [vii,](#)
1440 [8, 9](#)
- 1441 [17] O. Benhar, V.R. Pandharipande, and I. Sick. Nuclear binding and deep inelastic
1442 scattering. *Physics Letters B*, 410(2):79 – 85, 1997. [26](#)

- 1443 [18] R P Bickerstaff and A W Thomas. The EMC effect-with emphasis on
1444 conventional nuclear corrections. *Journal of Physics G: Nuclear and Particle*
1445 *Physics*, 15(10):1523–1569, oct 1989. [26](#), [27](#)
- 1446 [19] C. Bourrely and Jacques Soffer. Deep inelastic scattering of leptons and hadrons
1447 in the QCD parton model and experimental tests. pages 1565–1581, 2001. [15](#)
- 1448 [20] Gennady M. Briskin. *Diffractive Dissociation in ep Deep Inelastic Scattering*.
1449 PhD thesis, Tel Aviv U., 1998. [11](#)
- 1450 [21] Stanley J. Brodsky, Ivan Schmidt, and Jian-Jun Yang. Nuclear antishadowing
1451 in neutrino deep inelastic scattering. *Phys. Rev.*, D70:116003, 2004. [19](#)
- 1452 [22] C. G. Callan and David J. Gross. High-energy electroproduction and the
1453 constitution of the electric current. *Phys. Rev. Lett.*, 22:156–159, Jan 1969.
1454 [12](#), [13](#)
- 1455 [23] I. C. Cloet, Wolfgang Bentz, and Anthony William Thomas. EMC and polarized
1456 EMC effects in nuclei. *Phys. Lett.*, B642:210–217, 2006. [27](#)
- 1457 [24] F.E. Close, R.G. Roberts, and G.G. Ross. The effect of confinement size on
1458 nuclear structure functions. *Physics Letters B*, 129(5):346 – 350, 1983. [27](#)
- 1459 [25] JLab MARATHON Collaboration. Measurment of the f_2^n/f_2^p , d/u ratios and
1460 a -3 emc effect in deep inelatic electron scattering off the tritium and helium
1461 mirror nuclei. Technical report, Jefferson Lab, 2010. [28](#)
- 1462 [26] A. Daniel. *Precise measurement of the nuclear dependence of the EMC effect at*
1463 *large x*. PhD thesis, University of Houston, 2007. [16](#), [19](#), [20](#), [22](#), [23](#), [26](#)
- 1464 [27] J. Denard and J. Sahar. High accuracy beam current monitor system for cebaf's
1465 hall a. Chicago, 2001. Particle Accelerator Conference. [viii](#), [40](#)
- 1466 [28] G. Dunne and A.W. Thomas. Deep inelastic scattering as a probe of nucleon
1467 and nuclear structure. *Nuclear Physics A*, 446(1):437 – 443, 1985. [26](#)

- 1468 [29] K. Nakamura et. al. Review of particle physics. *Journal of Physics G: Nuclear
1469 and Particle Physics*, 37(7A):075021, jul 2010. [vii](#), [10](#)
- 1470 [30] K.G. Fissum et al. Vertical drift chambers for the hall a high-resolution
1471 spectrometers at jefferson lab. *Nuclear Instruments and Methods in Physics
1472 Research Section A: Accelerators, Spectrometers, Detectors and Associated
1473 Equipment*, 474(2):108 – 131, 2001. [viii](#), [ix](#), [45](#), [46](#), [47](#)
- 1474 [31] David J. Flay. *Measurements of the Neutron Longitudinal Spin Asymmetry A1n
1475 and Flavor Decomposition in the Valence Quark Region*. PhD thesis, Temple
1476 University, Philadelphia, PA, Aug 2014. [vii](#), [2](#), [4](#), [39](#), [40](#)
- 1477 [32] Jerome I. Friedman. Deep inelastic scattering: Comparisons with the quark
1478 model. *Rev. Mod. Phys.*, 63:615–629, 1991. [12](#), [13](#)
- 1479 [33] D.F. Geesaman, K Saito, and A Thomas. The nuclear emc effect. *Annual Review
1480 of Nuclear and Particle Science*, 45(1):337–390, 1995. [26](#), [27](#)
- 1481 [34] M. Gell-Mann. The eightfold way: A theory of strong interaction symmetry. [14](#)
- 1482 [35] J. Gomez et al. Measurement of the a dependence of deep-inelastic electron
1483 scattering. *Phys. Rev. D*, 49:4348–4372, May 1994. [viii](#), [22](#), [23](#), [24](#), [77](#)
- 1484 [36] S.A. Goudsmit. The discovery of the electron spin. [5](#)
- 1485 [37] Daniel Greenberger and Friedel Weinert. *Compendium of Quantum Physics:
1486 Concepts, Experiments, History and Philosophy*. Springer Publishing Company,
1487 Incorporated, 2016. [5](#), [14](#)
- 1488 [38] Tyler Hague. Calibrating the hall a raster. Technical report, JLab, 2019. [viii](#),
1489 [38](#), [39](#)
- 1490 [39] K M Hanna, M E Buzaladze, V R Garsevanishvili, V A Matveev, and Z R
1491 Menteshashvili. Multiquark cluster model at large bjorken scaling variable.

1492 *Journal of Physics G: Nuclear and Particle Physics*, 19(5):721–730, may 1993.

1493 26

1494 [40] Florian Hauenstein and Reynier Cruz Torres. Tritium trigger setup. [ix](#), [55](#)

1495 [41] D. Higinbotham. The emc effect still puzzles after 30 years - cern courier.
1496 <http://cerncourier.com/cws/article/cern/53091>, April 2013. (Visited on
1497 01/04/2016). [vii](#), [2](#), [15](#), [16](#), [17](#)

1498 [42] Doug Higinbotham. Target images, December 2017. [43](#)

1499 [43] R Hofstadter. Nuclear and nucleon scattering of high-energy electrons. *Annual*
1500 *Review of Nuclear Science*, 7(1):231–316, 1957. [5](#)

1501 [44] R. L. Jaffe. Quark distributions in nuclei. *Phys. Rev. Lett.*, 50:228–231, Jan
1502 1983. [26](#)

1503 [45] Tyler Kutz Hanjie Liu Mike Nycz Tong Su Jason Bane, Tyler Hague and Evan
1504 McClellan. Marathon pass 2 analysis primer. [ix](#), [49](#), [74](#)

1505 [46] Zhihong Ye John Arrington. Marathon rate estimations. [vi](#), [57](#)

1506 [47] R. Kazimi et al. Four Beam Generation for Simultaneous Four-Hall Operation at
1507 CEBAF. In *Proc. of International Particle Accelerator Conference (IPAC'16)*,
1508 *Busan, Korea, May 8-13, 2016*, number 7 in International Particle Accelerator
1509 Conference, pages 4240–4242, Geneva, Switzerland, June 2016. JACoW.
1510 doi:10.18429/JACoW-IPAC2016-THPOY060. [31](#)

1511 [48] Henry W. Kendall. Deep inelastic scattering: Experiments on the proton and
1512 the observation of scaling. *Rev. Mod. Phys.*, 63:597–614, Jul 1991. [11](#)

1513 [49] Tyler Kutz. Tritium decay. [x](#), [73](#)

1514 [50] Christoph W. Leemann, David R. Douglas, and Geoffrey A. Krafft. The
1515 continuous electron beam accelerator facility: Cebaf at the jefferson laboratory.
1516 *Annual Review of Nuclear and Particle Science*, 51(1):413–450, 2001. [31](#), [32](#)

- 1517 [51] Nilanga Liyanage. Optics calibration of the hall a high reolution s[ectrometers
1518 using the new optimizer. [ix](#), [60](#), [61](#), [62](#)
- 1519 [52] Larry L Lucas and Michael P Unterweger. Comprehensive review and critical
1520 evaluation of the half-life of tritium. *Journal of research of the National Institute*
1521 *of Standards and Technology*, 105(4):541, 2000. [72](#)
- 1522 [53] Simona Malace, David Gaskell, Douglas W. Higinbotham, and Ian Cloet. The
1523 Challenge of the EMC Effect: existing data and future directions. *Int. J. Mod.*
1524 *Phys.*, E23:1430013, 2014. [16](#)
- 1525 [54] R. W. McAllister and R. Hofstadter. Elastic scattering of 188-mev electrons from
1526 the proton and the alpha particle. *Phys. Rev.*, 102:851–856, May 1956. [2](#)
- 1527 [55] David Meekings. Hall a tritium target, 2017. [42](#)
- 1528 [56] Jonathan Mulholland. *SANE’s Measurement of the Proton’s Virtual Photon Spin*
1529 *Asymmetry, A_1^p , at Large Bjorken x*. PhD thesis, Virginia U., 2012. [vii](#), [5](#), [14](#), [31](#)
- 1530 [57] O. Nachtmann and H.J. Pirner. *Z. Phys. C.*, 21:277. [27](#)
- 1531 [58] NMC. Detailed measurements of structure functions from nucleons and nuclei.
1532 Technical Report CERN-SPSC-85-18. SPSC-P-210, CERN, Geneva, 1985. [21](#)
- 1533 [59] P R Norton. The emc effect. *Reports on Progress in Physics*, 66(8):1253, 2003.
1534 [16](#), [21](#), [26](#)
- 1535 [60] Mike Nyzc. *EMC effect in Tritium*. PhD thesis. [viii](#), [41](#), [42](#)
- 1536 [61] G. Palacios-Serrano, F. Hannon, C. Hernandez-Garcia, M. Poelker, and
1537 H. Baumgart. Electrostatic design and conditioning of a triple point junction
1538 shield for a 200 kv dc high voltage photogun. *Review of Scientific Instruments*,
1539 89(10):104703, 2018. [31](#)

- 1540 [62] D. H. Perkins. *Introduction to high energy physics, 3rd edition*. Addison-Wesley
1541 Pub Co Inc, United States, 1986. vii, 12
- 1542 [63] B. Povh. *Particles and nuclei: an introduction to the physical concepts*. Springer,
1543 1999. vii, 2, 5, 6, 7, 8, 9, 11, 12, 13, 14, 15, 18, 19
- 1544 [64] Tom Powers, Lawrence Doolittle, Rok Ursic, and Jeffrey Wagner. Design,
1545 commissioning and operational results of wide dynamic range bpm switched
1546 electrode electronics. *AIP Conference Proceedings*, 390(1):257–265, 1997. 35
- 1547 [65] J. Seely, A. Daniel, et al. New measurements of the european muon collaboration
1548 effect in very light nuclei. *Phys. Rev. Lett.*, 103:202301, Nov 2009. viii, 2, 25
- 1549 [66] Jason Seely. *Precise Measurement of the Nuclear Dependence of Strucutre
1550 Functions in Light Nucleii*. PhD thesis, Massachusetts Institute of Technology,
1551 2006. 16, 18, 23, 25
- 1552 [67] Jason Robert Smith and Gerald A. Miller. Chiral solitons in nuclei: Saturation,
1553 EMC effect and Drell-Yan experiments. *Phys. Rev. Lett.*, 91:212301, 2003.
1554 [Erratum: Phys. Rev. Lett.98,099902(2007)]. 27
- 1555 [68] Tong Su. Positron correction analysis. x, 72
- 1556 [69] Hall A Tech. Ep method. [http://hallaweb.jlab.org/equipment/beam/
1557 energy/ep_web.html](http://hallaweb.jlab.org/equipment/beam/energy/ep_web.html). (Accessed on 06/28/2016). 40
- 1558 [70] S Wexler. Dissociation of th and t2 by β -decay. *Journal of Inorganic and Nuclear
1559 Chemistry*, 10(1-2):8–16, 1959. 72
- 1560 [71] Pengjia Zhu et al. Beam Position Reconstruction for the g2p Experiment in Hall
1561 A at Jefferson Lab. *Nucl. Instrum. Meth.*, A808:1–10, 2016. viii, 35, 36

Appendix